Structural and magnetic studies of strained thin films of $La_{2/3}Ca_{1/3}MnO_3$

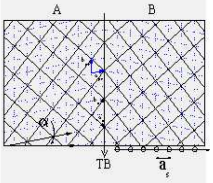

Gerardina Carbone
Stuttgart, June 2004

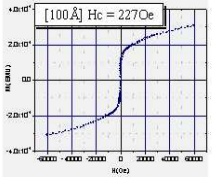

Max-Planck-Institut
für Metallforschung
in Stuttgart

Institut für Theoretische und
Angewandte Physik der
Universität Stuttgart

Structural and magnetic studies of strained thin films of $La_{2/3}Ca_{1/3}MnO_3$

Von der Fakultät Mathematik und Physik der Universität Stuttgart
zur Erlangung der Würde eines Doktors der Naturwissenschaften (Dr. rer. nat.) genehmigte Abhandlung

Vorgelegt von
Gerardina Carbone aus Salerno (Italien)

Hauptberichter: Prof. Dr. H. Dosch
Mitberichter: Prof. Dr. M. Dressel

Eingereicht am 26.05.2004
Tag der mündlichen Prüfung 05.11.2004

Institut für Theoretische und Angewandte Physik
der Universität Stuttgart

2004

Zusammenfassung

1. Motivation

Manganate mit gemischten Valenzen und Perovskit-Struktur, mit der allgemeinen chemischen Formel $A_{1-x}B_xMnO_3$, sind in den letzten 50 Jahren aufgrund ihrer interessanten und komplexen Physik, die sich beispielsweise in ihrem komplexen Phasendiagramm [1] widerspiegelt, intensiv untersucht worden. Bei Variation der Dotierungskonzentration x bilden sich diverse Phasen aus, deren Eigenschaften von antiferromagnetisch isolierend bis zu ferromagnetisch metallisch reichen und dabei ladungs- und orbitalgeordnete Regionen passieren. Die Vielfalt des physikalischen Verhaltens, die durch chemische Substitution (von Alkali- durch Seltenerd-Kationen) erzielt werden kann, macht diese Verbindungen zu einem interessanten Studienobjekt, da es möglich ist, die physikalischen Eigenschaften durch die Variation nur eines einzigen Parameters (der Konzentration x) gezielt einzustellen. Unlängst hat die Entdeckung der Phänomene des kollossalen Magnetwiderstands (CMR) und des dichten granularen Magnetwiderstands in ferromagnetischen Dünnfilmen (entsprechend einer Dotierung $x \approx 1/3$) das Interesse an diesen Materialien, die sich für Anwendungen in elektronischen Devices eignen, neu entfacht.

Beträchtliche Anstrengungen wurden unlängst hinsichtlich der Herstellung von kristallinen Filmen hoher Güte unternommen. Die Expertise, die bei der Herstellung dünner Oxidfilme in den letzten Jahren erreicht wurde, insbesondere aufgrund des groβen Interesses an der Herstellung von Hochtemperatur-

supraleitern (HTSC), erwies sich im Hinblick auf die Herstellung von Manganatfilmen hoher Güte als vorteilhaft. Techniken wie Sputtern, Molekularstrahlepitaxie (MBE) oder gepulste Laserdeposition (PLD) wurden zur Herstellung von Manganaten eingesetzt, um die Herstellung von defektfreien kristallinen Systemen zu ermöglichen, welche für die technische Anwendung geeignet sind.

Die Verwendung von Dünnfilmen hat ein neues und interessantes Forschungsfeld hervorgebracht, welches auf dem Einfluss der substratinduzierten Verspannung auf die Transporteigenschaften und die magnetischen Eigenschaften von Materialien beruht. Interessanterweise ruft die Gegenwart einer externen (epitaxieinduzierten) Verspannung neues physikalisches Verhalten hervor, welches noch nicht vollständig verstanden ist. Dieses Verhalten war lange Zeit ein zentraler Gegenstand sehr intensiver Forschung. Diverse Arbeiten beschäftigten sich mit dem Studium der Modifikation von physikalischen Eigenschaften, welche durch epitaktische Verspannung induziert wird. Allerdings ist das komplizierte Wechselspiel zwischen Struktur, Magnetismus und Transporteigenschaften in Manganaten immer noch ein offenes Forschungsfeld. Auch die vorliegende Arbeit ist in diesem Umfeld angesiedelt und soll einen Beitrag zum Verständnis dieses faszinierenden Themas leisten.

Diese Arbeit befasst sich speziell mit $La_{1-x}Ca_xMnO_3$ in der Phase bei x=1/3, welche im Folgenden als LCMO bezeichnet wird. LCMO ist unterhalb seiner Curie-Temperatur, für die in Volumensystemen $T_C \approx 280$ K gilt, ferromagnetisch metallisch und zeigt das CMR-Phänomen. Einer der Effekte, die häufig in dünnen LCMO-Filmen beobachtet werden, ist die Reduktion der Curie-Temperatur und das Auftreten von ferromagnetisch-isolierendem Verhalten, anstelle des metallischen Verhaltens im Volumen [10].

Den Hauptgegenstand dieser Doktorarbeit bildete die genaue strukturelle und magnetische Charakterisierung von verzerrten LCMO-Dünnfilmen, die epitaktisch auf $SrTiO_3$-Substraten (STO)

aufgewachsen wurden. Aufgrund der Fehlanpassung zwischen dem Kristallgitter der beiden Verbindungen wird eine mechanische Verspannung in der Filmstruktur induziert, welche zu Veränderungen der physikalischen Eigenschaften des Materials führen kann. LCMO hat im Volumen orthorhombische Struktur mit a = 5.47Å, b=5.49Å, c=7.74Å. Allerdings ist die Verwendung von pseudo-kubischen (pc) Gitterparametern sehr gebräuchlich, und für LCMO ist a_{pc}=3.87Å[1]. Die Struktur des STO-Substrates ist hingegen kubisch mit einen Gitterparameter a=3.905Å, und für epitaktische LCMO-Filme auf STO ist der Vektor a_{pc} von LCMO entlang der kristallographischen $< 100 >$ STO-Achse orientiert. In diesem Fall ist die Fehlanpassung zwischen den beiden Strukturen $\delta \approx 1\%$, und die Filme sind einer tensilen Verspannung unterworfen.

Das epitaktische Wachstum eines Films auf einem Substrat kann eine Übereinstimmung der Gitterparameter des Films in der Ebene mit denen des Substrates an der Grenzfläche zwischen den beiden Verbindungen (in diesem Fall LCMO und STO) induzieren. Wenn dies für die volumenrelaxierten Strukturen noch nicht der Fall ist (d.h. in Gegenwart einer Fehlanpassung $\delta \neq 0$), befinden wir uns im Bereich des pseudomorphen Wachstums, und die Verspannung, die durch das Substrat induziert wird, führt zu einer Modifizierung des Films. Das pseudomorphe Wachstum ist dann das Resultat einer Energiebalance zwischen der Tendenz des Kristallgitters, relaxiert zu wachsen, entsprechend der internen Energiebilanz, und dem externen Druck des Substrats, welches als Templat struktur wirkt. Das epitaktische Wachstum eines Films bei Vorliegen einer Fehlanpassung kann folglich zu strukturellen Verzerrungen führen, die - als Mechanismus zur Relaxation der epitakischen Verspannung - aus der mechanischen Reaktion des Kristallgitters auf die Gegenwart des Substrates resultieren. Diese Reaktion kann von Fall zu Fall variieren, in Abhängigkeit vom Grad der Fehlanpassung

[1]Der pseudo-kubische und der orthorhombische Gitterparameter sind gegeneinander um 45^o verdreht.

sowie von der Natur der atomaren Bindungen und demzufolge von der Steifigkeit des Gitters. Die spannungsinduzierten Gitterverzerrungen können lokalisiert sein oder über mehrere Einheitszellen hinweg moduliert. Dabei können sie direkt diejenigen physikalischen Eigenschaften beeinflussen, welche mit der Gitterstruktur verknüpft sind. Daher stellt eine genaue Studie der Kristallstruktur eines verspannten Materials einen wichtigen Schritt zum Verständnis der Veränderung von physikalischen Eigenschaften in der Gegenwart von Verspannungen dar.

2. Experiment

Das Hauptziel dieser Arbeit ist die genaue Analyse der spannungsinduzierten Modifikationen der Struktur der LCMO epitaktischen Filme und ihr Effekt auf die magnetischen und Transporteigenschaften des Materials. Die untersuchten Filme, die 50Å bis 600Å dick sind, wurden mit gepulster Laserablation von Dr. J. Klein, von der Universität Köln, hergestellt.

Die Filme sind ferromagnetisch und zeigen den CMR-Effekt. Ihre kritische Temperatur, im Bereich von $\approx 130K$, ist deutlich niedriger als der Volumenwert ($T_C \approx 280K$) und zeigt keine Dickenabhängigkeit. Das bedeutet, dass es selbst für die grössten gemessenen Dicken keine Anzeichen für eine Relaxation zu dem Volumenwert gibt. Die Struktur der Filme wurde mit Röntgenbeugung am Synchrotron untersucht, um die Verbindung zwischen der Struktur der Filme und ihren magnetischen Eigenschaften herauszufinden.

Röntenbeugung ist eine nicht zerstörende Technik, die eine genaue strukturelle Untersuchung der Filme erlaubt. Sie wurde in dieser Arbeit besonders benutzt um das epitaktische Verhalten zwischen Film und Substrat zu untersuchen. Insbesondere sollen eventuell vorhandene spannungsinduzierte Verzerrungen, Modifikationen der Kristallsymmetrie und allgemeiner, die Mechanismen zum Abbau der Spannung innerhalb des Films

untersucht werden. Die Signale, die von den spannungsinduzierten Verzerrungen kommen, sind sehr schwach im Vergleich mit Braggstreuung (drei bis vier Grössenordnungen kleiner) und können daher mit konventionellen Quellen nicht detektiert werden. Daher wurde in dieser Arbeit Synchrotronstrahlung verwendet. Die Messungen wurden hauptsächlich an der Beamline BM28 (XMaS, UK CRG) der ESRF (European Synchrotron Radiation Facility) in Grenoble (Frankreich) und an der MPI Oberflächenstreuungsbeamline an ANKA in Karlsruhe durchgeführt.

Die Untersuchung mit Diffraktion unter streifendem Eifall (GID) und "Crystal Truncation Rods" (CTR) haben ein vollständiges Bild der strukturellen Eigenschaften dieser Filme ergeben. Insbesondere hat die Verwendung von GID zur Messung der "*in-plane*" Struktur der Filme die Beobachtung einer Mikrostruktur erlaubt. Diese Mikrostruktur besteht aus Zwillingsdomänen (" twin domains", TD) ähnlicher Grösse, die periodisch in der Wachstumsebene angeordnet sind. Die Zwillings achse ist die $< 110 >_{ortho}$ Achse.

Wir vermuten dass diese Modulation der Zwillingsdomänen die strukturelle Antwort des Films auf die vom Substrat induzierte Spannung ist. Die Bildung von Zwillingsdomänen findet sehr oft in Perovskitkristallen statt, da dieser Prozess wenig Energie kostet. Im Spezialfall epitaktischen Wachstums erzeugt die Modulation eine mittlere Struktur, welche dabei hilft, den Unterschied der Gitterparameter zwischen Film und Substrat zu reduzieren. Konsequenter Weise hat dies einen starken Einfluss auf das Energiegleichgewicht des Wachstumsprozesses. Dieser spannungsreduzierende Prozess ist energetisch bevorzugt gegenüber Verzerrungen der Einheitszelle oder Verschiebungen der Atomabstände.

Die Signatur dieser periodischen Mikrostruktur in den GID Profilen, ist die Anwesenheit breiter Überstrukturreflexe (superlattice peaks (SL)) um die "*in-plane*" Braggreflexe vom Typ $[H\,K\,0]$. Diese SL-Reflexe besitzen sehr geringe Intensität ver-

glichen mit den Bragg Reflexen ($\approx$ 3 Grössenordnungen weniger). Für Braggreflexe vom $[H\,0\,0]$ und $[0\,K\,0]$ Typ findet man zwei SL in einer Entfernung von $\pm\vec{q}$ vom zentralen Maximum, in Richtung senkrecht zum Streuvektor. Für Reflexe vom $[H\,K\,0]$ Typ findet man stattdessen vier SL, mit Wellenvektoren $\vec{q}$ parallel zu den $< 100 >_c$ und $< 010 >_c$ kristallographischen Achsen. Diese SL zeigen die Anwesenheit einer eindimensionalen strukturellen Modulation an, d.h. eine zusätzliche Periodizität in der Struktur des Films mit Komponenten in der Wachstumsebene $a - b$ und der charakteristischen Länge $\Lambda_0 = 2\pi/q$. In der Umgebung reiner "*out-of-plane*" Reflexe dünner Filme (100 Å) wurden keine SL gefunden. Bei dickeren Filmen wurde stattdessen ein breites Maximum zusammen mit einer scharfen Komponente vom $[0\,0\,L]$ Typ beobachtet. Solch eine breite Komponente könnte auch einer schwachen Korrelation der "*out-of-plane*" Periodizität zugeschrieben werden.

3. Modell

In dem von uns vorgestellten Modell ist die Grösse der Zwillingsdomänen statistisch um einen durchschnittlichen Wert L_0 mit einer Standardabweichung ΔL_0 verteilt. L_0 ist die Periodizität der Zwillingsdomänenmodulation, allerdings steht sie mit der Modulationswellenlänge Λ_0 in einem nicht trivialen Zusammenhang. Unser Modell besitzt nur zwei Parameter. Der Erste ist der Kippwinkel (α) des pseudokubischen Gitters zwischen den beiden Zwillingsdomänen. In unserem Modell steht α mit der Orthorhombizität a_o/b_o des Films im Zusammenhang $\alpha = 90^o - 2arctan(a_o/b_o)$. Für einen Volumenkristall von LCMO ist der Zusammenhang $\alpha_{bulk} = 0.31^o$. In dünnen Filmen kann dieser Wert durch die Anwesenheit von epitaktischer Spannung stark verändert werden. Aus diesem Grund wird α in unserem Modell als variabel angesehen. Der zweite Parameter ist die maximale Anzahl von Einheitszellen, die in einer Domäne erlaubt

sind. Dies ist ein phänomenologischer Parameter, der von der inneren mechanischen Energie des Systems abhängt und ebenfalls als variabel angesehen wird. Eine detaillierte Beschreibung des Modells befindet sich in der Doktorarbeit von U.Gebhardt, der das Modell und das Programm zur Simulation der Streuprofile entwickelt hat. Dieses vereinfachte Modell, welches den Strukturfaktor der Einheitszelle nicht berücksichtigt, reproduziert überraschend gut die experimentellen Streuprofile. Auf der Basis dieser Resultate glauben wir, dass unser Modell auf alle Systeme angewendet werden kann, die die Entstehung von Zwillingsdomänen erlauben, und als einer der möglichen Spannungsrelaxationsmechanismen perowskitischer Filme angenommen werden kann.

4. Ergebnisse

4.1 *In-plane*

Als Ergebnis der Anwendung dieses Modells haben wir für den 100 Å Film eine *in-plane* Verteilung der Zwillingsdomänen gefunden, mit einer durchschnittlichen Domänengrösse von $L_0 = 32$ Einheitszellen (EZ) und einer Verteilungsbreite von $\Delta L_0 = 16$ EZ. Der Kippwinkel α wurde aus den Simulationen zu $\alpha = 0.06^o$ bestimmt, was einer Orthorhombizität von $a_o/b_o = 0.9991 \approx 1$ entspricht, mit einem *in-plane* Gitterparameter, der etwas grösser ist als im Volumen. Dies kann mit Wettstreit zwischen epitaktischem Wachstum und der Tendenz Zwillingsdomänen zu bilden, erklärt werden. Das Energiegleichgewicht tendiert dazu, die Entstehung von Zwillingsdomänen zu favorisieren, während das epitaktische Wachstum versucht den LCMO Film mit demselben "*in-plane*" Gitterparameter wie das STO Substrat zu erzeugen. Die resultierende Atomkonfiguration besteht aus einer periodischen Anordung von LCMO Zwillingsdomänen mit einem

vergrösserten Gitterparameter.

Bei grösseren Dicken, wie bei dem 400 Å Film, konnte ein befriedigendes Modell der Streuprofile erstellt werden indem die Struktur als bestehend aus drei verschiedenen *in-plane* Zwillingsdomänenverteilungen angesehen wurde. Diese Verteilungen werden durch folgende Durchschnittswerte und Abweichungen charakterisiert: $L_{01} = 32$EZ und $\Delta L_{01} = 14$EZ, $L_{02} = 64$EZ und $\Delta L_{02} = 24$EZ, $L_{03} = 79$EZ und $\Delta L_{03} = 49$EZ . Dies kann durch ein Modell von steigender Unordnung in der Domänenverteilung in der Wachstumsrichtung erklärt werden. Wenn die Dicke des Films sich vergrössert, wird die Verteilung der Domänen durch den Prozess des *Spannungsabbaus* immer ungeordneter. Dennoch verschwindet die durch das Substrat ausgeübte Spannung nicht völlig und die strukturellen Eigenschaften des Films werden nicht identisch mit denen eines relaxierten Volumensystems. Der Kippwinkel für die drei Verteilungen ist derselbe wie in dem dünnen Film, d.h. $\alpha = 0.06^o$, obwohl eine Veränderung (und insbesondere eine Erhöhung in Richtung des Volumenwertes) durch die *Relaxation* der Struktur erwartet würde. Aus Simulationen ist ersichtlich, dass eine Variation des Kippwinkels α allein nicht ausreicht um die Daten zu reproduzieren. Weiterhin sollte α einen Wert von 0.07 nicht überschreiten, um eine gute Übereinstimmung zwischen den simulierten und den gemessenen Streuprofilen zu erzielen. Da die Einführung einer solchen kleinen Veränderung keine weitere Verbesserung der Simulation mit sich bringt und da das Modell zu diesem Zeitpunkt noch qualitativ ist, wurde in unseren Simulationen α konstant bei $\alpha = 0.06$ gehalten. Auf der Basis der vorangegangenen Diskussion können wir sagen, dass der Wert von α in der Domänenverteilung entlang der c-Richtung um 18 % bis 19 % variiert.

4.2 *Out-of-plane*

Die Anwesenheit des breiten Intensitätsbeitrags an Positionen vom $[0\,0\,L]$ Typ kann mit demselben Modell durch eine "*out-of-plane*" Zwillingsdomänenmodulation erklärt werden. Einer der möglichen Ursprünge dieser Modulation könnte eine *monokline* Verzerrung der LCMO Einheitszelle sein, was die identische Periodizität in sowohl "*in-plane*" als auch "*out-of-plane*" Richtungen erklären könnte. Die zweite Möglichkeit ist das Vorhandensein kristallographischer Domänen mit c-Gitterachse in der Wachstumsebene. In diesem Fall könnten Zwillingsdomänen mit Zwillingsachse $< 110 >_o$ senkrecht zur Oberfläche dieselbe Periodizität in diese Richtung erzeugen. Die Verzwillingung entspricht dann einer leichten periodischen Verkippung des Films auf der Oberfläche des Substrats. Die geringe Intensität und die grosse Breite dieser Komponente wäre ein Merkmal einer geringen Anzahl solcher Domänen und einer schwachen Korrelation dieser Modulation. Die Überprüfung dieser Hypothesen benötigt eine genaue kristallographische Analyse, was über den Rahmen dieser Arbeit hinaus gehen würde.

4.3 Crystal Truncation Rod

Die CTR Messungen bestätigen die Anwesenheit einer Art von *Spannungsabbau* parallel zu der Wachstumsrichtung in dicken Filmen. In der Intensität der Laueoszillationen wurde eine starke Asymmetrie beobachtet. Dies kommt von einer Variation des Gitterparameter in c-Richtung sowohl an der Oberfläche als auch an der Film-Substrat Grenzfläche. Der c-Gitterabstand erhöht sich von der Grenzfläche zur Mitte des Films und verringert sich wieder an der Oberfläche. Die Veränderung an beiden Grenzflächen folgt einem exponentiellen Gesetz, mit einer Amplitude von $\Delta c \approx 0.07$Åund einer Zerfallslänge von ≈ 6 Einheitszellen. Die Veränderung des c-Gitterparameters an den beiden Grenzflächen kann durch die vom Substrat induzierte *Spannungsrelaxation* erklärt werden. Diese Relaxation kann

auch zu einer Veränderung der Kalzium Stöchiometrie an den Grenzflächen führen, wie durch EELS Messungen an Proben gezeigt wurde, die unter denselben Bedingungen gewachsen wurden [107]. Es ist bekannt, dass eine Veränderung der Kalziumkonzentration einen starken Einfluss auf den Gitterparameter von LCMO hat [106] und dies könnte auch zur Erniedrigung des c-Gitterparameters zur Oberfläche des Films beitragen.

Es ist wichtig hervorzuheben, dass trotz der beobachteten Veränderung des c-Gitterparameters in Richtung des Volumenwertes und dem Modell von steigender Unordnung in der Verteilung der Zwillingsdomänen in dicken Filmen, diese Filme keinen Anhaltspunkt für eine starke Relaxation *in Richtung der Volumenwerte* liefern. Dies gilt sowohl für strukturelle wie magnetische Eigenschaften. Alle untersuchten Dicken zeigen epitaktisches Wachstum und, wie durch magnetische Messungen gezeigt wird, dieselbe kritische Temperatur T_C. Dies zeigt, dass die Filme bis zum dicksten untersuchten Film (600 Å) als verspannt angesehen werden können.

4.4 Magnetismus

Die magnetischen Messungen wurden sowohl mit SQUIDs (superconducting quantum interference device) als auch mit polarisierter Neutronenreflektometrie (PNR) durchgeführt. Diese beiden Techniken wurden auf eine komplementäre Weise genutzt. Die SQUID Messungen, welche die durchschnittlichen magnetischen Eigenschaften der Probe messen, wurden benutzt um die Curietemperatur, die Sättigungsmagnetisierung und das Koerzitivfeld der Probe zu bestimmen, während die PNR Messungen benutzt wurden, um das Magnetisierungsprofil der Probe zu messen und den Mechanismus zu untersuchen durch den die Spannungen die *Magnetisierungverteilung* des Films beeinflussen.

Die SQUID Messungen zeigen, dass alle Filme ferromag-

netisch sind mit einer starken Erniedrigung der kritischen Temperatur. Diese liegt im Bereich zwischen 80 und 130K. Ein Einfluss der Filmdicke kann nicht beobachtet werden, was zeigt, dass Spannungen bis zu den grössten untersuchten Dicken bestehen bleiben. Interessante Ergebnisse liefert die Analyse der Hysteresekurven. Die Magnetisierung der Proben sättigt nicht komplett bis zu der grössten angelegten magnetischen Feldstärke $H = 6$Tesla. Dieser Effekt kann entweder durch eine Verkippung (canting) der magnetischen Momente erklärt werden, oder durch die Anwesenheit nicht gleich ausgerichteter magnetischer Domänen. Letztere Hypothese, die in kürzlich erschienenen Publikationen diskutiert wurde [72, 108], ist in guter Übereinstimmung mit den Ergebnissen unserer strukturellen Untersuchungen. Die magneitschen Domänen könnten mit der Anwesenheit der kristallographischen Domänen in Zusammenhang gebracht werden. Dies könnte mit Magnetischer Kraftmikroskopie (MFM) bewiesen werden. Die Grösse der magnetischen Domänen ist vermutlich vergleichbar mit der Grösse der kristallographischen Domänen, die mit unserem Modell gefunden wurden.

Weiterhin sinkt der Wert für die Sättigungsmagnetisierung der Filme, berechnet für das höchste gemessene Feld ($H = 6$Tesla), stark mit steigender Probendicke. Der Abfall folgt einem Exponentialgesetz mit einer Zerfallslänge von ≈ 6 Einheitszellen, während die durchschnittliche Magnetisierung innerhalb von 600 Åauf 20% des Höchstwertes sinkt. Dieser Abfall ist in sehr guter Übereinstimmung mit den CTR Ergebnissen, was auf eine starke Korrelation zwischen struktureller *Relaxation* und Veränderung der magnetischen Eigenschaften schliessen lässt.

Die Ergebnisse der SQUID Messungen wurden von den PNR Experimenten bestätigt, die an der EVA Beamline des ILL in Grenoble (Frankreich) durchgeführt wurden. Für eine der dicken Proben (400 Å) ergeben die PNR Messungen einen Beweis für einen starken Gradienten in dem magnetischen Profil des Films,

wie er aus den SQUID Ergebnissen erwartet wird. Das durchschnittliche magnetische Moment besitzt seinen höchsten Wert von $3\mu_B$ an der Grenzfläche und sinkt exponentiell in Wachstumsrichtung bis es einen niedrigsten Wert von $0.7\mu_B$ an der Filmoberfläche erreicht, in guter Übereinstimmung mit den SQUID Messungen.

Diese besonderen magnetischen Eigenschaften, zusammen mit dem Modell der Veränderung der Zwillingsdomänenverteilung und der c-Gitterparameters, kann der zunehmenden Unordnung in den Domänen zugeschrieben werden, was ebenfalls eine Unordung in den magnetischen Domänen widerspiegelt. In diesem Sinn konvergieren alle Messungen in einem Modell des epitaktischen Wachstums, welches durch Zwillingsdomänenperiodizität erreicht wird, mit einer schärferen Domänenverteilung an der Grenzfläche und einer breiteren Verteilung an der Oberfläche. Diese Veränderung ist ein Zeichen einer Zunahme von Unordnung in der Domänenverteilung, welche auch in dem magnetischen Profil auftaucht.

Contents

Introduction

Mixed valence manganites with perovskite structure, with general formula $A_{1-x}B_xMnO_3$ have been widely studied in the past 50 years because of their interesting and complex physics as demonstrated by their rich phase diagram[1]. Changing the dopant concentration x allows the formation of diverse phases, which change from insulating antiferromagnetic, to ferromagnetic metallic, passing through charge and orbital ordered regions. The variety of physical behaviour achievable via this chemical substitution (rare earth for alkali cations) makes these compounds an interesting subject of study, due to the possibility of tuning physical properties by the controlled variation of only one parameter, i.e. x. Recently, the discovery of phenomena of Colossal Magneto Resistance (CMR) and dense granular magneto-resistance in ferromagnetic thin films[2, 3] (corresponding to the doping $x \approx 1/3$) has renewed the interest towards them, as materials suitable for applications in electronic devices.

It is well established[4] that the theory of *double exchange*[5] alone does not explains the magnetotransport properties of manganites, and the introduction of lattice effects (as *Jahn-Teller* effect[6]) is crucial. However, a complete theory which explains the phenomenon of CMR, is still lacking. As a result the study of Mn-compounds is interesting for both general understanding and applications. A general introduction on these compounds can be found in the first chapter of this thesis.

One of the fundamental properties of these materials is the

strong interplay between structure, magnetism and transport[4, 7]. For this reason, great attention has been devoted to the study of high purity single crystals, to allow a high control on structure and doping, towards a clearer study of their effects on the physical properties. Moreover, due to the importance of thin films for the electronic industry, a good knowledge and understanding of their properties is necessary to make them suitable for applications. In this perspective, considerable efforts have also been addressed to the fabrication of high quality crystalline films.

In the last few years, methods of fabrication of thin films of complex oxides of very high quality have been strongly developed and refined especially due to the large interest in fabrication of High Temperature Superconductors (HTSC)[8, 9]. The use of techniques such as sputtering, Molecular Beam Epitaxy (MBE) or Pulsed Laser Ablation (PLA), applied to the fabrication of manganites, has been an advantage for the fabrication of high quality manganite films, providing crystalline systems devoid of defects and more suitable for applications.

The use of thin films has introduced a new and interesting field of study, via the role of the strain induced by the substrate onto the transport and magnetic properties of the materials, as discussed in more detail in chapter 2. Most interestingly, the presence of external strain (due to the epitaxy) introduces new physical behaviours, not yet completely understood, which have been for long time at the center of a very intensive research. Several works have been addressed to the study of the modification of physical properties introduced by epitaxial strain (cf [10, 11, 12, 13, 68], and [15] and references therein). However, the complicated interplay between structure, magnetism and transport properties in manganites is still an open field, and the present work enters this framework as a contribution to the understanding of this fascinating topic.

This work focuses on $La_{1-x}Ca_xMnO_3$ in the $x = 1/3$ phase, hereafter referred to as LCMO. LCMO is ferromagnetic metallic

below its Curie temperature which, for bulk systems, is $T_C \approx 280K$, and presents the phenomenon of CMR. One of the effects widely observed in thin LCMO films is the reduction of the Curie temperature and the appearance of a ferromagnetic *insulating* behaviour, instead of the metallic of the bulk[12, 13]. On the other hand, in thin films of $La_{1-x}Sr_xMnO_3$ in its ferromagnetic insulating phase ($x \approx 1/8$) a *metallic* behaviour has been detected in the ferromagnetic phase, together with an increase of the T_C (250K instead of the 180K of the relative bulk system)[14]. As can be seen from these two simple examples, the effect of the strain on these compounds is not unique and seems to depend on the individual cases.

The main scope of this thesis has been the accurate structural study of manganite strained thin films, in order to understand the mechanism of relaxation of strain and its influence on other physical properties. For this purpose, X-Ray Diffraction (XRD) measurements have been carried out on a series of LCMO samples with thickness varying between 50Å and 600Å.

XRD technique is a non-destructive technique which allows an accurate structural study of the films. It has been adopted in this work with particular attention to the evaluation of the epitaxial relationships between film and substrate, to detect eventual strain-induced distortions, modification of the crystal symmetry and, more generally, the study of the mechanisms adopted by the film to relieve the strain. A general introduction to the XRD and the formalism used in this work can be found in chapter 3. The use of Grazing Incidence Diffraction (GID) and Crystal Truncation Rods (CTR) measurements, have provided a complete picture of the structural properties of these films, allowing the observation of a particular microstructure, induced by the epitaxial strain, which has led to the formulation of a model of relaxation of epitaxial strain of quite general applicability. Experimental data, together with the model proposed to describe them, are presented in chapter 5 and 6.

XRD measurements have been performed with the use of

synchrotron radiation. The reason for this is that the signals arising from strain-induced distortions are expected to be very weak compared with Bragg scattering (few orders of magnitude smaller), impossible to detect with conventional sources. The measurements have been carried out mainly at the beamline BM28 (XMaS, UK CRG) at the European Synchrotron Radiation Facility (ESRF) in Grenoble -France, and also at the MPI Surface Scattering Beamline at ANKA in Karlsruhe - Germany.

To complete the analysis of the physical properties of these films, magnetic measurements have also been performed, both with Superconducting QUantum Interference Device (SQUID) and Polarised Neutron Reflectivity (PNR) techniques. These two techniques have been used in a complementary way. SQUID measurements, sensitive to average magnetic properties of the samples, have been used to measure the Curie temperature, the saturation magnetisation and the coercive fields of the samples, while PNR measurements have been used for the investigation of the magnetisation profile of the sample, to analyse the way in which the strain influences the magnetisation *distribution* in the film.

Interesting results have been obtained from the analysis of magnetic measurements. The main effect of the strain seems to be a reduction of the average magnetic moment $< m >$. This effect increases with increasing thickness, and determines, in thicker films, a gradient in the magnetic profile of the sample: $< m >$ decreases from the interface crystal-substrate to the surface of the film. Details on the measurements and discussion can be found in chapter 3.4. Such gradient in the magnetisation profile seems to have a correspondence in the structural profile, as observed by CTR measurements, discussed in chapter 6.

Chapter 1

Overview on Mn-compounds: bulk properties

In this chapter, we will present a short overview on the structural and electronic properties of the Mn compounds corresponding to the general formula $RE_{1-x}AE_xMnO_3$ (RE = rare earth, AE = alkali earth). In particular, the case of RE = La and AE = Ca, with Ca concentration $x \approx 1/3$ will be highlighted, which is the compound studied in this work (for a review on manganites compounds, see references [15, 16]). An important aspect of these manganite compounds is the strong interplay between structure, magnetism and transport properties. We will see how the structural phase diagram changes with the magnetic properties, showing a very rich variety of physical behaviour on varying the AE cation concentration[1].

Before outlining the problems connected with the topic of this work, i.e. structural and magnetic properties of manganite thin films, we will start with a general picture of the structure of the bulk complex oxides, i.e. the perovskite structure.

For these compounds it is not really possible to separate the crystal structure from the magnetic and transport properties, which change with the dopant concentration x. A complete pic-

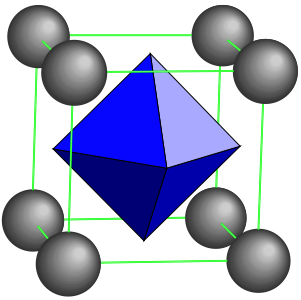

Figure 1.1: Schematic $SrTiO_3$ cubic unit cell with lattice parameter $a_0 = 3.905$Å. The TiO_6 octahedron is highlighted in blue and the Sr-atoms are at the corners of the cube.

ture of manganites should include crystal structure, magnetic properties, together with transport properties. However, for the sake of the simplicity, we will divide this chapter in three sections. The first describes the general features of the crystal structure of the complex oxides. The second describes the magnetic and transport properties of these compounds with respect to the doping concentration and the third focuses on the phase diagram of the $La_{1-x}Ca_xMnO_3$ solid solution.

1.1 Crystal structure

In spite of the variety of possible phases, the crystal structure of the manganese compounds still remains a common characteristic, only changing in a fine way with dopant concentration. The basic structure of the complex oxides is the perovskite structure, generally indicated by the formula ABO_3. The prototype compound is $SrTiO_3$ with cubic symmetry and lattice parameter $a_o = 3.905$Å, shown in figure 1.1.

A cubic perovskite can generally be thought as a closed packed arrangement of oxygen O^{2-} and either A^{2+} or A^{3+} ions in a fcc unit cell, and with either the B^{4+} or the B^{3+} ions occupying interstitial positions. The A-site cation has a twelve-fold oxygen coordination while the B-site cation has a six-fold oxygen coordination, which forms the BO_6 octahedron that plays a dominant role in the physics of manganite compounds (figure 1.1). The described atom arrangement requires that the ionic radii of O^{2-} and A^{2+} (and A^{3+}) are similar, satisfying the equality $r_A \approx r_O = 1.40$Å. From simple geometrical considerations, the atomic radii of the ion r_B also can be calculated: $r_B \approx (\sqrt{2} - 1)r_O = 0.58$Å.

The tolerance factor, defined as

$$t' = \frac{r_A + r_O}{\sqrt{2}(r_O + r_B)}$$

introduced by Goldschmidt in 1958, determines the stability limit for the oxide structure. This term defines a numerical relation between the dimension of the A-site and B-site cations. The value of t' is unity for ideally sized ions, giving rise to systems with ideal cubic symmetry. However, for most of the perovskite structures it is $0.89 < t' < 1.02$[15], leading to a wide range of structures and space groups.

1.1.1 Mn-perovskites

In Mn-perovskites with general formula $RE_{1-x}AE_xMnO_3$, the A-site rare earth (RE) trivalent cation can be substituted with a divalent alkali earth (AE) cation. The main effects of AE substitution (defined quantitatively by the concentration parameter x) are the variation of the number of electrons in the $3d$-band, the change of the interatomic distances and the Mn-O-Mn bond angles.

The size mismatch of the cations RE and AE generates deviations from the ideal perovskite crystal structure. The shift

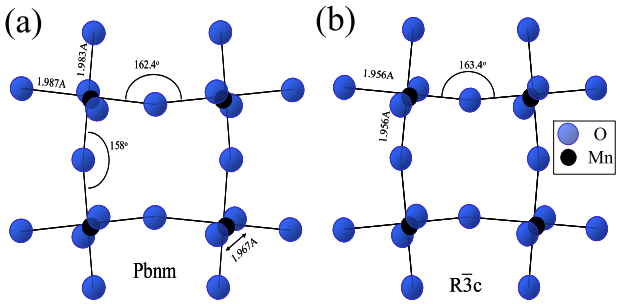

Figure 1.2: Scheme of (a) orthorhombic and (b) rhombohedral unit cell of the compound $La_{1-x}Sr_xMnO_3$ showing only the Mn-O plane. In a cubic unit cell the untilted octaedra generate a O-Mn-O bonding angle of 180^o

of the atoms from their ideal position can give rise to local distortions and tilts of oxygen octahedra. In Mn-compounds, the MnO_6 octahedra determine the crystal lattice symmetry. The doping generally leads to a change toward larger unit cells of lower symmetry.

The main types of structure generated by distortion of the ideal cubic perovskite structure are the rhombohedral ($R\bar{3}m$) and the orthorhombic (Pbnm) structure. In figure 1.2 is represented schematically the change in Mn-O bonding length and O-Mn-O bonding angle in $R\bar{3}m$ and Pbnm unit cell with respect to the cubic symmetry. A variety of small modifications of these have also been detected (cf reference [15] and references therein].

A rhombohedral lattice is generated by cooperative tilts of octahedra around the cubic $< 111 >$ crystallographic direction, due to the introduction of a small cation mismatch. A larger cation mismatch, on the other hand, leads to a buckling of the octahedra, which corresponds to a cooperative rotation around the cubic $< 110 >$ direction. The octahedral tilts influence the

Mn-O-Mn bond angle ϕ, the most sensitive parameter to the size of the A-site cation. When ϕ is reduced to values $\phi < 180$, it generates the orthorhombic O-type structure with $a < c/\sqrt{2} < b$, shown in figure 1.2(a). Finally, a strong deformation of oxygen octahedra around the Mn^{3+} ion, with Mn-O-Mn bond extended in one direction in the *a-b* plane, generates the orthorhombic O'-type structure ($c/\sqrt{2} < a < b$). This kind of deformation frequently occurs in the manganites and is called *Jahn-Teller* (J-T) type distortion and will be discussed in section 1.2.2.

A large variety of tetragonal, hexagonal and monoclinic unit cells also characterises the crystal structures of Mn-compounds, and more generally perovskite structures[17, 18, 19]. The unit cells are usually closely related. The doubled cubic cell $a \approx 2a_o$ contains 8 formula units (Z = 8). The rhombohedral cell with $a \approx 2a_o$ and $\alpha \approx 90.4^o$ is a deformed version (Z = 8) flattened along the $< 111 >$ direction. A smaller rhombohedral cell with $a \approx \sqrt{2}a_o$ and $\alpha \approx 61^o$ has Z = 2. The orthorhombic cell with $a \approx b \approx \sqrt{2}a_o$ and $c \approx 2a_o$ has Z = 4, as well as a closely related tetragonal cell with $a = b \approx \sqrt{2}a_o$ and $c \approx 2a_o$. Because all the structures are closely related, it is very common to refer to them using *one* formula unit and the so called *pseudo-cubic* lattice parameter a_{pc}. In figure 1.3 the relation between pseudocubic and orthorhombic lattice is shown as an example.

1.1.2 Domains and twinning

A very important aspect of the lowering of symmetry from the ideal cubic structure is the formation of *domains*. A $< hkl >$ domain is defined as a crystal with the crystallographic axis $< hkl >$ oriented along an arbitrarily defined direction in space, say z. Domains with different orientation, i. e. with different crystallographic axis directed in the same direction z, can coexist in a crystal. This can introduce new complications in the study of physical properties, especially in the detection of anisotropic properties, such as orbital order, magnetic order,

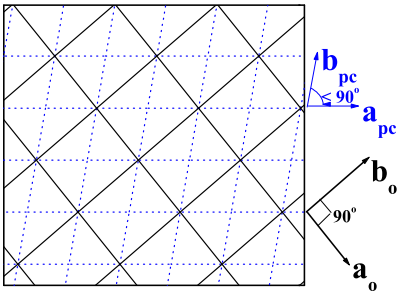

Figure 1.3: Scheme of a pseudocubic lattice for an orthorhombic system

stripe phases or one-dimensional distortions[20].

The presence of crystallographic domains should not be confused with polycrystallinity. In polycrystalline samples the crystallites are randomly distributed in space, without a preferred orientation. Domains, on the other hand, have a specific orientation and, in a good quality crystal, the ones oriented in the same direction are characterised by very similar values of the lattice spacing. For example in the $La_{2/3}Ca_{1/3}MnO_3$, where $a = 5.47$Å, $b = 5.49$Å, and $c = 7.74$Å, the directions $< 110 >$ and $< 001 >$ have a very close plane spacing $d \approx 7.75$Å. Finally, *twin domains* are coherent domains which have a certain lattice plane in common. A more detailed description can be found in chapter 5 at page 101.

1.2 Transport and magnetic properties

Manganite-perovskites present a rich variety of magnetic states strongly coupled with transport properties and structure. For these materials the role of structure and in particular of the distortion of the MnO_6 octahedra is of great importance for the magnetic and conduction properties. This is because the MnO_6 octahedra are central to the Double Exchange mechanism, discussed later (section 1.2.4, page 37).

The coupling of structure and transport properties of manganites is not completely understood. Few works have been addressed to the exploration of this coupling[21, 22], indicating that more has to be done to understand it. For the Sr-doped manganite compound $La_{1-x}Sr_xMnO_3$, for example, the rhombohedral phase is metallic while the orthorhombic one is insulating. The compound $La_{1-x}Ca_xMnO_3$, on the other hand, shows an orthorhombic type of symmetry in the whole doping range, even though it changes from antiferromagnetic (AF) insulating to ferromagnetic (FM) metallic for increasing x. This suggests that it is not the long range crystal symmetry that has a great importance on the transport, but instead, some kind of local order might be involved in the transport properties.

1.2.1 Electronic configuration

In this section, the role of the Mn^{3+} and Mn^{4+} ions in the structural magnetic and transport properties will be discussed. As already pointed out, the main effect of the doping in manganites is the change of the valence of the A-site cation, i.e. the concentration of Mn^{4+} ions, and consequently the number of electrons in the $3d$ band. The nominal electronic configurations of Mn^{3+} and Mn^{4+} are respectively $3d^4$ and $3d^3$. These levels are of great importance for the structural and electronic properties of manganites. In absence of a crystal field the Mn d levels are five-fold degenerate. In a crystalline structure, due to the interaction with neighboring ions, the degeneracy is partially

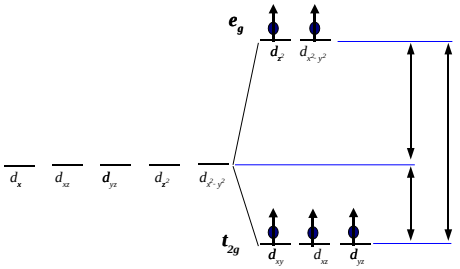

Figure 1.4: Mn 3d levels in a crystal field

lifted generating a triplet in the t_{2g} level, and a doublet in the e_g level (see figure 1.4). On the basis of energetic considerations it turns out that the configuration with 3 electrons in the t_{2g} level aligned in the same direction is the most favorable, the probability of any other configuration being too small to have any physical relevance[37]. The electrons aligned in the t_{2g} level form a "core spin" which does not contribute to the conductivity. The remaining electrons in the e_g levels are aligned to the core spin via strong Hund coupling and are free to move through the crystal.

The presence of the Mn^{3+} and Mn^{4+} ions is crucial for the physics of manganites, the properties being summarised in terms of the Mn^{3+}/Mn^{4+} ratio. Is is worth mentioning that the concentration of Mn^{4+} ions can also be tuned changing oxygen deficiency or La stoichiometry, which leads to similar properties of FM phase and conductivity[23].

1.2.2 Jahn-Teller distortions

The Mn^{3+} ion and its electronic instability in a crystal field, is responsible for the structural distortion of the MnO_6 octahedra. This effect, known as Jahn-Teller effect[6], is of great importance

to the physics of these compounds.

The Jahn-Teller (J-T) type distortion consists of the variation of the Mn-O-Mn bond length due to the electronic interaction of the Mn^{3+} cation with the crystal field. This produces a deformation of the MnO_6 octahedra, which are elongated in one direction and contracted in the other, as shown in figure 1.5(a).

As already mentioned before, the electronic configuration of the Mn^{3+} ion consists in a triplet occupying the degenerate t_{2g} orbitals, and a single e^- in the degenerate e_g orbital. In presence of a crystal field the e_g orbital is unstable and its degeneracy is lifted, leading to a change of the Mn-O-Mn bond. The Mn^{4+} ion is Jahn-Teller inactive, because of the absence of an unpaired e^- in the e_g orbitals. Therefore, a compound with a high concentration of Mn^{3+} ions is likely to have J-T distortions while a high concentration of Mn^{4+} ions should inhibit them. This observation has been confirmed experimentally, and orthorhombic structures are found for compounds with low doping or with oxygen deficiency, while the highly symmetrical rhombohedral structures are characteristic for high doping and higher oxygen content.

The J-T distortions play an important role in the structural phase diagram of manganites and have a great influence on their electronic properties [25, 26]. When the phenomenon of J-T distortions involves all the octahedra in the unit cell, a distortion of the whole lattice occurs, the so called *cooperative* J-T effect (shown in figure 1.5(b)). This effect is also frequently associated to orbital order, described below. The uncorrelated distortions, characterised by short-range order, are responsible for the presence of *polarons* i.e. short-range correlated electrons pinned by a local crystal distortion.

Charge order

The ratio Mn^{3+}/Mn^{4+} is responsible for the phenomenon of charge ordering (CO). This consists of a periodic distribution

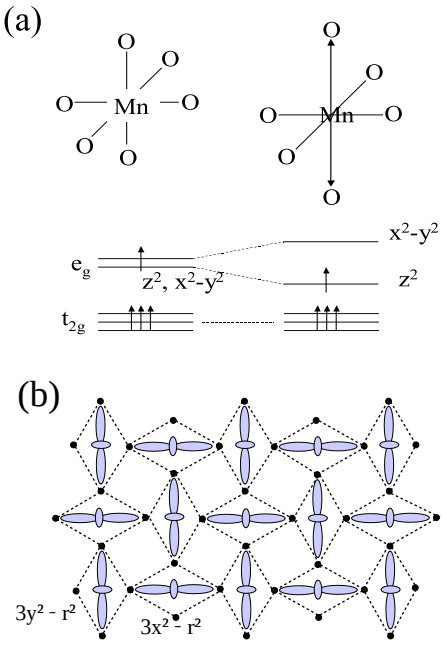

Figure 1.5: (a) Schematic representation of a J-T distortion. The change in Mn-O bonds is related to the lifting of the degeneracy of the e_2 level. (b) Cooperative jt distortions and resulting lattice

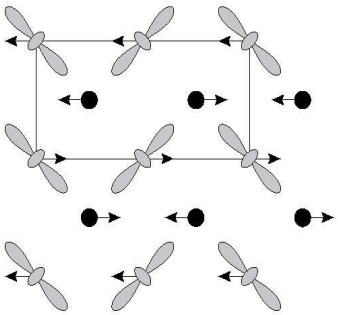

Figure 1.6: Two-dimensional scheme of OO and CO. The dots represent the Mn^{4+} ions, while the Mn^{3+} are represented by the orbital d_{z^2}. The sublattice of orbitals is highlighted by the solid line. The possibility of spin order is also shown.

of electric charge, i.e. Mn^{3+} ions, in the crystal lattice, driven by Coulomb interaction. The mobile electrons may become localised at certain Mn ion positions in the lattice, forming an ordered sublattice. CO is characteristic for special concentration of dopant, namely for rational fractions (as for example $x = 1/8,\ 1/2,\ 3/4$). In this case the extra fourth electron may be localised on alternate manganese ions in plane, creating an ordered path of charge in the lattice (as shown in figure 1.6). The CO can be either long-ranged or short-ranged. It is clear that CO is competitive with the electron conductivity, because it tends to inhibit the movement of the charges through the crystal. Compounds with long-range CO are generally insulating, but localised CO (polarons) is responsible for an enhancement of resistivity, introducing scattering centers for the mobile electrons. An indirect experimental method to detect CO is x-ray scattering[27, 28], which only detects the lattice displacement concomitant to the presence of pinned charge.

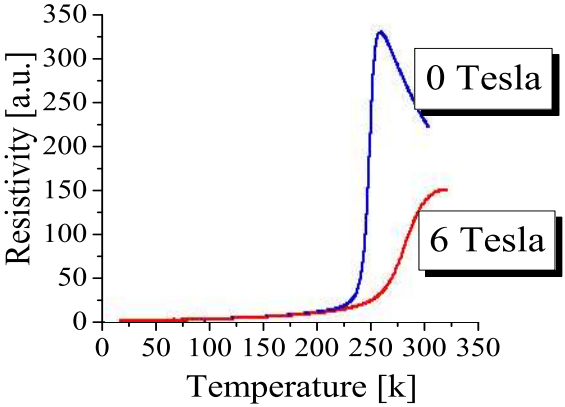

Figure 1.7: CMR

Orbital order

The orbital order (OO) consists in a spatially ordered arrangement of *d*-orbitals in the unit cell. Strongly associated with the carrier concentration, it develops when the *d*-electron occupies an asymmetric orbital. The direct electrostatic repulsion of the charge clouds coupled with cooperative J-T distortions, stabilises the effect generating an ordered sublattice of orbitals. Resonant scattering has been recently proposed as a technique to probe OO[29, 30]. However, the discussion of this technique is beyond the scope of this thesis and the reader is referred to the associated references for further details. A scheme of OO can be found in figure 1.6.

1.2.3 Colossal Magneto-Resistance

One of the reasons why the manganite compounds have received recently renewed interest is the discovery of the colossal

magneto-resistance effect (CMR), interesting for its potential application in electronic devices[14].

The CMR effect consists in a drastic reduction of the resistivity of a material in presence of an external magnetic field. Resistivity measurements vs temperature and applied magnetic field for $La_{1-x}Ca_xMnO_3$ are shown in figure 1.7. This effect appears only in the ferromagnetic metallic (FMM) region of the phase diagram (discussed later in section 1.3) and is maximum at the critical temperature T_C. An explanation of the CMR is possible within the theory of *double exchange* (DE) between $3d$ electrons, introduced by Zener in 1951[5]. The detailed explanation of such theory is beyond the scope of this work, in the following section we will introduce the basic idea of this model, referring to literature for more details[31, 32, 33, 34].

1.2.4 Double exchange model

As already discussed, the e_g level of the Mn ion has a two-fold degeneracy. A conventional basis for the orbitals is $\|3z^2 - r^2>$, elongated in the z direction and $\|x^2 - y^2>$ in the $x - y$ direction (see figure 1.8). Hybridisation of e_g orbitals leads to the formation of two bands, which can be treated as separate[37]. It is useful to define the hopping matrix T whose element $t_{ij}(ab)$ represents the hopping amplitude for an electron to go from an orbital a on the site i to the orbital b on the site j. Band calculations[38, 39] indicate that for these systems the elements t_{ij} are non-zero only for $i = j \pm 1$ and they are degenerate in the orbital space (a, b). This can be understood considering that the two nearest Mn orbitals do not overlap directly, so the hopping of the electrons requires virtual states through O sites. The intermediate states are the O-$2p_\sigma$ orbitals, which have a finite intersection with both kinds of Mn-e_g orbitals. In figure 1.8, the Mn and O orbitals are shown. It is clear that the overlap of e_g and O-$2p_\sigma$ orbitals is possible, being both directed along x and y directions, while no overlap is possible between O-$2p_\sigma$

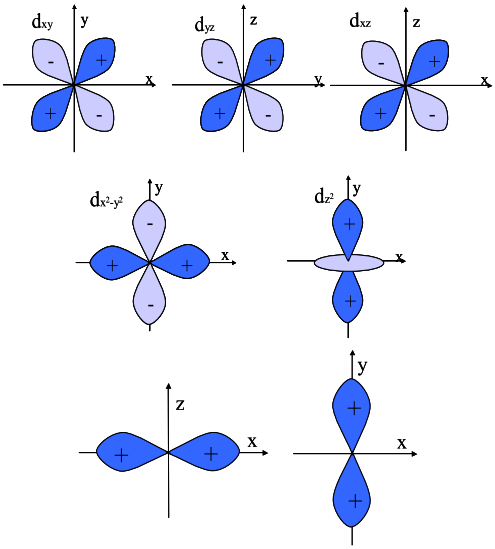

Figure 1.8: From the top to the bottom: d orbitals of the t_{2g} and e_g levels and and Oxygen $2p_\sigma$ orbitals in a Mn-perovskite crystal

and Mn t_{2g} orbitals. The main point of the DE model is the strong coupling between the electron motion and the magnetic order. The e_g electrons have their spin fully aligned with the core spin, via the strong Hund coupling. The hamiltonian of such interaction can be written as

$$H_{Hunds} = J_H \sum \vec{S}_{ci} \cdot d^+_{ia\alpha} \vec{\sigma}_{\alpha\beta} d_{i\alpha\beta}$$

which means that with a strong J_H factor, the hopping amplitude of an electron going from i to j (i.e. from a spin S_i to a spin S_j) is proportional to the quantum mechanical overlap

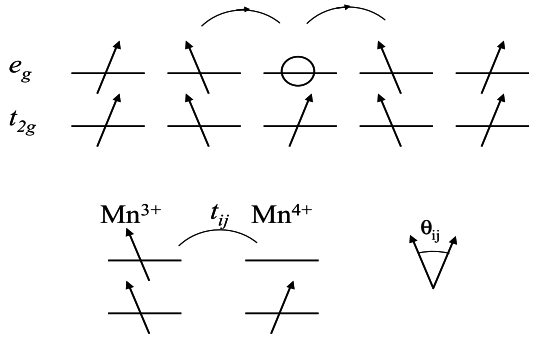

Figure 1.9: θ angle between Mn orbitals

of the two spin states which is maximal for parallel spins and minimal for anti-parallel. Therefore the electron hopping (hence conductivity) is favored in case of FM arrangement of spins. If one treats spins as classical objects, one can describe them by unit vectors $\vec{n}_i$ ad $\vec{n}_j$ and the polar angles $\theta_{i,j}$ and $\phi_{i,j}$. In this case the hopping amplitude depends on the polar angles. An over-simplified scheme of electron hopping from site i to the site j is shown in figure 1.9. This theory applies well to the manganite compounds, and explains the strong correlation between conductivity and ferromagnetism. If the manganese spins are not parallel or the bond Mn-O-Mn is bent, the electron transfer becomes more difficult and the electron mobility decreases. It is important to notice that because the triplet t_{2g} forms an electrically inert core spin, the density of the e_g electronic levels is $(1-x)$ and the electrons can travel through the crystal interacting with the core spin. In a classical approach one can define the following relation between conductivity and ferromagnetism:

$$\sigma = \frac{xe^2}{ah}\left(\frac{Tc}{T}\right)$$

where x is the doping, a the Mn-Mn distance. Generalising this relation for general spin direction, the transfer integral is

$$t = t_o \cos \frac{\theta}{2}$$

where θ is the angle between two adjacent Mn orbitals (see figure 1.9). Hence increasing the Mn-O-Mn bond angle θ the conductivity decreases.

1.2.5 Electron-phonon coupling in the CMR

As pointed out by Millis[40], the magnetic degree of freedom is not the only one to be taken into account for the complete explanation of the transport properties in manganites. The picture of strong interactions between electronic configuration and structural symmetry (e.g. J-T distortions) fits well the idea of Millis, which is that a perturbation of the crystal symmetry (buckling of O-Mn-O bond or rigid rotation of MnO_6 octahedra) might favor an overlap of orbitals. This can be responsible of a change in the hopping amplitude and consequently in the conductivity. This possibility has not been yet explored successfully[37].

The idea of Millis is that the one-electron approach used in the DE theory does not account for most of the properties of manganites, and for a more complete description of the physics of the manganites, the structural degree of freedom must be taken into account in the form of electron-lattice interaction. The strong electron-phonon coupling relative to the distortion of MnO_6 octahedra in the JT effect. "[...] may localise carriers, because the presence of an electron in a given Mn orbital causes local distortion which produces a potential minimum: this minimum tends to trap the electron in that orbital. If the coupling is strong enough, these tendencies lead to the formation of a self-trapped state called polarons"[41].

X-rays[42, 43, 44, 45, 46] and neutron scattering[42, 43, 47, 48, 49] studies performed on optimally doped CMR manganite sytems have demonstrated the existence of *polarons* in the

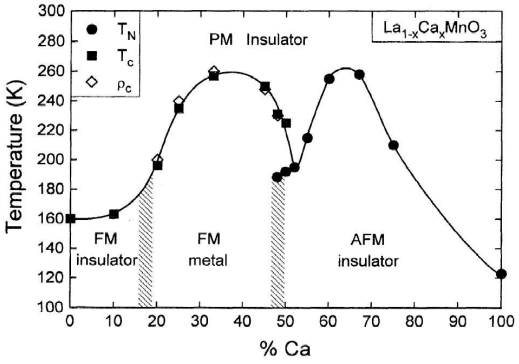

Figure 1.10: Phase Diagram of LCMO[56]

paramagnetic phase. This short range charge order, which disappears in the FM phase, is believed to be responsible for the insulating properties of the paramagnetic phase.

On the other hand, the complete suppression of J-T distortions following an insulator-metal transition for decreasing temperature[52] does not seem to be the driving force for the I-M transition.

Within the framework of the models proposed to explain the origin of CMR in manganites, we should mention the recently proposed *percolation mechanism*[53, 54, 55]. This model is based on the idea that the CMR manganites are "electronically *phase separated* into a sub-micrometre-scale mixture of insulating regions [...] and metallic, ferromagnetic domains" and that the CMR "can be explained by percolative transpor through the ferromagnetic domains"[53].

1.3 $La_{1-x}Ca_xMnO_3$ phase diagram

As we have highlighted several times in this chapter, the main characteristic of all the Mn-compounds is that the structural, transport and magnetic properties are strongly coupled and depend on the doping, as demonstrated by the phase diagram shown in figure 1.10.

The manganite compound relevant to this PhD work is $La_{1-x}Ca_xMnO_3$, hereafter referred to using the acronym LCMO for brevity. LCMO is a solid solution formed between the $LaMnO_3$ and $CaMnO_3$ end members of formal valence states $La^{3+}Mn^{3+}O_3^{2-}$ and $Ca^{2+}Mn^{4+}O_3^{2-}$ giving the mixed-valence $La_{1-x}Ca_x(Mn^{3+}_{1-x}Mn^{4+}_x)O_3$ compound. This compound is particularly interesting because it has one stable structure for the whole range of substitution, due to the high tolerance factor (the ionic radii of La^{3+} and Ca^{2+} being similar).

The end member parent compounds $LaMnO_3$ and $CaMnO_3$ are characterised by cubic structures. However, due to the mismatch of the cation radii, tilting of the oxygen octahedra occurs which together with local J-T type distortions produces the orthorhombic symmetry characteristic of the entire doping range.

The end members are both antiferromagnetic (AF) and insulating. In the low doping regime, for $x < 0.08$ the compound is AF, and it becomes a ferromagnetic insulator (FMI) for $0.08 < x \leq 0.2$. Upon further doping (for $0.2 < x < 0.5$) a ferromagnetic metallic (FMM) compound is formed. The minimum resistivity and the best ferromagnetism (highest Curie temperature T_C) coincide for $x \approx 0.3$. In the region of interest for this thesis, $x \approx 1/3$, the Curie temperature is $T_C \approx 280K$. The value of x= 1/2 is the boundary between the FMM phase and the AF and CO (insulating) phase persisting until $x = 7/8$, with maximum T_{CO} at $x = 5/8$.

One can explain the LCMO phase diagram in terms of hole doping of the $LaMnO_3$ compound (or electron doping of the $CaMnO_3$ end member)[57]. The initial Ca-doping corresponds

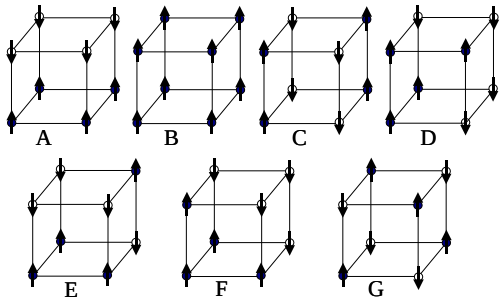

Figure 1.11: Possible types of magnetic order. In the magnetic F-type structure all the spins on Mn sites are aligned in the same direction. The A-type structure is one of the possible AF arrangements of spins. The spins are FM aligned in the $a-b$ plane and are AF coupled along the c direction. In the C-type structure the spins are FM aligned along the $< 110 >$ and $< 001 >$ crystallographic directions, with an AF alignment along the $< 100 >$ direction. The G-type structure is characterised by a fully AF alignment of spins. Each spin is surrounded by spins aligned in the opposite direction

to a hole doping in the e_g band, such that for small doping levels a canted antiferromagnetic (CAF) phase appears, along with weak ferromagnetism (with a very small saturation moment, $M_s \approx 0.15\mu_B$ per Mn-atom), mediated by itinerant electrons, via DE mechanism. When the doping increases the canted spins in the A-type magnetic structure (see figure 1.11[1]) of $LaMnO_3$ become canted further toward the c-axis direction up to the value $x \approx 0.1$. For $0.08 < x < 0.2$, the spins are FM aligned and, for temperatures below the T_C of the FM state, a CO

[1]Possible configurations of the spins in manganites are summarised in figure 1.11

state appears with a transition temperature T_{CO} maximum for $x = 1/8$. In this doping region the FM state is electrically insulating (FMI), while for doping $0.2 < x < 1/2$, the compound is paramagnetic (PM) and insulating at high temperatures, and undergoes a metal-insulator (M-I) transition at $T_{M-I} \approx T_C$ along with the PM-FM transition, showing the effect of CMR, as well. The optimal doping for the FMM phase is $x = 3/8$, and the saturation magnetisation in this region is $M_s \approx 3.7\mu_B/Mn$. CAF state appears for high hole doping until the end member $CaMnO_3$, which shows magnetic order of GF-type.

Certain special features appear at specific concentrations in the PD of LCMO (e.g. optimal doping for FMM phase, maximum T_{CO}, boundary between FM and AF phase). These features have a universal character, the doping level they are associated to, are independent of the particular compound. For example, the FM state is optimal (maximum T_C) for doping $x = 3/8$, and also $x = 5/8$ seems to be the highest T_c for the CO state in manganites. These anomalies at commensurate concentrations show once more the importance of the electron-lattice coupling in the manganite perovskites[15].

Given the strong interconnection between structure, magnetic and transport properties, one may expect that external perturbations such as strain induced from a substrate in thin films, can also affect these properties. This will be the subject of the next chapter.

Chapter 2

Manganite thin films: effect of strain of physical properties and structure

The expertise reached in the growth of high temperature superconductor (HTS) thin films with perovskite structure in the last decade, using the technologies implemented for semiconductors (such as sputtering, Pulsed Laser Ablation -PLA, and Molecular Beam Epitaxy -MBE), has been successfully applied to the growth of high quality crystalline thin films of Mn perovskites[58, 59]. The advantage of the use of thin films consists in the possibility of studying crystals with high perfection and a controlled amount of grain boundaries or defects. However, the presence of a substrate necessary for the growth of films introduces a new degree of freedom in the already rich landscape of variables, i.e. the external pressure in the form of epitaxial strain. This is why one of the major features of thin films is the strain induced change of the physical properties (structure, transport and magnetic order) compared to the bulk reference. Due to the fact that these changes are the main interest of this PhD work, we will describe the state of the art in the knowledge and

understanding of the influence of strain on physical properties of manganites as well as the problems still unanswered.

Before discussing the effects of strain on films, it is necessary to provide a brief introduction to the basic idea of thin film growth and epitaxy. A brief description of the principal effects of the strain on the structure and morphology of manganese perovskites will be given. Strain effects on the physical properties of manganites will also be discussed.

2.1 Perovskite thin films: Growth modes and epitaxy

A detailed description of the growth process goes beyond the purposes of this thesis. For this reason, in this section we will only briefly introduce the basic concept of film growth, and discuss the parameters important for the structural quality of the film. A more accurate description of the MBE[60] and PLA[61] systems, and more generally on the growth of perovskite thin films[62, 60], can be found in the reference papers.

2.1.1 Substrate and epitaxy

For the growth of a crystalline thin film the choice of the substrate is of primary importance. The basic requirements for the substrate can be summarized as follows:

- crystallographic lattice match with the Mn-compound
- similar thermal expansion coefficient
- absence of chemical interactions with the material to be deposited
- mechanical and chemical stability at the temperature and pressure conditions during the growth

In some cases the interaction between substrate and film can be mediated by an intermediate layer, called buffer layer. The presence of a buffer layer can be used to reduce the mismatch between film and substrate, or to prevent interdiffusion or chemical interaction between atoms of the substrate and the film. The criteria for the choice of the substrate described above apply also to the case of the buffer layer, and have to hold for both film and substrate.

The most commonly used substrates for Mn-compounds are $SrTiO_3$, MgO, $LaAlO_3$, which have perovskite structures with characteristics very similar to the Mn-compounds, and respond quite well to all the requirements listed above.

A film growing epitaxially on a mismatched substrate is characterised by the first atomic layers being elastically strained, in order to match the substrate lattice. When a *critical* thickness is reached, the elastic energy stored in the structure is enough to create structural defects, or cracks. The critical thickness d_c is related to the mismatch $\delta = (a_{Sub} - a_{film})/a_{film}$ (where a_{Sub} and a_{film} are the in-plane lattice parameter of respectively the substrate and film), the strain ϵ, the Young modulus of the film material Y and the energy released per unit length by a 2D crack E_s^* by the following formula[62]:

$$d_c = \frac{4E_s^*}{\pi Y \epsilon^2} \tag{2.1}$$

2.1.2 Growth techniques

The most common technique used for thin epitaxial oxide films is the growth from vapor phase, achieved in systems as MBE, PLA and sputtering. In these systems, the compound to be grown is evaporated from one or more sources, and the gas of atoms and molecules is directed toward a substrate kept at a controlled temperature. In a PLA system, which is the system used for the growth of the films studied in this thesis, the vapor of the compound to grow is generated by a pulsed laser beam

hitting the surface of a stoichiometric target. The gas generated, in the shape of a *plume*, as shown in figure 2.1, has the same stoichiometry of the target. The position of the substrate corresponds to the central part of the plume, to allow a uniform growth of the film. The stoichiometry of the target will be reproduced also in the film. The MBE system is more versatile. The growth of the film is obtained from the evaporation of the elements forming the compound desired, each being evaporated from a separate source. The advantage of using this technique is that it is possible to vary the concentration of the element and obtain films with different, and controlled, stoichiometry. The phase required is achieved by controlling in an accurate way the evaporation rates of each element, depending on its reactivity and on the concentration of each element in the compound desired. This makes the generation of the desired phase a complicated task.

For both of these deposition systems, epitaxial growth for complex oxides is generally achieved at a very high temperature, to increase the mobility of the atoms reaching the surface (adatoms), and facilitate an ordered growth. Typical temperatures of growth for perovskites are of the order of 500–600^o Celsius[62, 60], below the melting point of the compounds, but high enough to allow the diffusion of the adatoms on the surface. The deposition systems are generally ultra high vacuum (UHV) systems. The growth chamber must be *clean* and free from impurities to guarantee the purity of the phase of the films. The typical value of the pressure in a MBE or PLA deposition chamber is in the range 10^{-9}–10^{-11} Torr. Finally, essential to the growth of oxides it the presence of an Oxygen source, which provides molecular oxygen (O^2) or atomic oxygen, which is more reactive. Due to the presence of Oxygen gas the pressure in the chamber becomes as high as 10^{-4} during the growth.

The deposition chamber is often equipped with instrumentation useful to check the quality of the films *in-situ*, either during or after the growth. Reflection high energy electron diffraction

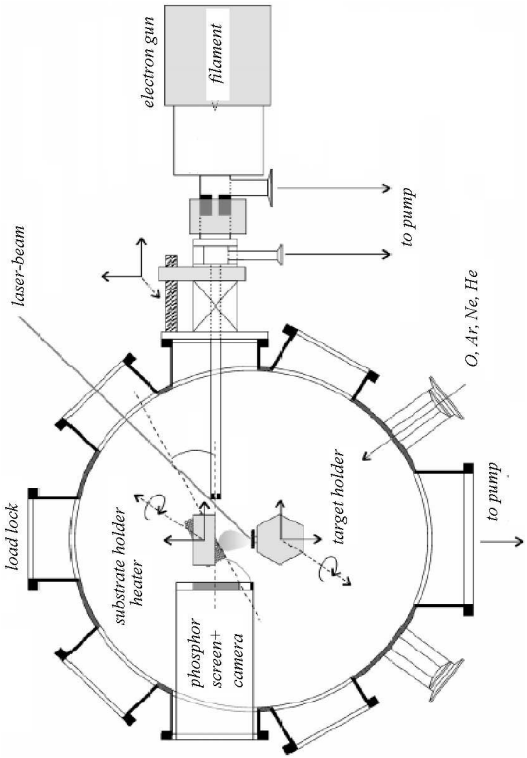

Figure 2.1: Scheme of a PLA system equipped with RHEED (electron gun)

(RHEED), as an example, is a surface-sensitive technique. It allows to check the crystal quality of the surface during the growth of the films, and it is often used as a feedback tool to modify the growth parameters, or stop the deposition for some minutes to allow the adatoms to diffuse on the surface and to order in a crystalline lattice[63]. It is also very useful to determine the growth modes, as illustrated in the next section. Other *in-situ* equipments often encountered in UHV deposition systems are atomic force microscope (AFM), used to check the surface morphology of the sample, low energy electron diffraction (LEED) to check the crystal quality of the surface, and a mass spectrometer, to control the concentration of the element during the growth. A detailed information about thin film deposition systems can be found in literature and review articles[62].

2.1.3 Growth modes

The epitaxial growth of complex oxide thin films - manganites, HTS and ferroelectric materials, is not fully understood. Nevertheless, the growth kinetics, surface morphology and formation of defects in complex oxide thin films are quite closely related to the epitaxially grown semiconducting systems. One of the most common mechanisms of the epitaxial growth is the 2D growth which depends both on the growth parameters and the substrate morphology. The *layer-by-layer* growth is characterised by the formation of 2D islands merging together in crystalline layers. It is typical for situation where the diffusion length of the ad-atoms on the surface of the substrate is smaller than the features of the substrate itself, as terraces and steps. It is illustrated in figure 2.2(b). The RHEED intensity oscillates in time, being maximum when the coverage of the surface is maximum, and minimum when 50% of the surface is covered. Every oscillation indicates the growth of *one* layer. If the diffusion length of the ad-atoms is larger than the terrace length, the ad-atoms attach on the edges of the terraces generating the so called *step-*

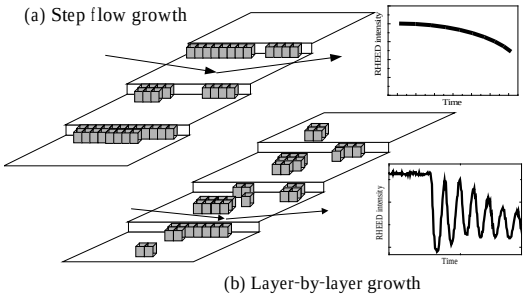

Figure 2.2: Growth modes and RHEED signal

flow growth. In this case the RHEED signal is constant in time (figure 2.2(a))

2.2 Manganite films

As we have already pointed out, for the manganese perovskites the separation of the structural, magnetic and transport properties is merely artificial, these properties being in reality strongly coupled. Here, for the sake of simplicity, the description of structural and other physical properties of manganite thin films will be discussed in separate sub-sections. Where possible, the structural features of the films and their transport and magnetic properties, will be considered with respect to the strong links existing among them. The important point in the discussion of thin films is the change in physical properties introduced by the intrinsic parameter of dimensionality of the film and also from the strain induced by the substrate.

2.2.1 Substrate and mismatch

In order to control the structural properties of a thin film, the choice of the substrate is crucial. The mismatch δ between the substrate and the compound to be deposited is defined as

$$\delta = \frac{a_{Mn} - a_{sub}}{a_{Mn}}$$

where a_{Mn} is the bulk in-plane lattice parameter of the Mn-compound to deposit and a_{Sub} is the one of the substrate. The mismatch represents the measure of the mechanical strain applied to the crystal structure of the film, which is the main cause of the modification of the film properties with respect to the bulk. For manganese perovskites the most common substrates used are high quality perovskite crystals, such as $SrTiO_3$ (STO), $NdGaO_3$, MgO and $LaAlO_3$, due to their similar structure and lattice parameters. In the case of LCMO deposited on $< 001 >$ oriented STO substrate (which is also the case of the samples studied in this work) the mismatch is about 1% (1,1% in the case of 1/3 doping) leading to a tensile strain, because the in-plane lattice parameters of bulk LCMO are shorter than those of STO. The LCMO compound, with $x = 1/3$, is orthorhombic with lattice parameters $a = 5.47$Å, $b = 5.49$Å and $c = 7.74$Å[64]. However, because LCMO grows on STO with the a_{LCMO} along the $< 110 >$ of the STO, it is useful refer to the LCMO structure as a *pseudo-cubic* one. The pseudo-cubic unit cell contains only one forlula unit (contrarily to the orthorhombic one which contains 8 formula units) and its lattice parameters a_{pc} and b_{pc} rotated by 45^o in the orthorhombic a-b plane and have a value of $a_{pc} = 3.87$Å.

As learned from the semiconductor industry, the value of δ gives a measure of the critical thickness for the epitaxy. However, the formula used in that case is not applicable to the perovskite structures, for the reason that the way to accommodate the strain from the two categories of structures is quite different due to energetic considerations. For example the maximum

value of mismatch for the epitaxial growth seems to be smaller for perovskite structures than for semiconductors. For the latter case, the epitaxial relation between two materials is still present with values of $\delta \approx 6\%$, while a value of 1.5% is already quite significant for perovskite structures.

2.2.2 Accommodation of the strain

The way a perovskite structure accommodates strain is mainly using the internal degrees of freedom of the lattice, i.e. by rotation of MnO_6 octahedra, or small modifications of the Mn-O bond lengths, leading to J-T type distortions (as described in section 1.2.2, page 32). Moreover, large variations of the unit cell lattice parameters are rather unusual, being energetically unfavorable. On the other hand, other mechanisms to relief the strain such as stacking faults, defects, are quite common in perovskites, together with other processes such as adsorption of oxygen at the surface or at the interfaces.

Moreover, for doped compounds one has to consider a further possibility. As already discussed in the previous chapter, for Mn-compounds small changes in stoichiometry lead to changes in the structure and consequently in the lattice parameters. Therefore, for films of such materials it is possible to include the change in stoichiometry in the list of the possible ways to relax the strain. Such variation would lead to a change of the lattice parameter to favour a matching of the film structure with the substrate. This may easily occur during the growth from vapour phase, due to the possibility of the atoms of rearranging on the surface of the template-structure of the substrate. This kind of 'strain relaxation' effect may result is a gradient of the doping concentration through the thickness of the film, which relieves the elastic strain preserving the epitaxy. We will discuss about this possibility in the chapter 6 dedicated to the experimental results.

For the manganites variations of the structure are strongly

connected with changes in physical properties. Therefore one expects the presence of the substrate alone to significantly influence the physical properties of the films making them different from the bulk. This will be discussed later, in sections 2.4 and 2.5. In the following we briefly describe what is already known about the strain induced structural changes in thin LCMO films.

It is important to emphasize that a general determination of the structural properties of these compounds with respect to parameters such as thickness and strain is quite difficult, if at all possible. This is because of the extreme sensitivity of the film properties to the details of growth process itself. Finally, a sensible comparative study among films vs. a chosen parameter is possible only for films made in the same growth conditions of pressure, temperature, deposition rate, etc. The growth conditions need to be extremely well controlled for the production of high quality crystalline films. In this respect it is easy to understand why one of the most important parameters in the growth of films turns out to be the grower him- or herself[65].

From the comparison of several systematic studies performed on thin films, it is only possible to extract a quite general picture of the trend of their physical properties. It is not possible to estimate absolute numerical values of critical thickness for strain induced effects (i.e. modified physical properties such as transport, magnetism or epitaxy). Only general features can be described which have a general significance. In this respect, it is also worthwhile spending few more words about the use of the adjectives *thin* and *thick*. The word *thin* is generally referred to films with thickness of few unit cells, with properties strongly different from the bulk. In this case it is the dimensionality and the strain, rather than the composition, which plays the essential role in the determination of their physical properties. In the same way the use of the word *thick* is generally referred to those films whose properties approach the behaviour of the bulk and are not prevalently characterised by strain. That it to say that the property of *thin* and *thick* is not intrinsic and can-

not be separated from other physical properties. Nevertheless a film made of few mono-layers is unmistakably thin, as well as is definitely thick a film of few thousand Å.

2.3 Morphology and microstructure of LCMO thin films

LCMO films in the region of optimal doping for the FMM phase, grown on STO, are subjected to *tensile* strain. This is due to the mismatch of about 1.1% between the lattice parameter of LCMO ($a_{pc} = 3.87$Å) and the larger lattice parameter of the cubic STO ($a_{STO} = 3.905$Å). In the epitaxial growth of LCMO on STO, the good match of the in-plane lattice parameters might induce a tetragonal structure of the film, instead of the orthorhombic of the bulk. In some cases monoclinic type distortions have been detected[66, 67]. The preferential growth direction of LCMO films on STO is with the long axis (c in the Pbnm, b in the Pnma space group), i.e. the direction of maximum mismatch between the two structures, parallel to the surface normal[64]. The presence of domains (described in section 1.1.2 at page 29) with different orientation and twins along the $< 110 >_o$ (using the Pbnm space group, i.e. $< 101 >_o$ using Pbnm space group) direction is also very common. From an energetic point of view the $< 110 >_o$ is the favorable direction for twins.[1] Finally, the presence of dislocations at the film-substrate interface is another possible way to relieve the mismatch strain.

Films of very good crystalline quality, with thickness generally not exceeding few hundreds Angstroms, which are fully epitaxial and coherently strained, have been grown. In absence of dislocations at the substrate-film interface, domain distribution and twinning can appear, to relieve the strain. Few cases are reported in literature where the twinning makes defined pat-

[1] For a more detailed description of twins we refer the reader to chapter 5

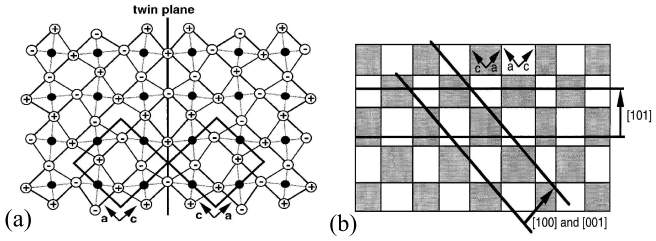

Figure 2.3: (a) Model of structure of strained thin films of LCMO, with J-T distortions, from Zandbergen et al.[64] (b) Chessboard-like arrangement of twin domains in strained thin films. Note that in this case the Pnma space group is used

terns in the film, which can be chessboard like (cf reference [64]), or columnar[68, 69]. Two relevant works for the research presented in this thesis, are those of Zandbergen and of Lebedev. These works show strong similarities with the results we report in this PhD thesis. Below we briefly summarise their findings.

Zandbergen et *al.*[64] report on transmission electron microscopy (TEM) studies of the microstructure of thin LCMO films grown on STO by PLA. Films thinner than 120Å are characterised by full epitaxy and structural distortions, while thicker films are found to have a bulk-like structure relaxed by the presence of interfacial dislocations. Moreover in the thin films no relevant tilts of MnO_6 octahedra, typical of the orthorhombic bulk structure, have been detected with electron diffraction (ED) refinement. Instead, an elongation of the Mn-O-Mn bonds along the c-axis has been found, representative of a Jahn-Teller distortion and only rarely observed in bulk[70]. For the thicker films, the dislocations observed at the interface relax the substrate-induced strain, breaking the epitaxial relationships with the substrate and leading to a bulk-like structure without distortions. Also, in the very thin films periodic twin boundaries are

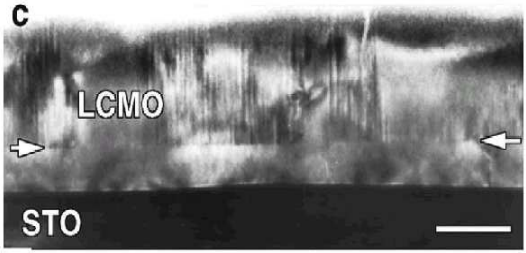

Figure 2.4: TEM image[68]of a thin film of LCMO, epitaxially grown on STO. The formation of columnar domains is shown. See text.

measured along the plane perpendicular to the interface and extending throughout the whole thickness. The average domain size, increasing with thickness, is in the range of 100–300Å with a broad distribution. The reason for the twinning observed in the thin films has been ascribed to the minimisation of the interfacial energy. Due to the different tilts of MnO_6 and to the J-T type distortions, the in-plane lattice parameters a and c (Pnma space group) have slightly different lengths. Consequently, the interchange of domain orientation, with twin boundary parallel to $< 101 >$, minimises the mismatch energy (due to the cubic symmetry of the STO).

In comparison, the work of Lebedev et *al.*[68] reports on TEM studies of the thickness dependence of the structure of LCMO films. The microstructure of the two films studied, of thickness 100Å and 2000Å, seems to be very different. Unlike the previous case, the very thin film consists in separated islands, while the thick film is found to have polyhedral columns perpendicular to the crystal surface, whose shape and coherence depends on the growth conditions (temperature of deposition). The highest quality film consists of a 1000Å epitaxial layer at the interface with the STO, without dislocations. The remain-

ing volume is comprised of in-plane twin domains, which are coherent along the surface normal, and form a columnar structure separated by anti-phase boundaries (APB's). The twin domains size is randomly distributed. Electron diffraction refinement suggests the presence of a monoclinic type of structure, with space group P21/c[68]. In another work[69] Lebedev et *al.* report a periodic twin domain distribution in thin films of LSMO. A similar modulated in-plane structure is found in the LCMO films presented in this thesis, which shall be discussed in chapter 5.

2.4 Transport properties of strained thin manganite films

There appears to be no general trend in the change of strained films properties, which strongly depends on the compound considered and the doping x. For example, bulk $La_{0.8}Sr_{0.2}MnO_3$ is FMI with $T_C \approx 150K$. However, films with thickness less than 250Å deposited on STO substrate are compressively strained and have a higher $T_C \approx 200K$[12] as well as an unusual metallic behaviour in the FM state. Strained thin films of LCMO compound ($x = 1/3$), on the other hand, shows a strong reduction of T_C (the bulk value of 280K is suppressed to $\approx 100K$ in thin films). Furthermore, the compound becomes insulating for very small thickness[71], while in the bulk the PM-FM transition is accompanied by a metallic-insulator transition (i.e. above T_C the resistance increases for decreasing temperatures, and decreases with decreasing temperatures below T_C). In few cases, a decoupling of the T_C and the T_{M-I}, which increases with decreasing thickness, has been detected[72].

Once more we would like to stress the absence of generality in the results of film properties vs. thickness. In some cases[74, 75] films of few tenth Å of thickness show a bulk-like behaviour (bulk T_C and transport properties), loosing all the strained-

induced *thin film* characteristics. In other cases[71, 72, 73], for films of the same compound, the condition of strain and epitaxy persists up to a thickness as high as $\approx$ 1000Å (in this case considered still a *thin* film), the film only becoming bulk-like for thickness higher than $\approx 1000 - 2000$Å . This demonstrates once more the arbitrariness of the use of the words thin and thick, and the extreme sensitivity of film properties on the growth.

Interesting studies on the effect of strain induced by different type of mismatch, and the importance of lattice distortions in the transport properties has been performed by several authors[76, 77, 78].

2.5 Anisotropy of physical properties

Among the characteristics of epitaxial strained films of Mn compounds is the introduction of anisotropy in the physical properties [73, 79]. Such anisotropy shows up together with the structural changes, which bring important modifications in the transport and magnetic properties as well. For thin films of FM Mn-compounds different authors[80, 81, 82] report a change in the symmetry of magnetic properties in bi-axially strained thin films. The isotropy of the magnetic properties of the bulk is changed in favor of anisotropy in the films. In particular the appearance of the so called magnetic *easy* and *hard* axis, defined respectively as the crystallographic directions where the coercive field is respectively smaller or larger. This effect, completely absent in the bulk, is ascribed to the epitaxial strain. From a comparative study between films with tensile and compressive strain, due to the different sign of the substrate mismatch δ, it has been found that a tensile in-plane biaxial strain is responsible for the appearance of an easy-plane, which coincides with the plane of the tensile strain. A compressive strain, on the other hand, produces the appearance of the easy-axis in the direction of the surface normal. In the case of the film studied for this PhD work, as we will see in detail in the chapter 4,

also the symmetry of the transport properties is affected by the strain[71].

But what is the physical role of the strain? How does it act on the structure and the electronic properties of these compounds, leading to such effective changes? This is a question difficult to answer and has been the subject of many recent publications[83, 84, 85].

Some of the results of this thesis provides more information to answer this question.

Chapter 3

Experimental techniques

Scattering of x-rays and neutrons has been extensively used in this work, for the study of structural properties and magnetic profile of the strained thin films of LCMO. In particular, polarised neutron reflectivity measurements (PNR) have been used to study the magnetisation profile of the thin films, while x-ray Bragg scattering has been used to analyse their crystal structure.

This chapter is dedicated to the description of the techniques used in this work for the structural study of the films. The principles of X-ray diffraction and neutron scattering will also be introduced. In the last section, a brief description of the experimental setup used for the x-rays and neutron experiments will be given.

3.1 Scattering of x-rays and neutrons

Due to the crystalline nature of our samples, we can describe the real-space structure in terms of crystal lattice vectors $\vec{i}$, $\vec{j}$ and $\vec{k}$. A crystal is a periodic arrangement of atoms and the unit cell of a crystal is the minimal group of atoms which represents this periodicity. By repeating it in all three crystallographic

directions, the entire lattice is formed. The unit cell is defined by three vectors $\vec{a}$, $\vec{b}$ and $\vec{c}$ which represent the minimum periodicity of the crystal in each of the three crystallographic directions $\vec{i}$, $\vec{j}$ and $\vec{k}$. These form the basis of the reciprocal space:

$$\vec{a} = a \cdot \vec{i}$$
$$\vec{b} = b \cdot \vec{j}$$
$$\vec{c} = c \cdot \vec{k}$$

The reciprocal lattice is built from the real-space, and is defined by the three following vectors:

$$\vec{\tilde{a}} = \frac{\vec{b} \wedge \vec{c}}{\vec{a} \cdot \vec{b} \wedge \vec{c}} \tag{3.1}$$
$$\vec{\tilde{b}} = \frac{\vec{c} \wedge \vec{a}}{\vec{a} \cdot \vec{b} \wedge \vec{c}} \tag{3.2}$$
$$\vec{\tilde{c}} = \frac{\vec{a} \wedge \vec{b}}{\vec{a} \cdot \vec{b} \wedge \vec{c}} \tag{3.3}$$

The scattering of an electromagnetic wave with wavelength λ of the order of the atomic spacing in a crystal (e.g. x-rays, electrons, neutrons), can be described in terms of intensity distribution in the reciprocal space. Such distribution contains information about the crystal structure, including position and nature of the atoms present in the crystal (i.e. structure factor).

The scattering process involves the vector of the incident and the scattered wave, respectively $\mathbf{k}_i$ and $\mathbf{k}_f$, which define the momentum transfer $\mathbf{Q}$ in the following way:

$$\mathbf{Q} = \mathbf{k}_i - \mathbf{k}_f$$

In the following we will only consider elastic scattering, i.e. a process which does not involve loss of energy of the impinging radiation. The condition of elasticity is that the wavelength of

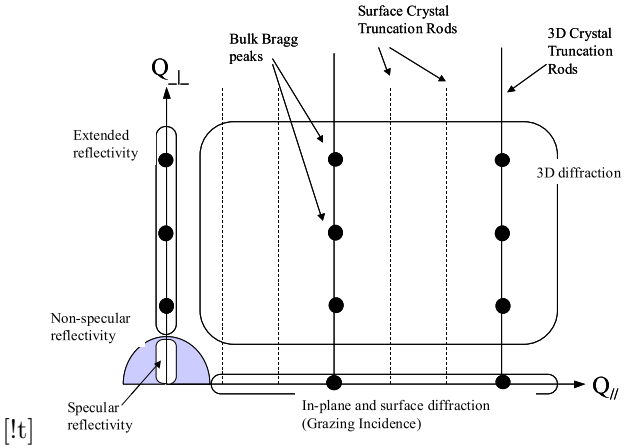

[!t]

Figure 3.1: Reciprocal lattice map showing reflectivity region, bulk scattering, in-plane peaks CRTs

the scattered and incident wave are the same:

$$\lambda_i = \lambda_f$$

Figure 3.1 shows a sketch of the reciprocal space map of a crystalline sample with a surface parallel to a set of crystallographic planes (we will see that the presence of a surface is associated to specific features in the reciprocal lattice). The coordinate system for the reciprocal space have been chosen, for simplicity, to be the vectors $\mathbf{Q}_{//}$ and $\mathbf{Q}_{\perp}$ i.e. the components of the momentum transfer $\mathbf{Q}$ respectively parallel and perpendicular to the scattering plane. In this way we can clearly separate in the diagram regions which are accessible with different scattering techniques.

The region close to $\mathbf{Q}\approx 0$ is the reflectivity region; the specular part ($\mathbf{Q}_{//} = 0$) is governed by the Fresnel laws (see next paragraph), while the non-specular reflectivity region ($\mathbf{Q}_{//} \neq 0$)

is governed by elastic diffuse scattering which we will not analyse in this work. For higher momentum transfer satisfying the condition $\mathbf{Q}_{//} = 0$, we get into the region of the extended reflectivity, where the Fresnel laws are not anymore sufficient to explain the scattering profiles, and the Bragg diffraction has to be taken into account. The region with $\mathbf{Q}_{//} \neq 0$ and $\mathbf{Q}_{\perp} = 0$ is the region of in-plane surface diffraction, accessible via grazing incidence diffraction (GID) technique, which will be described later, in section 3.5. Finally the area with both $\mathbf{Q}_{//} \neq 0$ and $\mathbf{Q}_{\perp} \neq 0$ is where the peaks from the 3D crystal arise, i.e. Bragg peaks from 3-dimensional crystal lattice. Moreover, in the 3-D diffraction area, rods of intensity perpendicular to the crystal surface are also present, due to the presence of the surface. These streaks of intensity, firstly studied by J. Robinson in 1985, are called Crystal Truncation Rods (CTR) and are discussed in more detail in section 3.4.

3.2 Reflectivity from X-Rays and neutrons ($\mathbf{Q} \approx 0$)

We now describe the elastic scattering of an electromagnetic wave giving rise to intensity in the specular reflectivity region with $\mathbf{Q} \approx 0$ in the reciprocal space map shown before. The refraction index n of the material (M) interacting with the wave is the main cause for the reflection and refraction processes. For a homogeneous material it is

$$n = \delta + i\beta \tag{3.4}$$

where β describes the absorption of the radiation from M (which is of the order of 10^{-6} for x-rays, and in most cases negligible for neutrons), and δ accounts for the change of the group velocity of the electromagnetic wave inside the material. The latter depends on the electronic density in the case of x-rays, and the nuclear density for the neutrons. Due to the fact that x-rays

and neutrons are sensitive to different physical quantities, they can be used as complementary techniques in the study of the materials.

Here we report the expression of δ and β for the x-rays and neutron refraction index for non-magnetic substances:

$$\delta_x = \frac{r_0\lambda^2}{2\pi} N_A \sum \frac{\rho_i}{A_i}(Z_i + f_i') = \frac{r_0\rho^{el}\lambda^2}{2\pi} \tag{3.5}$$

$$\beta_x = \frac{r_0\lambda^2}{2\pi} N_A \sum \frac{\rho_i}{A_i} f_i'' \tag{3.6}$$

$$\delta_N = \frac{\lambda^2}{2\pi} N_A \sum \frac{\rho_i b_i}{A_i} \tag{3.7}$$

In the previous equation N_A is the Avogadro's number, ρ_i the mass density of the element i with atomic number Z_i and atomic mass A_i. r_0 the classical electron radius, f' and f'' the real and imaginary anomalous dispersion factors for the element i. Finally ρ^{el} is the electronic density and b_i the neutron scattering length.

Snell's law expresses the refraction index as follows:

$$n = \frac{\cos\alpha_i}{\cos\alpha_t}$$

the angles α_i and α_t, illustrated in figure 3.2, being respectively the angle of incidence of the wave (with wave vector k), impinging on the surface of M and the angle of the wave transmitted in the medium M. The critical angle α_c is defined as the angle for which the transmitted wave disappears and the regime of total reflection occurs. It is expressed as $\alpha_c \approx \sqrt{2\delta}$[86].

For the condition of continuity of the tangential component of the electric and magnetic field at the interface[86] between M and the vacuum (or another material) one finds the following relations for the z-component of the wave vector of the incident (k_i) and transmitted wave (k_f):

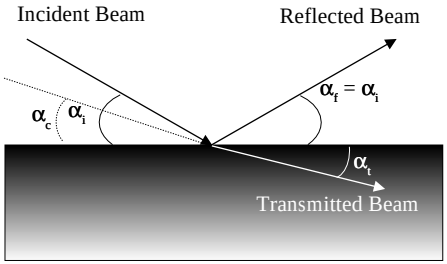

Figure 3.2: Snell's law

$$k_{i,z} = k \sin \alpha_i \tag{3.8}$$

$$k_{t,z} = k\sqrt{n^2 - \cos^2 \alpha_i} \approx k\sqrt{\alpha_i^2 - \alpha_c^2} \tag{3.9}$$

The amplitude of the transmitted and the reflected waves are respectively the Fresnel coefficients[86] T_F and R_F, which are expressed by the following formulas:

$$R_F = \frac{k_{i,z} - k_{t,z}}{k_{i,z} + k_{t,z}} = \frac{\alpha_i - \alpha_t}{\alpha_i + \alpha_t} \tag{3.10}$$

$$T_F = \frac{2k_{i,z}}{k_{i,z} + k_{t,z}} = \frac{2\alpha_i}{\alpha_i + \alpha_t}$$

where $\alpha_t = \sqrt{\alpha_i^2 - \alpha_c^2}$. For $\alpha_i > \alpha_c$ the intensity of the reflected waves is $R(Q) \approx \alpha_i^{-4}$[86].

In the extreme case of the incident angle being smaller than the critical angle ($\alpha_i < \alpha_c$) the vector $k_{t,z}$ becomes imaginary (cf equation 3.9) and the transmitted wave travels parallel to the surface of M with an amplitude which decreases exponentially

with increasing depth, described by the following formula

$$E = e^{-z/\Lambda} \tag{3.11}$$

and is called *evanescent wave*[87].

In the case of the material M being a film with thickness T_{film}, the intensity of a reflectivity profile is given by the Fresnel-reflectivity plus the Kiessig fringes coming from the interference between the waves scattered from the surface of the film and the interface with the substrate, as shown in the upper part of figure 3.3(b). These waves have different amplitude due to the difference in the e^- or nuclear density between film and substrate (and never depend on the crystallinity of the materials). The distance between two consecutive maxima (or minima) of the Kiessig fringes, calculated in momentum transfer units Q, is directly related to the thickness of the film T_{film} by the formula

$$T_{film} = 2\pi/\Lambda \tag{3.12}$$

$$\Lambda = Q_j - Q_{j-1} \tag{3.13}$$

It is important to notice that in a multilayer structure where a certain number of layers L, each with thickness d_i, is repeated J times the reflectivity profile has a peculiar shape, presenting fringes relative to the total thickness of the film ($T_{film} = J * \sum_i^L i * d_i$) and an additional periodicity due to the thickness of each repetition in the film ($T_{period} = \sum_i^L i * d_i$), as shown in figure 3.3(b). Note that in the case we are analysing the momentum transfer has only a component along the surface normal z, and the reflectivity profile is sensitive only to the electron (or nuclear) density along the z-axis.

The Parratt formalism[88] is widely used to analyse the reflectivity. For a succession of N slabs, each of thickness d_j (as the one schematised in figure 3.3(a)), and with uniform density ρ_j^{el} and b_j (for x-rays and neutrons respectively) the formula for the reflectivity is the following

$$\frac{R_j}{T_j} = e^{-2ik_{z,j}z_j} \frac{R_{j,j+1} + X_{j+1}e^{2ik_{z,j+1}z_j}}{1 + R_{j,j+1}X_{j+1}e^{2ik_{z,j+1}z_j}} \tag{3.14}$$

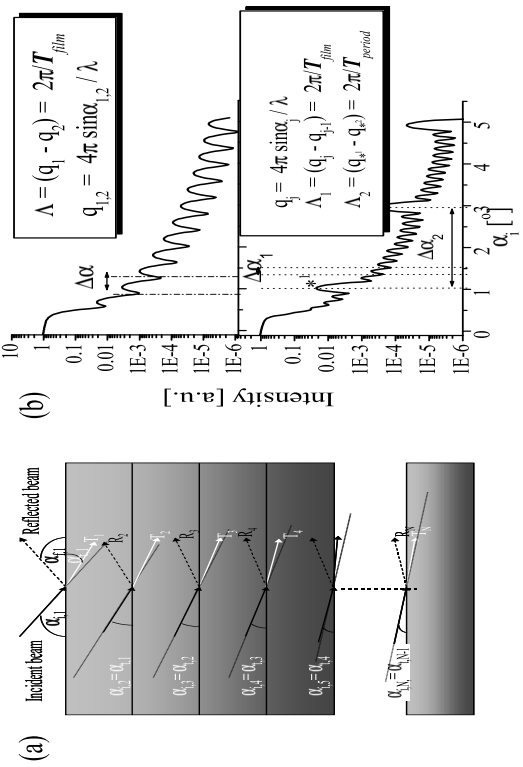

Figure 3.3: (a) Scheme of reflection and transmission coefficient in a multilayer structure (b) Kiessig fringes from a single layer and from a multilayer with periodicity T_{period}.

where $R_{j,j+1}$ and T_j are the Fresnel coefficients described in the equations 3.10.

3.2.1 Polarised neutron reflectivity

The index of refraction for neutrons changes in the case of magnetic materials. The neutrons are uncharged particles with spin $s = 1/2$, and the capability of interaction with a magnetic field makes them a suitable probe of the magnetism of a material. For this purpose it is possible to use both polarised and unpolarised neutron beams. In the first case all the neutrons in the beam have a well defined spin direction, in the second, the direction of the spins is undefined. The advantage of the use of a polarised beam is the possibility of the detection of both magnitude and direction of the field of magnetic induction $\vec{B}$ inside the sample analysed.

In presence of magnetic induction $\vec{B}$, in fact, (due to the magnetization of the sample) the interaction potential for the neutrons becomes:

$$U(z) = U_n(z) + U_m(z) = \frac{\hbar^2}{2m} N(z)b(z) + \vec{B} \cdot \vec{s} \qquad (3.15)$$

where $\vec{s}$ is the spin operator which represents the two possible spin states for a neutron ($\pm 1/2$), $U_n(z)$ and $U_m(z)$ are respectively the nuclear and magnetic potential of the material. Knowing the polarisation of the incident neutrons and measuring that of the scattered neutrons permits to determine the interaction between neutrons and the magnetic field of the sample probed.

In a polarised neutron reflectivity (PNR) experiment the polarisation of the neutron beam is achieved using an external polarisation field $\vec{H}_p$ (cf figure 3.4). This is generally achieved using polarising mirrors[89]. A *spin-flipper* positioned after the polariser and before the sample, is used to rotate the spin of the neutrons by 180^o in such a way the neutron beam impinging on the surface of the sample can have spin either parallel

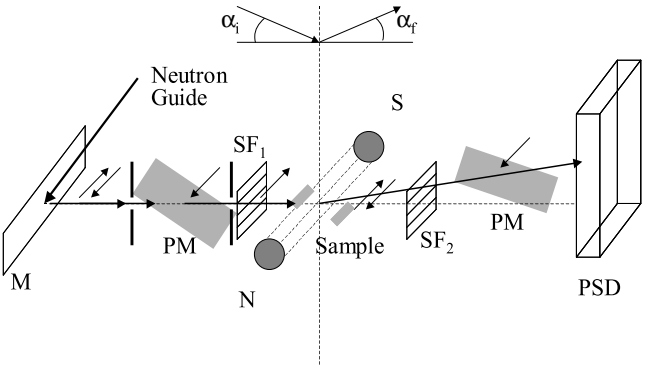

Figure 3.4: Scheme of the setup of a PNR experiment. Polarising mirrors (PM), spin flippers (SF), monochromator (M), postion sensitive detector (PSD), magnetic field and sample are shown. Note that the polarisation field, the magnetic induction of the sample and the guide field are all aligned in the same direction

or anti-parallel with respect to $\vec{H}_p$, and the neutrons are said to have respectively spin state *up* (+) or *down* (-). Therefore the second term in the previous equation is equal to $\mu \cdot B$, with $\mu = \pm 1/2$ being the absolute value of the magnetic moment of the neutrons. Upon interacting with the field of magnetic induction $\vec{B}$, the neutrons may change their spin state, (in classic terms the spin of the neutron precesses about $\vec{B}$). Analysing the spin state of the neutrons after the interaction allows us to determine the induction $\vec{B}$ (i.e. the magnetisation $\vec{m}$ inside the sample). It is important to notice that in a PNR experiment all the magnetic fields are aligned in the same direction, i.e. a

guide field is present which is a reference for the spin state of the neutrons. For some experiments also at the sample position an external magnetic field $\vec{H}_{ext}$ is applied (for example to saturate a ferromagnet) which can be parallel or anti-parallel to the *guide field*.

The final state of the neutrons after the interaction with the sample, is detected with the use of an analyser, i.e. an external known field $\vec{H}_a // \vec{H}_p$. The most commonly used analysers are supermirrors[90], but other methods such as He^3 analyser are also used[91]. The analyser selects the neutrons with a defined spin state, i.e. the ones with spins parallel to $\vec{H}_a$. Due to the fact that the direction of $\vec{H}_a$ is fixed, a second *spin-flipper* is positioned after the sample, which allows the analysis of the spin of the neutrons with both spin states *up* or *down* ($+$ or $-$). Due to direction of the magnetic moment $\vec{m}$ inside the sample, part of the neutrons of the reflected beam may keep the same spin state as before the interaction, say $+$, and part may change spin state, to $-$, giving rise to different reflectivity profiles. Depending on the sign of the polarising and analysing fields $\vec{H}_p$ and $\vec{H}_a$ (i.e. by the use of *spin-flippers*) 4 reflectivity profiles can be measured. These curves are conventionally labeled with R^{++}, R^{--}, R^{+-} and R^{-+}, with the two signs $+/-$ indicating the spin state of the neutrons before the interaction (the first) and the spin state after (the second). To obtain the curve R^{++} (R^{--}), as an example, the neutrons of the incident beam must have spin *up* (*down*) and the intensity measured is that of reflected neutrons with spin *up* (*down*). Therefore, the curves R^{++} and R^{--} represent the intensity of the reflected neutrons with unchanged spin state after the interaction with the sample. On the other hand, the curves R^{+-} and R^{-+} are the measure of the intensity of the reflected neutrons with spin state changed after the interaction. The presence of spin-flip scattering indicates that in the sample is present a component of the magnetic moment $\vec{m}$ which is transversal to the *guide field*[89].

In the case the reflected beam is not analysed, the final spin

state of the neutrons is not known and the measured curves R^+ and R^- are obtained, generally different from R^{++} and R^{--}. However, if the component of $\vec{m}$ transversal to the *guide field* is zero, all the scattered neutrons keep the same polarisation of the incident neutron beam and the intensity of the curves R^{+-} and R^{-+} is also zero. In this case the reflected curves R^+ and R^- are equivalent respectively to R^{++} and R^{--} and the presence of the analyser is unimportant.

Finally, it is important to stress that for a sample with the surface lying in the plane of polarisation, the component of $\vec{B}$ perpendicular to the surface do not influence the final spin state of the neutrons, consequently they cannot be determined by a PNR experiment.

3.2.2 Parratt and Matrix approach

Compared to other techniques, such as SQUID measurements, which detect the average magnetisation M of the material, PNR measurements are suitable for measuring the *structure* of the magnetic profile inside the sample. They have been successfully applied to study the magnetic coupling in multilayered structures[92], or for samples with non-uniform magnetic profiles. Information about the magnetic structure is obtained from the comparison between the reflectivity curves measured with different combination of the sign of the magnetic field $\vec{H}_p$ and $\vec{H}_a$, as described in the previous section.

The formalism used for the analysis of PNR data is generally the Parratt formalism, deduced by equation (3.14), with the only difference that the latter does not include the spin degree of freedom. The *supermatrix* formalism used to analyse the data in our case and described elsewhere[93] has the advantage of being generally applicable to any geometry, being independent of the coordinate system used. This treatment also provides a rigorous formalism that can be applied to layered systems of arbitrary complexity. The code used, written by A. Rhuem,

can be downloaded from the MPI-MF web page at the address http://www.mf.mpg.de We will just introduce the Hamiltonian of the system and the main equation used to describe the interaction neutron-sample. For a detailed description of the formalism see related literature[94].

The total Hamiltonian describing neutron reflectivity from a layered system can be written as sum of the Hamiltonians in each layer:

$$H = \sum_j H_j = V_j(z) - \vec{\mu} \cdot \vec{B}_j \tag{3.16}$$

where $V_j(z)$ is the nuclear potential and $\vec{B}_j$ is the magnetic induction within the j^{th} layer and $\vec{\mu}$ the moment of the neutrons. For measurements in the small angle regime, we can approximate $V_j(z)$ and $\vec{B}_j(z)$ with constant quantities within each layer. In case of strong inhomogeneity in the magnetisation of the layers, one can model dividing each layer j, in sub-layers i, each with uniform magnetisation $m_{i,j}$. in such a way is $\vec{B}_j(z) = \sum_i B_{i,j}(z)$. Writing the moment of the neutrons as an operator, in terms of the Pauli matrix $\vec{s}$, the reflectance will be expressed as function of thickness of the j^{th} layer, the momentum transfer and the scalar product $\vec{s} \cdot \vec{B}_j$.

3.3 Kinematic x-ray diffraction theory (Q>> 0)

X-ray diffraction or Bragg scattering, is a process of elastic coherent scattering of x-rays from the electrons present in a material. Due to the fact that no dynamical process (as multiple scattering, absorption or resonance) is involved, the kinematic approach is enough to describe the mechanism of diffraction from a crystal. Also, although we will always refer to x-ray diffraction, being the only diffraction techniques used in this thesis, all the formalism developed will apply to neutron scattering as well.

Ideally, the incident radiation can be thought as a plane wave characterised by a certain wave-vector k whose magnitude is related to the wavelength λ by the following formula:

$$k = \frac{2\pi}{\lambda}$$

The diffracted radiation is the coherent sum of the radiation elastically scattered by all the electrons invested by the x-ray wave. Due to the periodicity of the crystal the calculation of the scattering from the electrons in the lattice is quite easy. The amplitude of the radiation scattered by a generic atom n in the position $\vec{r}_n$ with respect to a chosen coordinate system has the form

$$A_n(Q) = A_0 f_n e^{2\pi i \vec{Q}\cdot\vec{r}_n} \tag{3.17}$$

where $\vec{Q}$ is the momentum transfer defined above, and $f_n = f_{n,0} + f_n^{'} + f_n^{''}$ is the atomic form factor defined as the amplitude of the wave scattered by the electronic cloud of each atom. The atomic form factor depends on the energy of the radiation used but, far from absorption energies or resonances it can be approximated with a negligible error, by its constant part $f_{n,0}$. One can write the generic atomic position $\vec{r}_n$ as follows:

$$\vec{r}_n = \vec{d}_n + m_a\vec{a} + m_b\vec{b} + m_c\vec{c} \tag{3.18}$$

$$\vec{r}_n = \vec{d}_n + \vec{R}_m \tag{3.19}$$

where $\vec{d}_n$ is the fractional position of the atom in the generic unit cell, and $\vec{R}_m = m_a\vec{a} + m_b\vec{b} + m_c\vec{c}$ indicates the position of the m^{th} cell in a crystal made by $N_a \times N_b \times N_c$ unit cells. Substituting the expression (3.3) for $\vec{r}_n$ in the equation (3.17) and summing over all the n's one obtains:

$$A(Q) = A_0 \sum_n f_n e^{2\pi i\vec{Q}\cdot\vec{d}_n} \sum_{m_a}^{N_a} e^{2\pi i\vec{Q}\cdot m_a\vec{a}} \sum_{m_b}^{N_b} e^{2\pi i\vec{Q}\cdot m_b\vec{b}} \sum_{m_c}^{N_c} e^{2\pi i\vec{Q}\cdot m_c\vec{c}} \tag{3.20}$$

The structure factor F is a quantity depending on the atoms in the u.c. and their position, and is expressed by the following equation:

$$F = \sum_n f_n e^{2\pi i \vec{Q}\cdot\vec{d}_n} \tag{3.21}$$

The sums over m_j (with $j = a, b, c$) can be written as follows:

$$\sum_{m_j}^{N_j} e^{2\pi i \vec{Q}\cdot m_j\vec{j}} = \frac{e^{2\pi i \vec{Q}\cdot N_j\vec{j}} - 1}{e^{2\pi i \vec{Q}\cdot\vec{j}} - 1} \tag{3.22}$$

Finally, the diffracted intensity, given by the square of the amplitude $A(Q)$, can be expressed as a product of a part depending on the unit cell, i.e. the structure factor F, and a part depending on the number of unit cell forming the crystal:

$$I = A(Q)\cdot A^*(Q) =$$

$$= F(Q)F^*(Q) \prod_{j=a,b,c} \left(\frac{e^{2\pi i \vec{Q}\cdot N_j\vec{j}} - 1}{e^{2\pi i \vec{Q}\cdot\vec{j}} - 1}\right)\left(\frac{e^{-2\pi i \vec{Q}\cdot N_j\vec{j}} - 1}{e^{-2\pi i \vec{Q}\cdot\vec{j}} - 1}\right)$$

$$I = F(Q)F^*(Q) \prod_{j=a,b,c} \frac{\sin^2 \pi N_j \vec{Q}\cdot\vec{j}}{\sin^2 \pi \vec{Q}\cdot\vec{j}} \tag{3.23}$$

From equation (3.23) it is clear that the intensity is not vanishing only for $(\vec{Q}\cdot\vec{j}) \in N$ i.e. the following three equalities, called *Laue equations* have to be simultaneously satisfied:

$$\vec{Q}\cdot\vec{a} = h$$

$$\vec{Q}\cdot\vec{b} = k$$

$$\vec{Q}\cdot\vec{c} = l$$

The integers h, k, and l are called Miller indices, and indicate a vector in the reciprocal space (i.e. a crystallographic

direction) for which the diffraction condition is satisfied, provided that the structure factor does not vanish in that point. The ensemble of points which satisfy the Laue conditions are called Bragg points[95], they are indicated with capital letters $[H, K, L]$, to distinguish them from crystallographic planes, indicated with (h, k, l), or from crystallographic direction indicated with $< h, k, l >$.

3.3.1 The structure factor

The structure factor F is a very important quantity in diffraction, because it determines the scattering amplitude of a crystal on the basis of the configuration of the atoms, i.e. the *lattice symmetry*. Waves scattered by equal atoms in a crystal can have constructive or destructive interference depending on their relative position inside the lattice itself. The *selection rules*, i.e. mathematical relationships among the Miller indices, determine the crystallographic direction where the interference is destructive, which are commonly referred to as *forbidden* reflections. The different arrangement of atoms in a crystal lattice defines the *space groups*, or groups of symmetry, for which, independently on the chemical composition of the crystal, the selection rules are the same. The knowledge of the selection rules is of fundamental importance in the determination of the crystal symmetry in a diffraction experiment. For orthorhombic systems of the space group Pbnm the following selection rules hold:

Miller indices	selection rule
0 k l	k + l = 2n
h k 0	h = 2n
h 0 0	h = 2n
0 k 0	k = 2n
0 0 l	l = 2n
h k l	h+l, k = 2n

As an example and useful exercise, we write in the following the analytical form of the structure factor of LCMO compound, which we will use in the calculation of the diffracted intensity:

$$F = (1-x)f_{La}e^{2\pi i\vec{Q}\cdot\vec{d}_{La}} + xf_{Ca}e^{2\pi i\vec{Q}\cdot\vec{d}_{Ca}}$$

$$+f_{Mn}e^{2\pi i\vec{Q}\cdot\vec{d}_{Mn}} + f_{O_{1,2}}e^{2\pi i\vec{Q}\cdot\vec{d}_{O_{1,2}}} \tag{3.24}$$

The space group of LCMO in a wide range of doping is Pbnm. The structure factor in equation 3.24 is calculated on the basis of the atomic position taken from reference [64], which are listed in the table 3.3.1[1].

	LCMO film			LCMO bulk		
Atom	x	y	z	x	y	z
La, Ca	0.017	1/4	0.989	0.020	1/4	0.996
Mn	1/2	0	0	1/2	0	0
O(1)	0.483	1/4	0.073	0.491	1/4	0.064
O(2)	0.277	0.031	0.728	0.276	0.033	0.724

Table 3.1: Atomic positions of LCMO bulk compound and the strained films are shown. From reference [64]

[1]Note that in the paper of Zandbergen the space group used is Pnma. For our calculation in Pbnm space group, appropriate positions have been taken into account

The atomic positions of the elements in the unit cell, accordingly with the Pbnm space group are the following:

$$La, Ca = \{x, y, 1/4\}, \{x + 1/2, 1/2 - y, 3/4\}$$
$$\{-x, -y, 3/4\}, \{1/2 - x, y + 1/2, 1/4\}$$

$$Mn = \{0, 1/2, 0\}, \{1/2, 0, 1/2\}, \{1/2, 0, 0\}, \{0, 1/2, 1/2\}$$

$$O_2 = \{\{x, y, z\}, \{x + 1/2, 1/2 - y, -z\}$$
$$\{-x, -y, z + 1/2\}, \{-x + 1/2, y + 1/2, -z + 1/2\}$$
$$\{-x, -y, -z\}, \{-x + 1/2, 1/2 + y, z\}$$
$$\{x, y, -z + 1/2\}, \{x + 1/2, 1/2 - y, z + 1/2\}$$

$$O_1 = \{x, y, 1/4\}, \{x + 1/2, 1/2 - y, 3/4\}$$
$$\{-x, -y, 3/4\}, \{1/2 - x, y + 1/2, 1/4\}$$

3.4 3-D reciprocal lattice and crystal truncation rods ($\mathbf{Q}_{//}$ and $\mathbf{Q}_{\perp} \neq 0$)

The ensemble of the allowed Bragg reflections $[H\,K\,L]$ for a given crystal lattice forms the reciprocal lattice. For a 3-dimensional crystal the reciprocal lattice is made of points, while for a 2-dimensional crystal, e.g. an atomic plane, the reciprocal lattice is made of streaks, or rods perpendicular to that plane (see figure 3.5). These lines of intensity in the reciprocal space, are called crystal truncation rods (CTR)[96]. Due to their particular shape, i.e. being a continuous intensity distribution along one reciprocal lattice direction (in this case l) the CTRs are generally indicated using only two Miller indices of the crystallographic plane they refer to (in our case h and k). Finally a

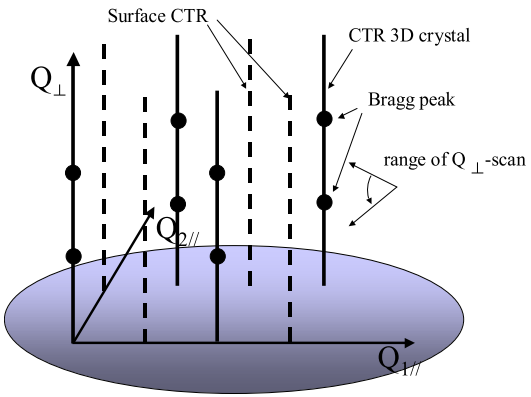

Figure 3.5: Surface of a crystal and CTRs

CRT of a crystal with the surface defined by the crystallographic axis a and b is indicated as $[H, K]$ rod.

It is easy to understand as a surface, as a 2-dimensional arrangement of atoms, also determines the presence of rods of intensity in the reciprocal space. The presence of a surface in real crystals makes the presence of CTRs, in a diffraction experiment, unavoidable. Moreover, in this case the intensity along the CTRs is not uniform (as in the ideal case) but depends on the nature of the surface itself. One can distinguish between two main cases depending if the surface has the same or a different structure than the bulk (due for example to oxidation or reconstruction[97]). In the first case the intensity along the surface normal is given by the sum of the intensity of the Bragg points (coming from the $3D$ crystal) *and* the intensity of the rods (coming from the surface), as shown in figure 3.5. In this case the intensity shows a peak in the position of the Bragg point and a minimum in between two Bragg points. In the second case two sets of CTRs appear. One related to the $3D$

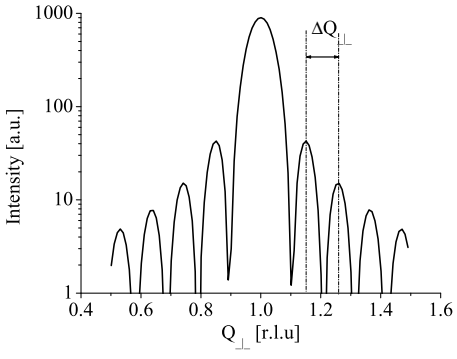

Figure 3.6: Intensity of a CTR of a film with thickness T near a Bragg peak: Laue oscillations. The distance between two maxima (or minima) is related to the thickness of the crystal $\Delta Q_\perp = 2\pi/T_{cry}$.

crystal with its (ideal) surface, i.e. identical to the first case, the other related to a *single layer* on the top of the first surface. The position of this second set of CTRs depends *only* on the structure of the surface, and the intensity modulation is related to the arrangement of the atoms *on the surface* but not into the bulk. A scheme of these rods is given in figure 3.1, page 63, where they are drawn as lines without Bragg peaks intersecting them. Finally, the study of such rods gives important information on the surface as well as interfaces e.g. roughness, termination layer, reconstruction.

The intensity along the CTRs is of particular interest also in the case of thin films. The diffracted intensity of a crystalline film with thickness T_{film} has a special distribution in the reciprocal space. Due to the finite extension of the crystal in one dimension, and the presence of two "surfaces" (substrate-films and film-vacuum interfaces) the intensity of the scattered radiation along a CTR has the typical aspect of the Kiessig fringes

(cf page 67). This comes directly from the Laue equation (3.23). The intensity profile will show a succession of maxima and minima, separated by a distance which is inversely proportional to the thickness of the crystalline part of film T_{cry}. The equation is the same as the (3.2) on page 67, with the quantity T_{cry} instead of T_{film}. Note that it is generally $T_{cry} \leq T_{film}$, i.e. the thickness which scatter coherently is less or equal to the total thickness of the film. These features are called Laue oscillations. They give a measure of the thickness which scatters coherently in a crystal (cf figure 3.6).

Any modulation or asymmetry in the intensity distribution along the rods can be connected to a form of "disorder" in the crystal distributed in the planes perpendicular to the rods (cf reference [99]). In the case of strained film, the phenomenon of relaxation of strain along the direction of growth, i.e. a variation of the spacing of the layers along the surface normal, is one of the possible sources of non-homogeneity.[2] In presence of a mismatch between the substrate and the film, the first atomic layers can undergo an elastic deformation of the in-plane atomic spacing, which relaxes with increasing thickness. We will show in the next chapter the model of strain relaxation in more detail.

The intensity of a CTR for a crystal with a surface is calculated from the Laue equation in the limit of large N_z (i.e. the number of unit cells in the direction perpendicular to the surface). In this case the numerator of the function in equation 3.22, which can also be written in the form

$$\sum_{m_z}^{N_z} e^{2\pi i \vec{Q} \cdot m_z \vec{z}} = \frac{\sin^2 \left(N_z \vec{Q} \cdot \vec{a}_z / 2 \right)}{\sin^2 \left(\vec{Q} \cdot \vec{a}_z / 2 \right)}$$

can be approximated by its average value 1/2. This gives a

[2]There can be many cases of non-homogeneity along the direction of the growth (perpendicular to the plane of growth), as for example the phenomenon of confinement of certain atomic species in thin films of alloys[100], or adsorption of atoms from a surface with a certain penetration depth in the bulk.

simple expression for the intensity of the diffracted radiation along the CTR which is proportional to the quantity

$$1/(2sin^2(\vec{Q} \cdot \vec{a}_z/2)$$

It is important to notice that this expression does not apply to the case of a monolayer, where only one atomic layer and not the whole crystal, contributes to the rod intensity.

As we pointed out before, the CTR are also sensitive to the termination layer of a crystal. In such case the intensity should be calculated from both the bulk contribution and the surface monolayer. In the case of a crystal with a complex u.c. made of several different atomic layers, there might be (depending also on energy considerations) several possibilities for surface termination. Each termination gives a special contribution to the CTR intensity, that allows the termination layer to be deduced from the CTRs data as shown in the work by You et *al.*[101]. In such case the intensity will contain an interference term between the bulk structure factor F_B and the structure factor of each atomic layer F_i, which will modify the intensity distribution on the basis of the following equation:

$$I_{CTR} = I_0(Q)N_xN_y\Big[F_B(Q)\frac{1}{1-e^{iQ_zc}} + \sum_i F_i\Big]^2 \qquad (3.25)$$

3.5 Grazing incidence diffraction ($\mathbf{Q}_{//} \neq 0$ and $\mathbf{Q}_{\perp} = 0$)

Grazing incidence diffraction (GID) is a technique which allows one to measure the purely in-plane components of the **Q**-vector. It makes possible to access the Bragg reflections relative to crystallographic planes with vector lying on the surface of the sample measured. On the other hand, GID technique is widely used to measure the CTR intensity coming from the near-surface layers, due to the possibility of tuning the penetration depth of the x-rays to probe few atomic layers close to the surface.

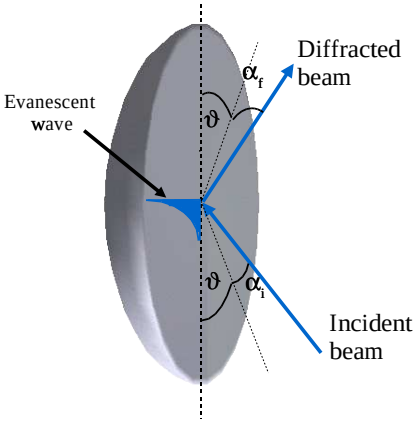

Figure 3.7: GID geometry, the evanescent wave is highlighted.

We now describe the GID technique to give a better idea of its capabilities. The x-ray wave with wave-vector $\vec{k}_i$ impinges on the surface with a glancing angle α_i, the exit angle being α_f. The Bragg angle lies in the plane of the surface (see figure 3.7). Also for the GID a great role is covered by the refractive index, n given by the equation 3.4. For x-rays frequencies the value of n is about $(1-10^{-5})$ and it is in general a complex quantity which accounts both for the change in the propagation vector of the radiation and the absorption of radiation from the material. In GID configuration, the momentum transfer has a component Q_z along the surface normal, and a component Q_{xy} parallel to the surface plane. In the extreme case of α_i smaller than the critical angle α_c, which is the angle for total external reflection, the component of $\vec{k}_i$ perpendicular to the plane becomes a complex quantity inside the material, as discussed in section 3.2, which is purely imaginary in case of absence of absorption i.e. $\beta = 0$. Consequently also the component of the momentum transfer

along the surface normal Q_z becomes zero, and the x-rays wave in the material, the *evanescent* wave described by the equation 3.11 (page 67) travels parallel to the surface.

The imaginary part of the vector $\vec{k}_i$ gives the measure of the penetration depth Λ_i of the evanescent wave inside the material following the formula (3.26). For the time-reversal symmetry, also the vector $\vec{k}_f$ of the exit wave is associated to a probed depth, Λ_f, given by the same formula:

$$\Lambda_i = \frac{1}{Im[k_i z]} \tag{3.26}$$

Since the momentum transfer **Q** is related to the incident and exit vector from the formula $\vec{Q} = \vec{k}_f - \vec{k}_i$, it is also a complex quantity associated to a scattering depth Λ given by:

$$\Lambda = \frac{\Lambda_i + \Lambda_f}{\Lambda_i \Lambda_f}$$

The possibility of tuning and controlling carefully the scattering depth makes GID a depth-sensitive technique. The range of scattering depth varies between 50Å and 1000Å depending on the material. In this work, however, the GID technique has been mainly used to access the purely in-plane component, to measure structural modulation propagating in the direction parallel to the surface of the films studied. All the measurements have been carried out at an incident angle α_i equal to the critical angle α_f to get the maximum intensity of the scattered radiation, as well as to get a scattering depth enough to measure the signal from the substrate, and to compare the in-plane lattice spacing of the two materials.

3.6 Experimental details

3.6.1 Beam lines used for XRD experiments

The XRD experiments have been performed using synchrotron radiation. The reason for this is that the strain-induced effect on the structural properties of thin films, such as distortions, or structural modulations, are expected to be small, and give rise to diffraction signals quite small compared with the Bragg scattering from the crystal structure. The limited intensity available from conventional sources is a strong limitation for the detection of such signals, and the use of synchrotron is required. Synchrotron sources provide a bright beam with a narrow spot size and a dynamical range up to 12 orders of magnitude. The experiments relevant for this thesis have been performed at the beam lines BM28 (XMaS) of the ESRF in Grenoble, and the MPI-MF surface diffraction beam line at ANKA, Karlsrhue.

The XMaS beam line is optimised for single crystal diffraction over an energy range of 3 to 15 keV. It is sited on a Bending Magnet source (critical energy 9.8 keV). The optics consists of a double-crystal monochromator followed by a toroidal mirror. The monochromator comprises two plane silicon crystals, currently silicon $< 111 >$ mounted in a crystal cage which maintains a constant 20mm offset for the exit beam. The first crystal is water cooled and absorbs most of the incident synchrotron radiation power. The mirror is uncooled, is made from single crystal silicon and has a sectored cylindrical cross-section of 116 mm radius (saggital). The small cylindrical curvature required tangentially, 5.5 km, is produced by a pneumatically actuated bending mechanism. The two curvatures thus form the toroidal surface that focuses the beam to a small spot onto the sample surface. To enhance the mirror reflectivity the surface has been coated with a thin layer of Rhodium. The maximum flux collected is from a fan of radiation of 3.1 milliradians horizontal width and 0.2 milliradians vertical height. The intensity measured at the sample position at an energy of $10KeV$ is $\approx 10^{12}$

Figure 3.8: Photo of the BM28 diffractometer

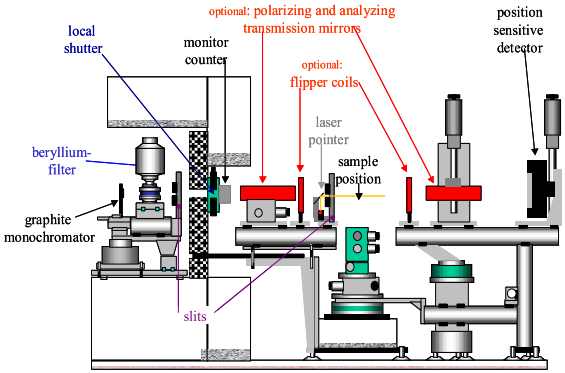

Figure 3.9: schematic of the eva reflectometer

photons per second. The experimental hutch is equipped with a 11 axis Huber diffractometer, shown in figure 3.8. More information about the beam line can be found at the XMaS web-page: http://www.esrf.fr/exp_facilities/BM28/xmas.html.

To perform XRD experiment in GID geometry the sample has been mounted with the surface parallel to the electron orbit in the synchrotron ring. The horizontal ω circle has been used as grazing incidence angle α_i, and the horizontal detector arm to determine the exit angle α_f. In this configuration the scattering plane is in the direction vertical to the electron orbit, in such a way the polarisation of the beam (in the horizontal plane) does not influence the measured intensity. The energy of the photons used for the experiment is $10KeV$, corresponding to a wavelength of 1.293Å.

3.6.2 EVA beam line at ILL

PNR experiments have been performed at EVA Beamline, at ILL in Grenoble. Eva is a 3-axis reflectometer supplied with

cold neutrons with wavelengths 5.5Å or 2.75Å, which can be used both in reflection and grazing incidence geometry. The sample can be mounted in a displex (a closed cycle refrigerator), for controlled temperature measurements in a range of 10–300 Kelvin. An electromagnet at the sample position can supply an external magnetic field up to 0.45Tesla. The beam is polarised and analysed with magnetised supermirrors[90], and detected by a position sensitive detector PSD which can be put at a variable distance from the sample to provide a better resolution or reduce the absorption of the scattered beam by the air. A schematic of the beam line EVA is shown in figure 3.9

For our experiment the sample has been mounted in the displex and the magnet has been used to apply an external field. PNR profiles have been measured at very low temperature ($T = 10K$) and at a value of the external magnetic field $H_{ext} = 0.2Tesla$ to be sure to have the maximum alignment of the magnetic moment. Polarisation analysis has also been used. The results are discussed in chapter 3.4.

Chapter 4

Thin films of LCMO: growth, transport and magnetic measurements

In this chapter we will describe the transport and magnetic measurements performed on films of LCMO with thickness in the range 50–600Å and discuss the results. The transport measurements are the subject of another PhD thesis[102]. Their results are relevant to the work described in this PhD thesis, and will be discussed in this context. We will especially emphasise the different transport behaviour along different crystallographic planes, i.e. the anisotropy of the transport properties.

The magnetic characterisation of the samples, on the other hand, is part of this PhD work. SQUID measurements have been carried out on samples of different thickness, and will be shown and discussed in this chapter. As will be discussed in the following chapter, the magnetic properties of the samples studied show a marked thickness dependence, which also corroborates the PNR results discussed in chapter 3.4 and are also consistent with the interpretation of the structural measurements, discussed in chapter 6.

Before introducing the transport properties, we will briefly discuss the quality of the samples, including their growth parameters and preliminary structural measurements.

4.1 LCMO thin films: morphology and crystalline quality

The films of LCMO have been fabricated via pulsed laser ablation (PLA)[1]. The PLD system consists of a UHV chamber equipped with an *in-situ* atomic force microscope (AFM) which provides a check of the sample morphology before and after the growth. A RHEED system is also incorporated (see figure 2.1, page 49) to control the crystal quality of the surface during growth (see section 2.1.2).

The films are deposited on $< 100 >$ oriented STO substrates. Before the deposition, the substrate is prepared with an etching procedure aimed to create a Ti-O termination layer of the surface to improve the epitaxial growth of the LCMO films. AFM measurements performed on the STO reveal that the surface is flat on atomic scale, with step height of one u.c. and with terraces a few thousands Å wide.

The control of growth conditions, such as substrate temperature, deposition rate, oxygen partial pressure and a final annealing at a temperature higher than the deposition temperature, guarantee an ordered growth of the films with a high crystalline quality. The presence of RHEED oscillations during the entire deposition process indicates a *layer-by-layer* growth of the film (section 2.1.2). Also, AFM images of the sample recorded shortly after the growth indicate a surface morphology very similar to the surface of the substrate, as shown in figure 4.1. This demonstrates that the steps of the substrate propagate through the entire thickness of the film. Moreover, these data

[1] from J. Klein[102] at the University of Cologne - Germany

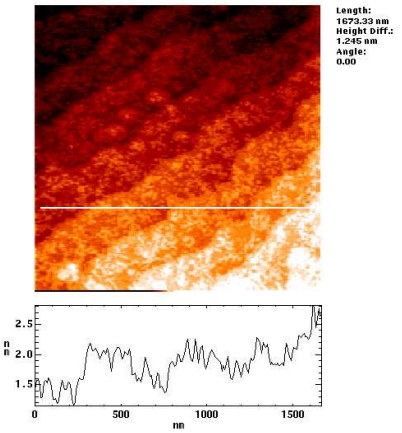

Figure 4.1: AFM image of 600Å LCMO film. The step structure of the STO surface looks the same, it is preserved at the LCMO surface. Courtesy of J. Klein

give strong evidence for an ordered phase, free from dislocation defects that would break the coherence of the crystal lattice.

The epitaxial growth and the good crystal quality of the films are confirmed by x-ray diffraction. Figures 4.2 and 4.3 show the results of the preliminary x-ray measurements. The FWHM of the $[002]_c$ Bragg peak of a 600Å thick film of LCMO is found to be $\approx 0.037^o$, similar to that of the STO substrate. Moreover, the Laue oscillations along the CTRs indicate coherent scattering from the entire film thickness (cf section 3.4).

4.2 Transport properties

Here we highlight the results of the transport property measurements of these films, and shortly describe the setup used for the

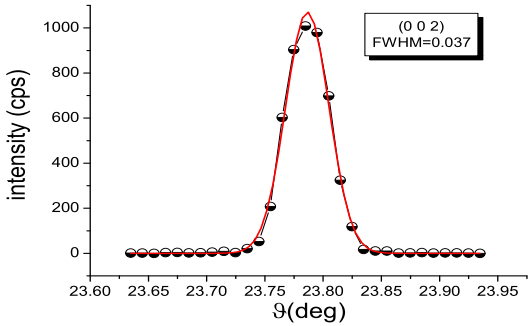

Figure 4.2: FWHM of [002] peak of 600Å thick films of LCMO on STO

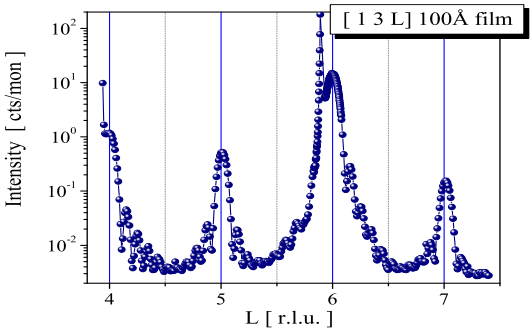

Figure 4.3: Laue Oscillations along the CRT [13] of a 100Å thick film.

measurements. The reader is referred to J. Klein's PhD thesis

for further details.

4.2.1 Geometrical configuration for the *in-plane* and *out-of-plane* measurements of the R(T)

The transport measurements have been performed on these samples in two different geometries, *in-plane* geometry (standard configuration) and *out-of-plane* geometry. For the *in-plane* geometry measurements four gold contacts have been evaporated on the surface of the samples, two for supplying the current (I) and two for the measurement of the potential difference (V). For the *out-of-plane* measurements *mesa* structures (see figure 4.4) were created, to allow the current to flow along the c-axis of the films.

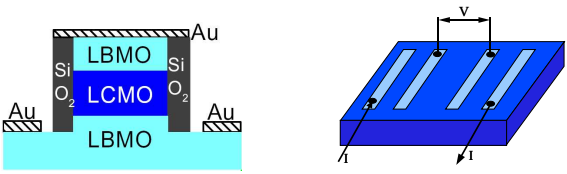

Figure 4.4: Sketch of the setup used for the in-plane and the out-of-plane R(T) measurements

The mesa structure used to measure the c-axis resistivity of our films is shown in figure 4.4. The LCMO film has been grown in a trilayer structure in between two $La_{2/3}Ba_{1/3}MnO_3$ (LBMO) layers, which play the role of electrodes. A measurement of the transport without the two LBMO layers would have revealed the tunneling process between the gold contacts through the LCMO insulating barrier rather than the intrinsic properties of the layer itself. This is because very thin films of

LCMO have been found to be insulating in the whole range of temperatures (5–300K)[102, 71]. The compound LBMO is suitable because it is a CMR material with physical properties very similar to LCMO whose T_C ($\approx 300K$ in the bulk) is only slightly suppressed in films with the thickness used[71]. Moreover the similarity in the crystal structure and lattice parameters between the two compounds ($\delta_{LCMO-LBMO} \approx 0.01\%$) allows the epitaxial growth of one layer on the other in the trilayer structure, avoiding the introduction of further parameters such as roughness, disorder, stacking faults, that would influence the out-of-plane transport properties of the compound of interest (LCMO).

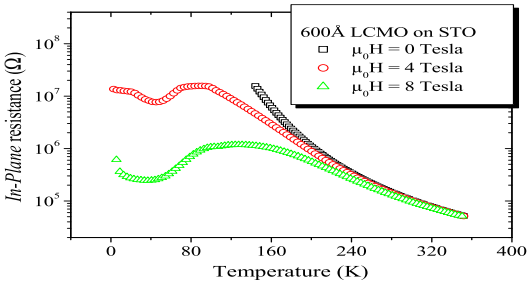

Figure 4.5: *In-plane* R(T) of 600Å LCMO films deposited on STO. $T_{MI} \approx 130K$

4.2.2 Anisotropy in transport for LCMO films

The resistivity measurements give very interesting results, different for the *in-plane* and the *out-of-plane* geometries. The *in-plane* measurements performed on a 600Å thick film show that a metal-insulator (M-I) transition occurs at a temperature $T_{MI} \approx 130K$ (see figure 4.5). The M-I transition follows the PM-FM transition at a temperature comparable with T_C de-

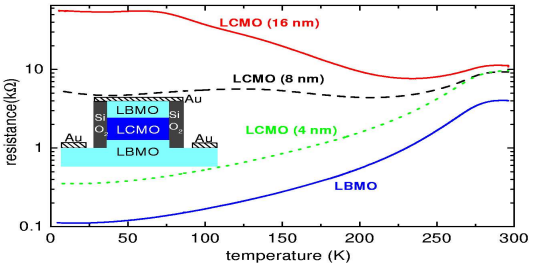

Figure 4.6: *Out-of-plane* R(T) of LBMO-LCMO-LBMO trilayer for different thickness of LCMO[71]. The mesa structure is also sketched.

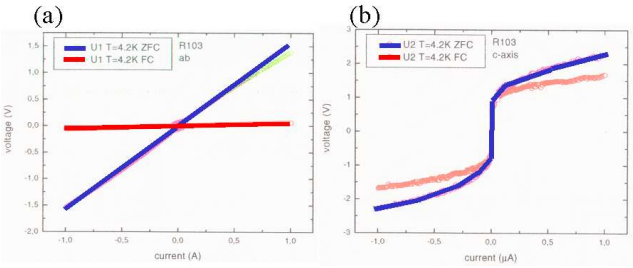

Figure 4.7: I-V characteristics for both in-plane (a) and out of plane (b) configurations. The non-ohmic behaviour of the I-V curve measured out-of-plane gives a clear evidence of an insulating state developing along the c-axis direction.

termined by SQUID measurements (see Section 4.3). Also the CMR effect is present, with a value of the MR ratio of about 100%. On the other hand, films with thickness < 200Å have been found to be insulating for all temperatures, even in the FM phase, which are normally metallic in the bulk.

Resistivity measurement along the *out-of-plane* direction provide evidence for an insulating behaviour for films of all thickness. As can be seen in figure 4.6 the high temperature part is dominated by the LBMO, while for $T < 200K$ the contribution of LCMO becomes prevalent. The insulating behaviour of the LCMO layer is also confirmed by the I-V characteristics measured in both in-plane and out-of-plane directions, with an in-plane ohmic behaviour and non-ohmic behaviour along the c-axis of the sample (figure 4.7).

4.3 SQUID magnetometer

A superconducting quantum interference device (SQUID) is a mechanism used to measure extremely weak magnetic signals, using a device called Josephson junction. A Josephson junction is made up of two superconductors, separated by a non superconducting layer so thin that electrons can tunnel through the insulating barrier[103]. A SQUID consists of tiny loops of superconductors employing Josephson junctions. A radio frequency (RF) SQUID is made up of one Josephson junction, which is mounted on a superconducting ring. An oscillating current is applied to an external circuit, whose voltage changes as an effect of the interaction between it and the ring. The magnetic flux is then measured. A direct current (DC) SQUID, which is much more sensitive, consists of two Josephson junctions employed in parallel so that electrons tunneling through the junctions undergo quantum interference, depending on the strength of the magnetic field within a loop. DC SQUIDs sense a resistance in response to even tiny variations in a magnetic field, and it is this capacity that enables the detection of minute magnetic fields.

In this work the SQUID has been used to measure the magnetization $\vec{m}$ of the films as response to an external magnetic field H_{ext} in a wide range of temperatures and fields. The field H_{ext} is applied along the film surface in direction parallel to the $< 110 >$ crystallographic direction. It is worthy to note

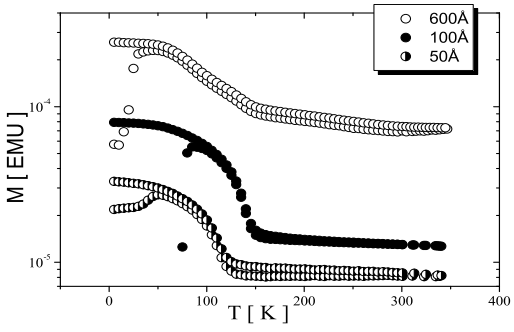

Figure 4.8: M(T) curves for 600Å, 100Å and 50Å thin films of LCMO on $SrTiO_3$ substrate.

that the SQUID is a volume-sensitive technique, and does not allow the detection of inhomogeneities inside the sample. As a consequence, the only measurable quantity is the *average* magnetization $< \vec{m} >$.

4.3.1 Magnetisation measurements on LCMO thin films

Measurements of magnetisation vs. temperature M(T) have been carried out both in zero field cooling (ZFC) and field cooling (FC) process, in a constant external field $H_{ext} \approx 100Oe$ and in a temperature range of [5–300]K. From these curves the Curie temperature T_C of the samples has been deduced. Moreover, from hysteresis curves M(H), measured at $T < T_C$, the value of coercive field and the value of $< \vec{m} >$ have been measured. These results are summarised in table 4.1.

The results of the SQUID measurements performed on three LCMO thin films with different thickness are shown in figure 4.8

Sample	Thickness	T_C	H_{co}	$< \vec{m} >$
Bulk		$\approx 280K$	$\approx 80Oe$	$3.7\mu_B$
R128	50Å	108K	295Oe	$1.2\mu_B$
R127	100Å	135K	227Oe	$0.9\mu_B$
R96	600Å	134K	628Oe	$0.5\mu_B$

Table 4.1: Table which summarises the results of the SQUID measurements performed on LCMO thin films of different thickness deposited on STO. The bulk value are reported for comparison

and 4.9. As we can see from the M(T) curves (figure 4.8), the T_C for all the films lies in the range of temperature $[80 \div 135]K$ and does not show a clear thickness dependence, i.e. there is no sign of relaxation towards the bulk value ($T_C \approx 280K$). On the other hand, a comparison between the M(H) measurements performed on the same films (shown in figure 4.9) indicates a remarkable change of the magnetic properties with the thickness.

The value of the coercive field, H_{co}, is larger than the value expected from the bulk $H_{co} \approx 80Oe$. Moreover, it is not the same for all the samples, and *increases* with the thickness of the films, as summarised in table 4.1. On the other hand, the value of the average magnetisation $< \vec{m} >$ per $Mn-$atom, is strongly reduced in comparison with the value of $3.7\mu_B$ expected from the bulk. It reaches a value as low as $1.2\mu_B$ for the thinner film, and further *decreases* with increasing thickness. This behaviour is strange, to say the least. Contrary to what it is generally found for thin films[2], where a relaxation is always found toward bulk value with increasing thickness, in our case there is no sign of relaxation effect. The strain-induced properties (reduction of T_C and $< \vec{m} >$, and increase of H_{co}) persist for all the thickness investigated, and seem to be amplified with increasing

[2]See also chapter2 of this thesis, page 55

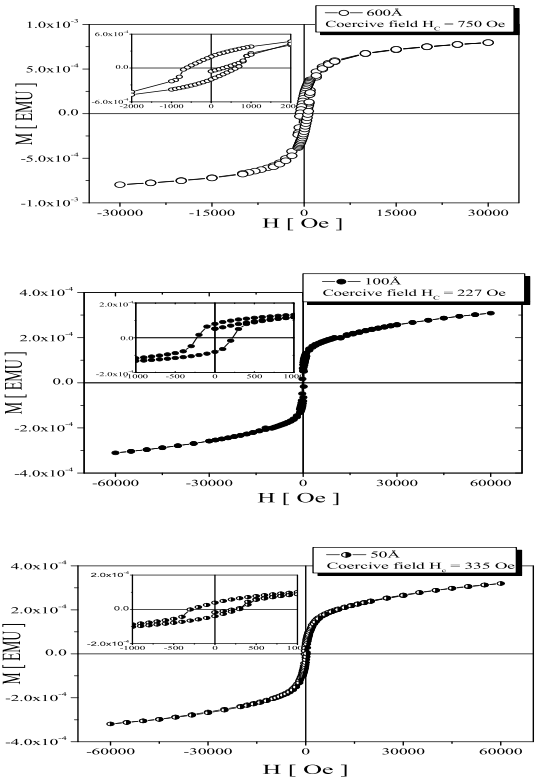

Figure 4.9: M(H) curves for 600Å, 100Å and 50Å thin films of LCMO on $SrTiO_3$ substrate. The data are corrected for the paramagnetic contribution of the substrate

thickness. These results suggest the presence of a *gradient* in the magnetisation profile of the films, with $< m >$ decreasing from the substrate-film interface to the surface of the sample. This hypothesis has been successfully applied to the interpretation of the PNR measurements, as will be discussed in chapter 3.4.

Before summarising, another important remark has to be made. As it can be seen from the shape of the hysteresis curves in figure 4.9, the magnetisation of the samples does not saturate up to the highest field applied, i.e. $H = 6Tesla$. This effect can be ascribed either to a *canting* of the magnetic moments, or to the presence of magnetic domains in high external magnetic field. The last hypothesis, subject of recent publications[72] will be further discussed in the next chapter of this thesis. The "saturation" magnetisation of the samples has been calculated on the basis of the value of their magnetisation at the maximum value of the applied field.

To summarise, these films do not show evidence of a strong "relaxation" behaviour towards the bulk, both from the point of view of structural and transport properties. The T_C is similar for all the thicknesses and also the pseudomorphic relation with the substrate persists, evidencing that the films can be considered "strained" up to the highest thickness investigated (i.e. 600Å). Moreover, the decrease of the average magnetisation, as well as the increase of the coercive field of the films suggests that something more than a simple "relaxation" effect has to be taken into account to explain the anomalous film properties.

Chapter 5

Experimental results and Twin Modulation

In order to understand how strain acts on the structure of the deposited film, and the subsequent effect on the transport properties, a detailed structural analysis is required. X-ray diffraction (XRD) provides a detailed macroscopic tool to investigate the structural properties of the films and their relation with the structural characteristics of the substrate. Furthermore, XRD can be used to probe strain effects via structural distortions which maybe correlated with transport properties. The XRD scattering geometries used (discussed in chapter 3) have been applied to address different characteristics of the films. GID is useful for checking the purely in-plane components of the reciprocal lattice (RL), to analyze the epitaxy of the system, the in-plane mosaicity and crystal structure. The CTRs study gives information on the crystal structure in the direction of the growth and eventual relaxation effects occurring along the surface normal.

In this chapter we will describe the GID experiment performed on the films, and the in-plane modulation found. The model proposed to explain the scattering profiles agrees quite

well with the experimental results.

5.1 More about orthorhombic and pseudo cubic notation

As mentioned before, the space group of bulk LCMO is *Pbnm*. For simplicity of notation, and for an easier comparison with the cubic structure of the STO substrate, sometimes the pseudo-cubic coordinates are more convenient to use. The relation between orthorhombic and pseudo-cubic coordinates are expressed as

$$\begin{gathered} a_o \approx b_o \approx \sqrt{2} a_{pc} \ , \ c_o \approx 2a_{pc} \\ \vec{a}_o = \vec{a}_{pc} - \vec{b}_{pc} \\ \vec{b}_o = \vec{a}_{pc} + \vec{b}_{pc} \\ \vec{c}_o = 2\vec{c}_{pc} \end{gathered}$$

In terms of Miller indices the relation between orthorhombic and pseudo-cubic reciprocal lattice vector is the following:

$$\begin{aligned} h_o &= h_{pc} - k_{pc} \\ k_o &= h_{pc} + k_{pc} \\ l_o &= 2l_{pc} \end{aligned}$$

From now on we will indicate with a subscript *_o*, *_c* and *_pc* respectively for the orthorhombic, cubic and pseudo-cubic quantities (e.g. crystallographic directions, lattice parameters, atomic planes, etc.). Because the film of LCMO grows with the crystallographic direction $< 100 >_o$ along the $< 110 >_c$ of STO, we will frequently use the cubic lattice of the STO as a reference, both in real and reciprocal space.

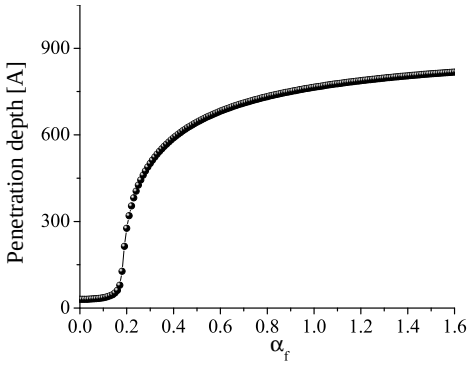

Figure 5.1: Graph of the penetration depth of 10keV x-ray beam in a LCMO sample as a function of the exit angle α_f at fixed incident angle $\alpha_i = \alpha_c$

5.2 Experimental: Grazing Incidence Diffraction for *in-plane* measurements

The GID measurements have been performed at an incident angle $\alpha_i = \alpha_c$, to have the maximum intensity from the film, and a penetration depth large enough to have a signal from the substrate. The scattering signal from the substrate provides information about the epitaxial relationship with the film. At the energy of the x-ray radiation used (E_X=10 keV), the critical angle for the LCMO is $\alpha_c \approx 0.27^o$ and the volume probed is easily calculated from illuminated area and the scattering depth, which is $\Lambda \approx 400$Å for $\alpha_f = \alpha_i$. The GID measurements were performed to investigate $[HK0]$-types Bragg peaks. A sketch of the reciprocal space is shown in figure 5.2

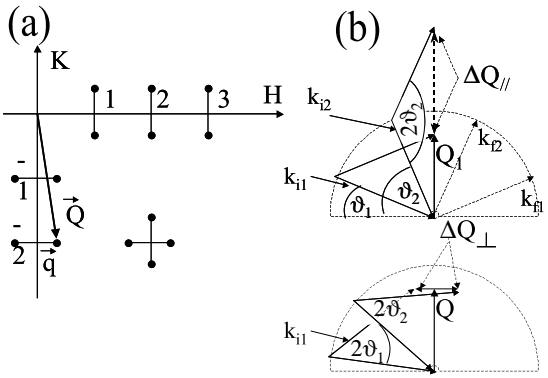

Figure 5.2: (a) Sketch of the reciprocal lattice map. The positions of the SL peaks in the H-K plane are shown. (b) Schematic of longitudinal ($\Delta Q_{//}$) and transverse ($\Delta Q_{\perp}$) scans

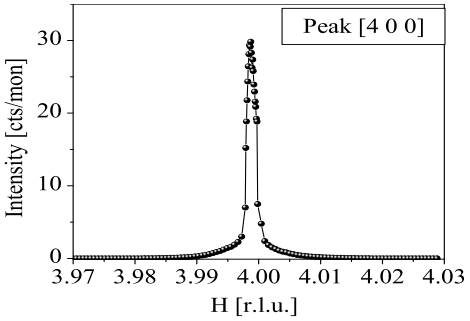

Figure 5.3: Longitudinal scans of [400] Bragg peaks of the 100Å film. No splitting is present

5.2.1 100Å LCMO film

From GID measurements performed on the 100Å thick film, sharp Bragg peaks at the reciprocal lattice position of the STO are observed. No film peaks are found which correspond to the lattice parameter of the bulk LCMO. This indicates perfect match of in-plane lattice parameter i.e. presence of pseudomorphism and epitaxial strain. Moreover, the in-plane Bragg peaks are quite sharp, demonstrating the long coherence of the diffracting planes. Figure 5.3 shows the longitudinal scans[1] across the Bragg [4 0 0] peak. Only one peak is observed in the scan, indicating that no additional periodicity other than the one from the substrate is present. The film is epitaxially grown on the substrate, moreover, the in-plane lattice parameters are identical (pseudomorphism). This is true for all the longitudinal scans of in-plane Bragg peaks of the form $[H\,K\,0]_c$. Furthermore, in

[1] A longitudinal scan records the intensity of the scattered radiation along the direction of the momentum transfer $\vec{Q}$, and gives information about the spacing of the crystallographic planes perpendicular to it (see also figure 5.2)

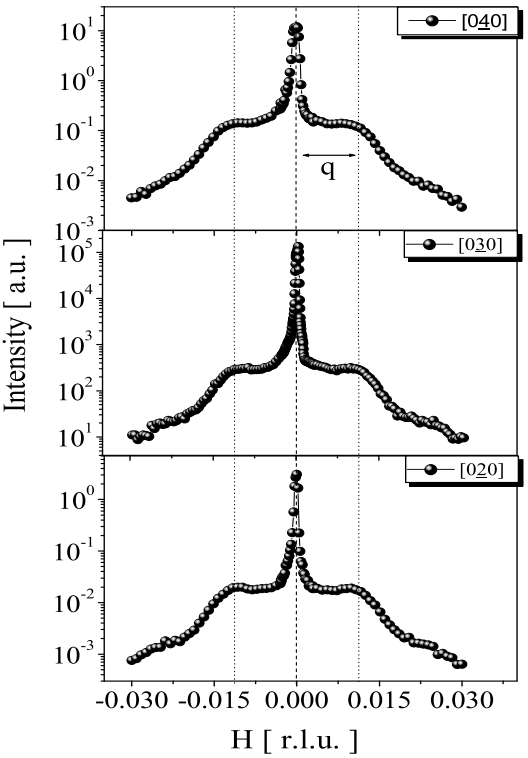

Figure 5.4: In-plane modulation measured on the $[0\bar{2}0]$, $[0\bar{3}0]$ and $[0\bar{4}0]$ Bragg peaks of the 100Å thick film.

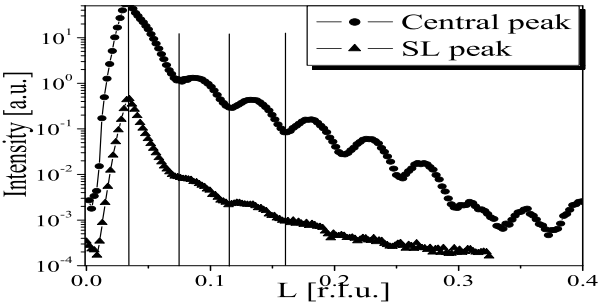

Figure 5.5: L-scans performed on the central (filled circles) and the SL peaks (triangles) of the reflection $[0\,\bar{2}\,0]$ of the 100Å thick film

transverse scans[2] performed on the same peaks, the contribution from the substrate and the film cannot be distinguished (see central peak in figure 5.4). This indicates that the mosaicity of the film is comparable to that of the substrate, sign of very good crystalline quality of the film.

As can be clearly seen from the plot in figure 5.4, these transverse scans show a remarkable feature: together with the sharp central component, representing the Bragg peak of the in-plane lattice spacing of STO-LCMO, two broad side peaks appear at a distance $\pm \mid \vec{q} \mid$ from the center, along the crystallographic direction $< 100 >_c$ with $\mid \vec{q} \mid$ independent of the momentum transfer $\vec{Q}$. Also $[H\,0\,0]$-type reflections show side peaks at the same distance from the central peak, with $\pm \mid \vec{q} \mid$ independent on $\vec{Q}$ *but* directed along the $< 010 >_c$ axis. Furthermore, $[H\,K\,0]$-type Bragg peaks with both H and $K \neq 0$, present 4 satellites at the following positions: $[H \pm q\,K\,0]$, $[H\,K \pm q\,0]$. Finally, satellites are present around every Bragg peak with in-plane component and are completely absent around Bragg peaks of

[2] A transverse scan is shown in figure 5.2

the type $[0\,0\,L]$. A schematic map of the reciprocal space of the film investigated is shown in figure 5.2(a), which summarises the features described.

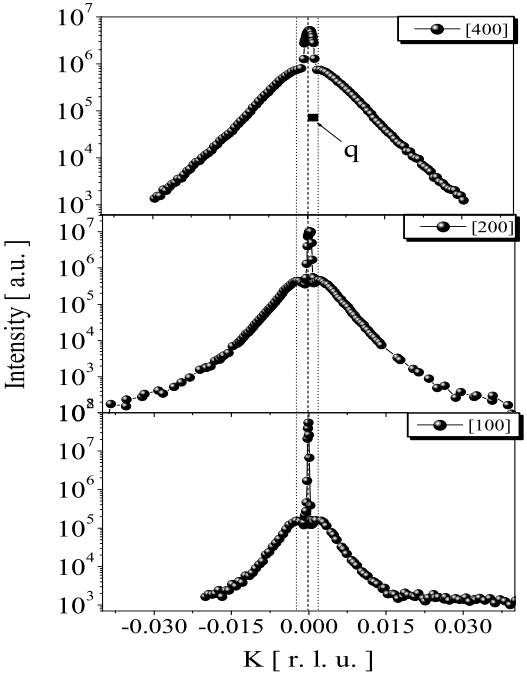

Figure 5.6: Transversal scans of the $[1\,0\,0]_c$, $[2\,0\,0]_c$ and $[4\,0\,0]_c$ peaks of a 400Å film

5.2.2 400Å thick film

Similar results are found for the 400Å film. Satellite peaks are found around in-plane Bragg peaks, with $\vec{Q}$-independent vector

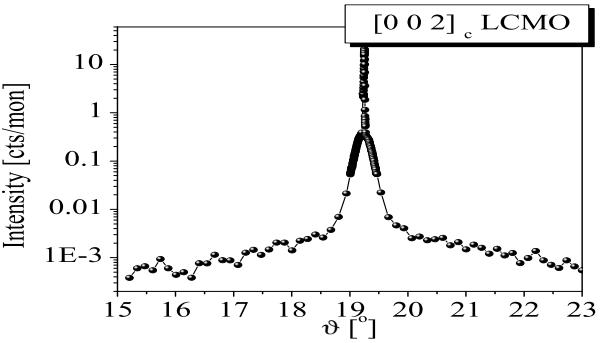

Figure 5.7: Transverse scan of the $[002]_c$ peak of the 400Å film

$\vec{q}$. From figure 5.6, one can see that in this case the absolute value of q is much smaller than the one found for the 100Å film.

As for the case of the 100Å film, no clear satellite peaks have been found around out-of-plane Bragg reflections. However, for $[0\,0\,L]$-type peaks, one can distinguish 3 component, in the transverse scans, as can be seen in figure 5.7 a *broad* component has been detected. The sharp component corresponds to the $[0\,0\,2]_c$ Bragg peak of the LCMO film, as it is shown in figure 5.8. The figure shows clearly that along this crystallographic direction the STO and LCMO peaks are well separated, and the Laue oscillations of the sharp component correspond to the thickness of the film. A second component, with FWHM of about 0.2^o, is visible in the figure, and may be interpreted as due to the presence of very broad satellite peaks, whose nature will be discussed in the following section. This component is clearly due to the film, because it shows a maximum of intensity in correspondence of the film Bragg peak $[0\,0\,2]$. A third very broad component, close to the level of the background, instead, is the thermally-diffused scattering intensity from the substrate. Its

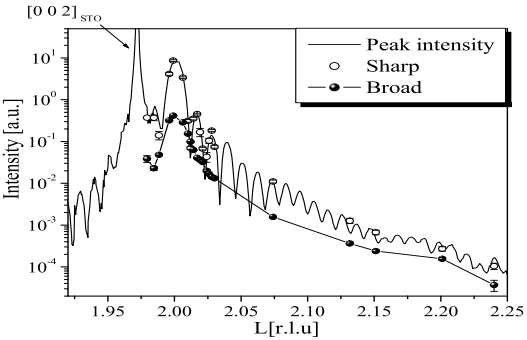

Figure 5.8: Longitudinal scan of the $[0\,0\,2]_c$ peak for the 400Å film (solid line). It is also shown the integrated intensity of the sharp (open circles) and the broad component (filled circles) of the transversal scans (θ-scan of the type shown in figure 5.7) at different values of L. The substrate peak is also shown

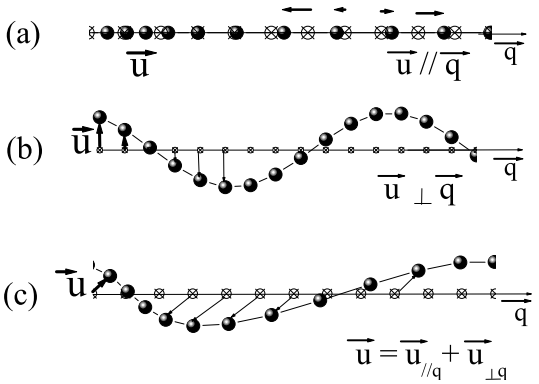

Figure 5.9: Example of (a) purely longitudinal displacive modulation (the atoms are shifted along the direction of the modulation), (b) sinusoidal displacive modulation, with polarization perpendicular to the propagation vector $\vec{q}$ and (c) combination of the two, the displacement of the atoms has a longitudinal and a transversal component

intensity shows a maximum in correspondence of the substrate position.

5.2.3 Discussion: *In-plane* modulation

The fact that $\vec{q}$ is independent on the value of the momentum transfer $\vec{Q}$ suggests that the side peaks can be considered as super-lattice (SL) peaks, a signature of an ordered *superstructure* present within the crystal structure of the film, with a characteristic length

$$L_0 = 2\pi/q \tag{5.1}$$

CTR scans (i.e. along the L direction) measured on the central peaks and both the "side" peaks, as shown in figure 5.5, show

thickness oscillations relative to the thickness of the film. This is an indication of the fact that the "super-structure" is coherent throughout the whole film thickness.

In order to analyse the nature of the modulation observed we have applied a model of displacive modulation. The atomic displacement from the ideal unperturbed position, $\vec{u}$, can be expressed as the sum of two component, one parallel and one perpendicular to the propagation vector of the modulation $\vec{q}$:

$$\vec{u} = \vec{u}_{//} + \vec{u}_{\perp} \tag{5.2}$$

Possible displacive modulation are shown schematically in figure 5.9.

To calculate the scattered intensity of a crystal with displacive disorder we need to modify the structure factor of the compound (equation (3.21), page 75) adding to the static atomic position vector in the unit cell $\vec{d_n}$ the displacement $\vec{u}_n$.

$$F_d = \sum_n f_n e^{2\pi i \vec{Q}\cdot(\vec{d_n}+\vec{U}_n)} \tag{5.3}$$

For a sinusoidal modulation the displacement $\vec{u}_n$ has the form

$$\vec{u}_n = \vec{U} cos(2\pi \vec{q}\cdot \vec{d_n}) \tag{5.4}$$

where $\vec{U}$ represents the amplitude vector of the displacement, and $\vec{q}$ is the propagation vector of the modulation. In order to calculate the scattered intensity of such crystal, one has to introduce the (5.4) in the equation (5.3), and develop the product $F \cdot F^*$. The result of such operation[3] is the following:

$$I = FF^*[1-2(\vec{Q}\cdot\vec{U}]^2 \sum_n f_n e^{2\pi i \vec{Q}\cdot\vec{d_n}})] + FF^*[\vec{Q}\cdot\vec{U}] \sum_n f_n e^{2\pi i(\vec{Q}\pm\vec{q})} \tag{5.5}$$

[3]Details of this procedure can be found in reference [99]

One finds that the Bragg intensity is reduced by a factor of $2(\vec{Q}\cdot\vec{U})^2$ while two superlattice peaks appear at a distance $\pm \mid \vec{q} \mid$ from the center with intensity I_{SL}

$$I_{SL} \propto F^2(\vec{Q}\cdot\vec{U})^2 \tag{5.6}$$

The modulus of the vector $\vec{q}$ is related to the periodicity of the real space modulation length L_0 (by the relation (5.1))

From equation (5.6) it is clear that the intensity of the SL peaks is maximum when the displacement $\vec{u}$ is parallel to the direction of the momentum transfer $\vec{Q}$. These considerations, together with the experimental results schematised in figure 5.2, which shows a sketch of the $H-K$ plane of the reciprocal lattice of the films analysed, indicate that the modulation is purely transversal. This is seen from the position of the SL peaks around $[H00]$- and $[0K0]$-type Bragg peaks, for which the vector $\vec{q}$ is always transversal to the momentum transfer $\vec{Q}$, and no longitudinal component is found. From the absence of a longitudinal component of $\vec{q}$ we can deduce (see equation (5.6)) that the displacement field $\vec{u}$ must be perpendicular to the propagation vector of the displacive field $\vec{q}$, i.e. in equation 5.2 the component $\vec{u}_{//} = 0$. Therefore, the modulation is purely transversal, as shown by the case (b) in figure 5.9.

The last important observation to be made is about the direction of the modulation: $\vec{q}$ is found to be always parallel to the crystallographic directions $< 100 >_c$ or $< 010 >_c$. The absence of SL peaks of the type $[H \pm q\, K \pm q\, L]$ is an indication of the fact that the modulation is one-dimensional. The presence of the SL peaks in both $< 100 >_c$ *and* $< 010 >_c$ directions is due to the presence of domains rotated by 90^o with respect to each other.

Finally, on the basis of the considerations made for the calculation of the structure factor and the intensity of the SL peaks, for the 100Å thick film, the absence of SL peaks around purely out-of-plane Bragg peaks tells us that the modulation has no component along the surface normal, being a phenomenon con-

film [Å]	a_c, b_c [Å]	$\vec{q}$ [r.l.u.]	L_0 *apparent* [Å]
100	3.905	0.01	350
400	3.905	0.0026	2300

Table 5.1: Summary of the experimental results relative to the in-plane modulation for the 100Å and the 400Å films

fined in the plane of the growth. For the 400Å thick films, instead, an out-of-plane component of the modulation should also be considered.

Results for the 100Å thick film

For this film, on the basis of the qualitative analysis we conclude that the presence of SL peaks with the characteristics described corresponds to a 1-dimensional displacive-like modulation, propagating in the plane a-b of the films along either the direction $< 100 >_c$ or $< 010 >_c$ with polarization field $\vec{u}$ perpendicular to the propagation vector $\vec{q}$, and with an *apparent* periodicity[4] in real space with wavelength $L_0 \approx 350$Å.

Results for the 400Å thick film

The value of $\vec{q}$ for the SL found in the 400Å thick film are associable to an in-plane transversal modulation with propagation vector along the crystallographic direction $< 100 >_c$ or $< 010 >_c$. and corresponds to an apparent periodicity $L_0 \approx$ 2300Å. Also in this case, scans along the L direction of the reciprocal lattice performed on the central and the SL peaks,

[4]The reason for calling the periodicity *apparent* will be clarified in section 5.3.5, where we will show that, on the basis of our model of periodic arrangement of crystallographic domains, the connection between the magnitude of the modulation vector and the real space periodicity length is not trivial, and cannot be expressed by the formula (5.1).

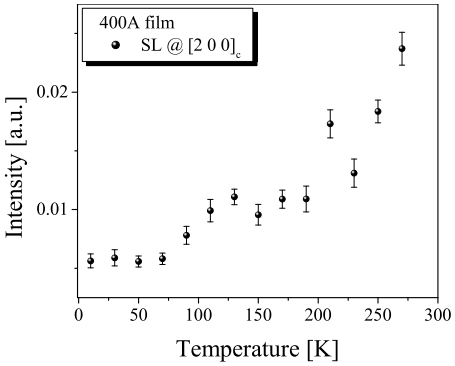

Figure 5.10: Temperature dependence of the intensity of SL peaks around $[2\,0\,0]_c$ peak of the 400Å thick film. Similar results are also found for the 100Å thick film.

show Laue oscillations with same periodicity. Also in this case the modulation is coherent in the whole film thickness.

The *broad* component of the $[0\,0\,L]$-type peaks, attributed to the presence of broad SL peaks, can also be associated to an *out-of-plane* modulation. The possible origin for this *out-of-plane* modulation will be discussed later (cf section 5.4.3).

5.2.4 Temperature dependence of SL peaks intensity

GID measurements have been performed on both samples in the temperature range 10–300K, in order to investigate the possible connections between their crystal structure and transport properties. A slight decrease of the SL peaks intensity with decreasing temperature has been observed for both samples (as shown in figure 5.10). As pointed out in the previous section, the intensity of the SL peaks is related to the structural mod-

ulation via the equation (5.6). The observed variation of the SL peaks integrated intensity suggests that a variation of the structural modulation occurs. This variation is reversible. Nevertheless, the SL peaks do not disappear completely, indicating that there is no drastic change in the film structure.

5.3 Our model: periodic arrangement of twin domains

At this point it is crucial to create a model of in-plane, one-dimensional, displacive modulation, which accounts for the results of our XRD investigation, including a reasonable origin of the long periodicity found for the 400Å film.

The model we have applied to the analysis of our data, and which we are going to present in this section, consist of an in-plane periodic arrangement of crystallographic domains, as a mechanism to relieve the strain induced by the substrate[5]. Our model of *twin domain modulation* (hereafter referred as TDM) is based on the idea that the match between two material with interatomic distances a_1 and a_2 is easier if it occurs via the tilt of one structure with respect to the other, instead of the contraction of the larger lattice or the elongation of the smaller. In other words the creation of a twin is energetically favorable with respect to the deformation of the unit cell, via elongation or contraction of inter-atomic distances. As we will show in the following, this model accounts for the appearance of the *in-plane* SL peaks, and can be easily extended to the out-of-plane modulation, and reproduces scattering profiles with a good agreement with the experimental results.

Before introducing the model in some detail it is worth spend-

[5]The model has been developed by Ulrich Gebhardt (based on an idea of Dr. P. Wochner) within his PhD thesis, we refer to his work and successive publications for a more accurate description of the model and its implications.

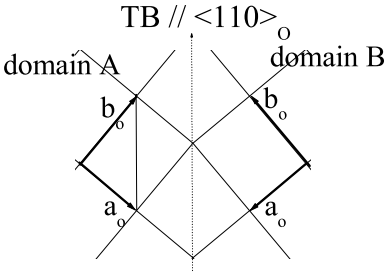

Figure 5.11: Example of a twin boundary along the $< 110 >_o$ plane, in an orthorhombic structure, in the $a - b$ plane

ing some more words on the mechanism of formation of twinning domains.

5.3.1 Twin domains

A twin domain (TD) is a coherent domain which forms in a particular crystallographic direction (typically $< 110 >$ i.e. the diagonal of the u.c.). This direction defines the mirror plane across which the crystal switches from one domain A to the specular domain B (see figure 5.11). The twins have this name from sharing the atoms at the corner of the unit cell and from forming coherently from one another without the formation of a phase boundary or a stacking fault. TD are present in several systems, and are particular to any symmetry groups which allow a mirroring of the structure, with consequent exchange of lattice parameters in one direction, without breaking the order of the crystal lattice. The structure across an ideal twin boundary (TB) looks ordered and coherent, and continues smoothly without breaking in any point.

From energetic considerations the formation of a TB is favored in certain directions with respect to others. Often this is a favorable way to relax strain compared to other mechanisms such as the creation of dislocations or stacking faults, because ideal TDs do not involve atomic displacements. For this reason, during the epitaxial growth of a film with strain induced by the lattice mismatch with the substrate, a continuous interexchange of domains of the form ABABA... of the film could be energetically more favorable than the distortion of the unit cell to match the in-plane atomic spacing.

Therefore, the periodic arrangement of domains can be viewed as a way to relax the elastic strain induced by lattice mismatch. In this respect the model is applicable to all systems allowing the formation of twins, when grown as epitaxial thin film on a substrate with considerable lattice mismatch.

As already discussed in chapter 2, in literature there are a few examples of twin modulated structures, especially detected by TEM technique. Zandbergen et *al.*[64] and Lebedev et *al.*[68] have separately found evidence of an interchange of twin domains in epitaxial films in absence of interfacial disorder or dislocations. These latter strain relief mechanisms tend to favor a relaxed film growth leading to physical properties similar to bulk.

5.3.2 Reciprocal lattice of a single twin domain

For the TB within the orthorhombic crystal structure (figure 5.11) the ratio of the in-plane lattice parameters a_o/b_o defines the orthorhombicity of the crystal. In figure 5.12 a section of a crystal lattice including a TB is shown. The pseudo-cubic coordinates are also shown. The angle α represents the tilt of the crystal lattice across the TB measured with respect to the pseudocubic coordinates and is connected to the orthorhombic-

ity a_o/b_o by the following equation:

$$\alpha = 90^o - 2\arctan\frac{a_o}{b_o} \tag{5.7}$$

For a given angle α it is relatively simple to calculate the reciprocal lattice of a TD which results from the summation of the reciprocal lattices from the domains A and B tilted by the same angle α. Notice that in the pseudo-cubic coordinates the angle between the lattice parameters a_{pc} and b_{pc} is slightly different from 90^o, such that it differs in the pseudo-cubic reciprocal lattice as well. The reciprocal lattice resulting from such a combination is shown in figure 5.13. For a TB along the $< 010 >_c$ direction, the Bragg peaks along the $< 100 >_c$ direction are unmodified, while the ones along the $< 010 >_c$ direction are tilted with respect to the ideal cubic lattice by an angle of $\pm\alpha$ (respectively for the domain A and B in the figure).

It is very important to point out that the distance of the peaks from the ideal positions, indicated by $\vec{dq}$ in figure 5.13, increase with increasing $\vec{Q}$. This is the most important signature of the presence of twinning within a crystal structure. It is not to be confused with the SL peaks associated to a structural modulation, appearing in the reciprocal space always at the same distance from the (central) Bragg peak at all the values of $\vec{Q}$, as found in our measurements (see figure 5.4).

5.3.3 Periodic arrangement of twin boundaries: a simple model

We describe now in more detail the model of periodic arrangement of domains (or TDM as defined before) which could be responsible for the appearance of SL peaks in the XRD patterns. We will describe this model in pseudo-cubic coordinates. As already discussed, the modulation propagates in-plane along the crystallographic directions $< 100 >_c$ and $< 010 >_c$ and is characterized by the angle α already introduced in equation 5.7,

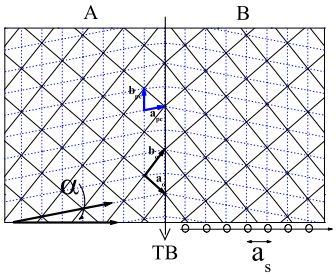

Figure 5.12: Schematics of a TD in the $a-b$ plane, which favor the matching between film (dashed line) and substrate (open circles) lattice. The orthorhombic and pseudo-cubic coordinates are highlighted

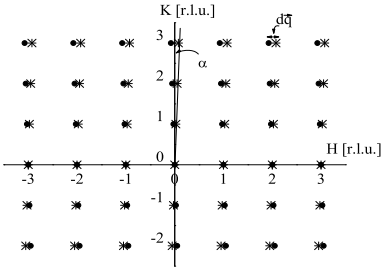

Figure 5.13: Sketch of the reciprocal lattice of a twinned structure with the domains A (dots) and B (stars) tilted by an angle α. In pseudo-cubic-coordinates

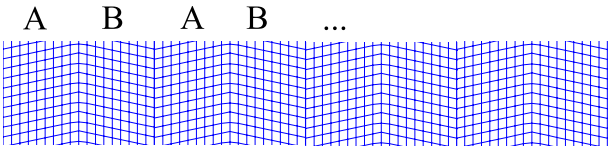

Figure 5.14: TDM: sketch of a periodic arrangement of twin domains, for a simple system with a pseudocubic unit cell that contains only one e^-

.

as shown in figure 5.14. In the case of an orthorhombic film in epitaxial relationship with the substrate, the angle α can be written in terms of the substrate lattice parameters:

$$\alpha = \arccos\left(\frac{a_{Sub}}{a_{pc}}\right) = \arccos\left(\frac{a_{Sub}}{\frac{1}{2}\sqrt{a_o^2 + b_o^2}}\right) \qquad (5.8)$$

To simplify the model and make it independent of particular systems we consider a pseudo-cubic lattice made of a unit cell containing only one e^-. Due to the fact the the modulation is one-dimensional we can further simplify the model considering only one line of atoms, instead of an atomic plane or atomic lattice.

To explain the mechanism of formation of the periodic arrangement of twin domains consider a line of atoms of the STO substrate along the $< 100 >$ direction, separated by a distance a_s, and a line of atoms of the film lying on a corner of a pseudocubic cell, with interatomic spacing $a_f^{pc} > a_s$. On the basis of the TDM model, the atoms of the film align on the atoms of the substrate along a direction tilted by an angle α with respect to the $< 100 >_c$, as shown in figure 5.15. Because of the underlying structure of the substrate, after a certain number of u.c. $\tilde{N}$, the line of atoms of the film has to reverse the tilt by mirroring the structure with respect to the $< 010 >_c$ direction, creating a

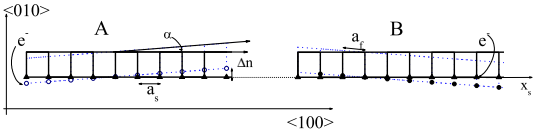

Figure 5.15: Formation of TD during the epitaxial growth of a film (open and closed circles) on a substrate with lattice parameter a_s (triangles): one-dimensional model. Top view.

twin domain (A in figure 5.15). This happens when the distance Δ_n between the n_f^{th} atom of the films and the n_s^{th} atom of the substrate becomes energetically unfavorable, i.e. too large to be physically acceptable. The two "tilted" lines of atoms represent the two twin domains A and B. Applying the same consideration to the domain B, a continuous inter-exchange of domains ABABA... is expected, all with similar length, forming an "ordered" pattern of TDs, which looks like a "superstructure" superimposed onto the crystal lattice (cf. figure 5.14).

In order to calculate the diffraction pattern that is produced by such structure, it is necessary first to calculate the size distribution of the domains, then add coherently the scattered radiation from each unit cell of the two domains.[6]

5.3.4 Domain size distribution

To calculate the domain size distribution it is important to understand which are the physical mechanisms underlying the process of formation of TBs.

As explained in the previous paragraph, the tilt angle α represents the orthorhombicity of the film (and *not* of the bulk). It contains information about the epitaxial strain, and is the

[6]Is it not enough to invent a domain distribution instead of creating it from probability of changing domain because the physics, energy balance, maximum number of u.c. in each domain, tilt angle, is in that probability.

first variable of the model. It is an intrinsic parameter of the system, evaluable via the equation 5.8, provided that one knows the lattice parameters of the film. The second important physical parameter we have already encountered is $\tilde{N}$, the maximum number of u.c. allowed in each domain. This is related to the energetics of the system, elastic energy and epitaxial strain, and is less easily accessible: in our model it will be treated as variable. The third parameter σ is also related to energetics, and comes from the formalisation of the domain formation as described in the following. We can formalise the problem by evaluating the probability of an atom j to belong to one of the domains A or B in terms of combined probability to belong to the same domain as the $(j-1)^{th}$ atom belongs to or to the other domain. In this way, the probability of each j^{th} atom depends on the probability of the atom $(j-1)^{th}$ with the final result that the probability distribution depends very strongly on the starting point. Let the probability of belonging to the domain A and B be $p\uparrow$ and $p\downarrow$, respectively. These may be expressed as exponential functions depending on the position j (being maximum at $j=\tilde{N}$) and decaying with a characteristic length σ, which determines the width of the domain length distribution:

$$p\uparrow = e^{\frac{j-\tilde{N}}{\sigma}} \tag{5.9}$$

$$p\downarrow = e^{\frac{-j-\tilde{N}}{\sigma}} \tag{5.10}$$

The probability of the two domains is considered to be the same, due to the cubic symmetry of the substrate (i.e. same inter-atomic distances in both the in-plane crystallographic directions) which explains the presence of two domains rotated by 90^o discussed at page 113. Combining the probability functions expressed in eq. 5.9 and 5.10, the domain size distribution is found and is characterised by an average value L_0 of the domain length and of width ΔL_0. Figure 5.16 demonstrates the appearance of a domain size distribution, using the parameters

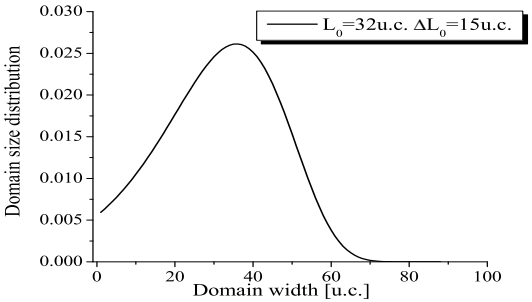

Figure 5.16: Domain size distribution for $L_0 = 32$u.c., $\Delta L_0 = 15$u.c. and $\alpha = 5^o$

$\tilde{N} = 43$, $\sigma = 10$. It is important to notice that there is not a direct correspondence between the value of $\tilde{N}$ and L_0 because the domain distribution L_0 depends on the combination of the three parameters σ, $\tilde{N}$ and α. Moreover, once the domain distribution is calculated, the only parameters with practical physical relevance are α, L_0 which represents the average domain size and ΔL_0 which represents the width of the distribution. The parameter ΔL_0 gives an idea of the sharpness of the periodicity, i.e. the degree of "order" of the distribution of domains.[7]

5.3.5 Diffraction pattern of a structure with TDM

From the knowledge of the domain distribution and the evaluation of the correlation function between two atoms j and i belonging to the lattice, the calculation of the diffraction pattern is straightforward. The results of such calculations for the values of the parameters L_0, ΔL_0 and α corresponding to the

[7] A more detailed description of the calculation of domain size distribution can be found in the PhD thesis of U. Gebhardt.

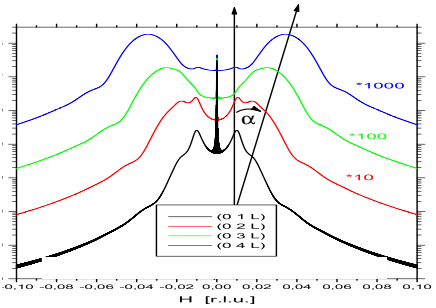

Figure 5.17: Transversal diffraction profiles for the peaks [H00], with H=1,2,3,4 corresponding to the structure with a domain size distribution for $L_0 = 32$u.c., $\Delta L_0 = 14$u.c. and $\alpha = 5^o$

distribution of the figure 5.16, are shown in figure 5.17

As discussed in section 5.3.2, the signature of a super-periodicity of wavelength L in a crystal lattice is the presence of SL peaks in the reciprocal space, at a fixed distance from every Bragg point defined by the equation 5.1. On the other hand, the presence of twin domains generates a "splitting" of the Bragg peaks in the direction parallel to the direction of the TB -in our case $< 010 >_c$, whose distance from the ideal cubic position increases with increasing $\vec{Q}$ depending on the tilt angle α (TD peaks). In the diffraction patterns of a TDM, as in Figure 5.17, both of these features are evident. The scattering profiles contain information about both the presence of the twin domains and their periodic distribution.

The peaks have different shapes depending on the parameters L_0, ΔL_0 and α. The sharpness of the SL peaks depends mainly on the distribution width and the coherence of the lattice, while the intensity of the TD peaks, together with their position in the reciprocal space, depends mostly on the angle α. The determination of the domain distribution from the dif-

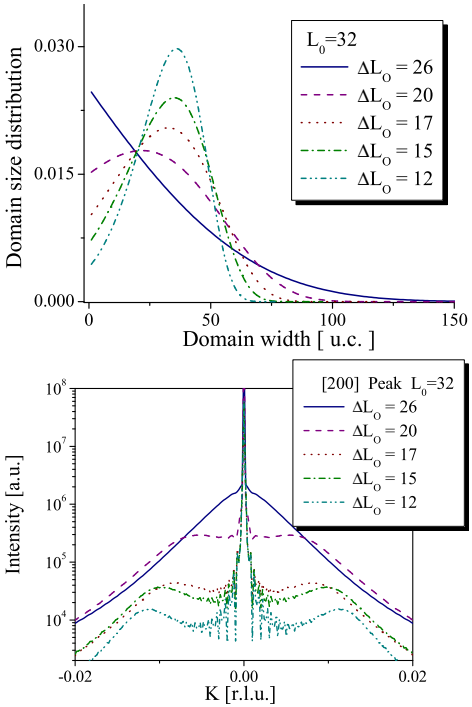

Figure 5.18: Domain distribution for fixed L_0 and different width ΔL_0 and relative diffraction profiles of the peak [200]

fraction pattern is not so straightforward, nor intuitive. It is deducible with a fitting process, or an accurate simulation but not from simple mathematical considerations. The equation 5.1 does not hold in this case, the quantity q being connected to all the variables α, L_0 and ΔL_0 in a non-trivial way.

To emphasize this point we calculate the scattering profile of domain distributions with the same average value L_0 and different width ΔL_0. One would normally expect that the position of the SL peaks in the reciprocal space would be the same for each distribution, by just being related to the value L_0 with the equation 5.1. However, we see that this is not the case, the plots in figure 5.18 show, respectively, an example of domain size distribution profiles with fixed L_0 and different widths. As can be seen in the figure the scattering profiles are very different. The separation of the SL peaks is expected to be the same, but clearly changes with different widths and for each distribution there is a different set of SL peaks. In this example, not only the width of the SL peaks but also their actual position in the reciprocal space depends on the distribution of domain size, and the coherence of the modulation in the real space. This is one of the most interesting results of our model, which can give new insight on the interpretation of the satellite peaks in complex structures.

Several more features should be highlighted resulting from the model. For example, if the periodicity of a distribution is very well defined, higher order SL peaks appear in the diffraction pattern, which is a well known result from multilayer structures. In the extreme case of a very broad distribution, strongly asymmetric and centered around zero (as is the case of the continuous line in figure 5.18), the SL peaks assume the form of diffuse scattering around the central peak, where no features can be recognised (continuous line in figure 5.18). Finally the dependence of the scattering profile on the twin angle α is quite marked; the TD peaks are 'convoluted' with the SL peaks and shift their position along the direction of the tilt α,

as highlighted in figure 5.17.

5.4 Results: simulated and measured scattering pattern

This simple model of TDM has been used to simulate the XRD profiles measured on our samples and shown before. Considering that the model is so simplified, and does not take into account internal degrees of freedom of the unit cell together with other effects like the thermally diffuse scattering or mosaicity of the sample, the agreement between measured and calculated scattering profiles is quite amazing. Moreover, the model which is based on the assumption of a compressive strain (i.e. $a_f > a_s$) also seems to apply well to these films grown under a "tensile" strain ($a_f < a_s$). This point deserves a more detailed discussion about the mechanisms which take place in epitaxial growth.

The *pseudomorphic* growth of a structure on a substrate requires a matching between the lattice parameters at the interface between the two compounds. When this is not already the case for the bulk relaxed structures the strain imposed by the substrate on the film acts as a modifying agent on the film structure itself. The pseudomorphic growth is then the result of an energy balance between the tendency of the crystal lattice to grow relaxed, following the internal energy balance, and the external "pressure" of the substrate acting as a template-structure. Moreover, as already discussed previously, for orthorhombic perovskites the formation of TD has a primary role in the energy balance of the crystal growth.

The applicability of the TDM model described to our system requires the following important condition: the in-plane lattice parameter a_{pc} of LCMO film becomes *larger* than the one of the STO a_{sub} because of the tilt α (cf eq. (5.8)), even though the epitaxial strain is *tensile*. This can be justified from the competition between the tendency to the formation of TD and the

L_0[u.c]	L_0[Å]	ΔL_0[u.c.]	ΔL_0[Å]	$\alpha[^o]$	b_o/a_o
32	125	16	62	0.06	≈ 1

Table 5.2: Domain size distribution and orthorhombicity for the 100Å film

epitaxial growth. The energy balance tends to favor the formation of TD's, while the epitaxial relationships force the matching of the in-plane lattice parameters of LCMO with STO. The resulting atomic configuration consists in a periodic arrangement of TD of LCMO with an enlarged lattice parameter and reduced tilt angle α. The change in the length of the lattice parameter can partly be compensated by a reduced tilting of the octahedra MnO_6.

Due to the complexity of the model the structure factor and other correction terms have not been taken into account. The results presented in this section are re-scaled with respect to the intensity of the SL peak, and are expressed in terms of arbitrary units (a.u.).

5.4.1 100Å film

Figure 5.19 shows a comparison between the experimental data and the simulation of the scattering profile of the 100Å LCMO film. The dots correspond to the data points and the line to the simulation, obtained using the parameters shown in table 5.2:

The domain size distribution profile corresponding to these parameters is also shown. It is worthy to notice that the calculated periodicity of the TD for the 100Å sample corresponds to an average domain size $L_0 \approx 125$Å , which is much smaller than the periodicity expected from the formula (5.1). For this reason, we have called the periodicity *apparent* in the section of the experimental results (cf page 114). Moreover, as expected from the discussion at the beginning of this section, the tilt an-

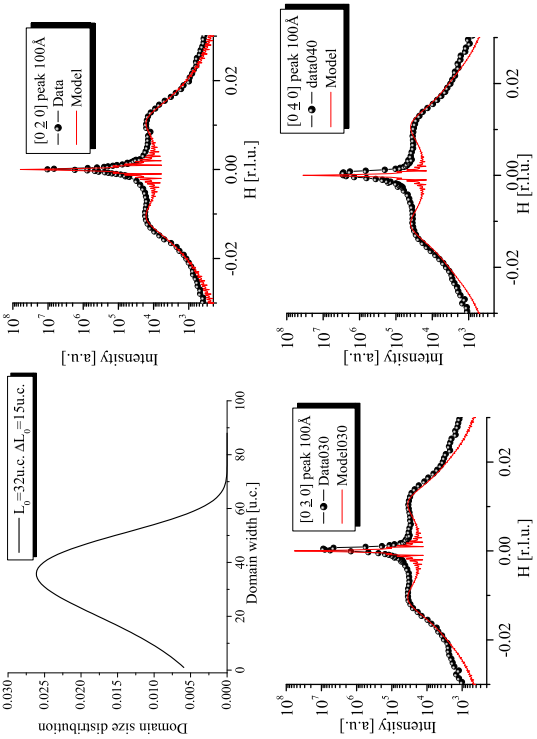

Figure 5.19: Simulated diffraction profiles for the 100Å film. The domain size distribution and the diffraction curves for different scattering vectors are shown.

gle α does not correspond to the LCMO bulk orthorhombicity (which is $\alpha_{bulk} \approx 0.31$) because of the epitaxial strain induced by the substrate.

5.4.2 400Å film

The case of the 400Å film is more complicated. The shape of the diffraction peaks shows two main features. First, the SL are very close to the main peak and quite sharp on the top. Secondly, the diffuse intensity far from the central peak has an exponential decay, which is quite uncommon. To reproduce such profiles a "distribution" of TDM periodicities has to be considered. The model we propose consists in a variation of TD distribution along the c-axis, due to a strain *relaxation* effect. This particular process of *strain-relaxation* corresponds to an increase of disorder in the TD periodicity, i.e. an increased average domain size and a broadening of the distribution. Even though, the strain induced by the substrate is not relieved completely, and the structural properties of the films do not become the ones of the bulk relaxed system.

The tilt angle for the 3 distributions is the same as the one found for the thin films, i.e. $\alpha = 0.06^o$, although a change (and in particular an increase towards bulk value) is expected from the process of relaxation of the structure. Simulations of scattering profiles from *in-plane* TD distributions characterised by different tilt angles, and same value of L_0 and ΔL_0, show that the variation of α alone is not enough to reproduce the data. Furthermore, for a good agreement between simulated and measured profiles, the parameter α should not exceed the value of 0.07^o. Finally, due to the fact that the introduction of such small change does not introduce any further improvement of the simulation, and considering that at this level the model is still qualitative, in our simulations α has been kept constant at the value of $\alpha = 0.06^o$. On the basis of the previous discussion, we can argue that the variation of α in the distribution of domains

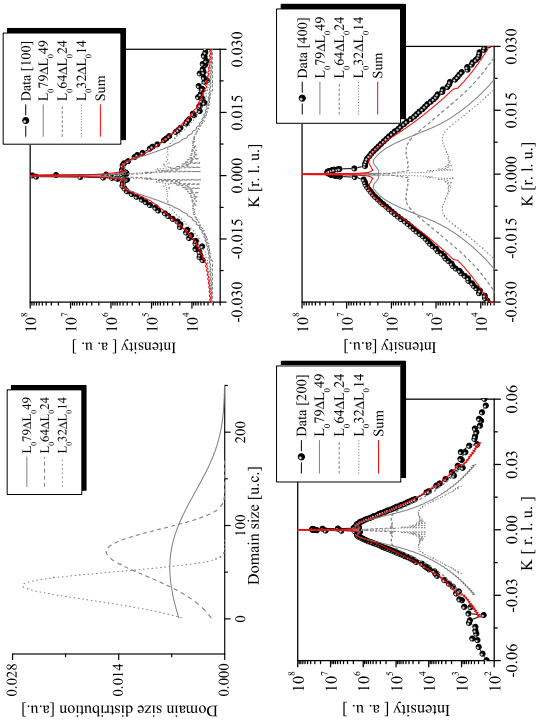

Figure 5.20: Simulated diffraction profiles for the 400Å film: domain size distribution and diffraction curves

distribution	L_0[u.c]	L_0[Å]	ΔL_0[u.c.]	ΔL_0[Å]
1	79	308	49	191
2	64	250	24	94
3	32	125	14	62

Table 5.3: Distribution of TD for modeling the data relative to the 400Å film

along the c direction does not exceed the 20%, i.e. the tilt angle stays always around 18–19% of the bulk value.

The change of the domain distribution is probably smooth, i.e. there is not a net change in the distribution profile at a certain thickness, but in our simplified model, to support our statement, we just consider three different distribution profiles that, as we can see in the comparison between simulated and experimental curves, are enough to get a good agreement with the data. The domain size distribution which give the best agreement with the experimental results are displayed in the table 5.3.

The model of structural "relaxation" in the direction of the growth parallel to the c-axis, i.e. an increased disorder in the periodicity of the TD toward the surface, is confirmed by CTRs measurements which will be presented in the next chapter.

5.4.3 *Out-of-plane* modulation in the 400Å film

For the 400Å film, the transverse scans around $[0\,0\,L]$-type reflections present a sharp and a broad component. As already illustrated before (cf page 109), the sharp component is the film Bragg peak, while the origin of the broad component has been ascribed to the presence of *an out-of-plane* modulation, which we will try to explain within the TDM model presented in this chapter.

We claim that the broad component can be interpreted as

due to two very broad SL peaks. These SL peaks have the same origin as the in-plane ones, i.e. a TDM (or, better, a component of a TDM) that propagates in the plane og the growth, with atomic displacements along the direction of the growth. This modulation can have two possible origins. The first possibility consists in the presence of a *monoclinic* distortion of the LCMO unit cell, which would account for the identical periodicity in both the in-plane *and* the out-of-plane directions.

The second hypothesis consists in the presence of some LCMO crystallographic domains with the $c-$axis in the plane of the film (and a and b axis at 45^o from the surface normal). In this case TD with twin axis $< 110 >_o$ parallel to the surface-normal could produce a similar periodicity along this direction. However, the relative intensity of the SL peaks for the $[0\,0\,L]$-type reflections with respect to the central component is much smaller than for the in-plane peaks (their integrated intensity is only $\approx 10\%$ of the SL measured for $[H\,K\,0]$-type peaks)[8]. This would indicate a very small population of these kind of domains. Moreover, the small intensity measured along the CTR of the broad component alone (filled circles in figure 5.8) and the absence of clear thickness oscillations, are a sign of a very small volume that scatters coherently. The weak intensity of the radiation diffracted from these domains could justify the absence of Bragg peaks relative to the c spacing in the GID measurements. However, the strain induced by the substrate would not justify the presence of twin domains arranged *periodically* along the direction of the growth. For this reason, the first hypethesis seems to be more acceptable.

The scattering profile of the peak [0 0 2] of the 400Å film, shown in figure 5.7, can be reproduced applying our model of TDM. The domain size distribution corresponding to the best

[8]It is important to note that, wihle along the $[0\,0\,L]$ direction the film and substrate Bragg peaks are separated, the $[H\,K\,0]$-type peaks always contain both contribution. Even in this case, the relative intensity of the SL peaks versus the central component is bigger in the in-plane type peaks.

simulation correspons to the following parameters: $L_0 = 78$u.c., $\Delta L_0 = 57$u.c. and tilt angle $\alpha = 0.07^o$. These values correspond quite well to the value found for the in-plane distribution of the TD for the 400Å film. In conclusion, the presence of a *monoclinic* distortion of te unit cell would not require the introduction of crystallographic domains with c-axis oriented in the plane of the growth and would account for the same periodicity of the *in-plane* and *out-of-plane* modulations.

5.5 Conclusions

In conclusion, the model of TMD is capable of reproducing the experimental data relative to 100Å and 400Å thin films. In both cases this modulation has a strong in-plane component and, for the thicker sample, only a small out-of-plane component. The periodicity of the Laue oscillations measured on the broad component of the *in-plane* SL peaks, as illustrated in section 5.2, corresponds, in both cases, to the whole film thickness. This is a clear indication of the fact that the in-plane component of the structural modulation of the films is coherent in the whole thickness.

For the 400Å thick film, the weak *out-of-plane* component can be associated to a modulation propagating in the plane of the growth, with atomic displacements along the surface normal. We cannot either exclude the presence of a monoclinic distortion of the thick film, nor the presence of a small percentage of domains with $c-$axis in the plane of the growth. Both would account for the appearance of the out-of-plane structural modulation, within our proposed model. However, the hypothesis of monoclinic distortion would explain the same periodicity found for the TDM in the two directions. In either case, from the very weak intensity of the *out-of-plane* SL peaks (cf. figure 5.8), we can argue that this modulation is not very coherent in the thickness of the film.

The temperature dependence found for the intensity of the

SL peaks can be ascribed to a variation of the film structure, which does not show any correlation with the transport properties. Moreover, the persistence of the SL peaks in the whole range of temperature investigated indicates that the structure of the films is orthorhombic (or monoclinic, in the case of the 400Å film) and no structural phase transformation occurs. However, on the basis of the proposed model, the disappearance of the SL peaks is related to an increase of the crystal symmetry of the system, while a reduction of the tilting angle α would be related to a decrease of the orthorhombicity of the film. The suppression of the metallic behaviour in the FM phase in very thin films (epitaxialy strained) could be associated to a structural change, from the orthorhombic to the cubic symmetry. In this case one would expect a complete insulating behaviour in case of strongly distorted layers[104], e.g. pseudomorphic thin layers with cubic symmetry.

5.5.1 A comparison: Sr-doped films

As discussed in section 5.4, page 128, this model of TDM is expected to be naturally applicable to systems with *compressive* strain. In this case, no strong changes of the lattice parameters are expected.

In order to compare the effect of tensile and compressive strain, we shortly illustrate the results of structural investigations performed on Sr-doped films ($La_{0.88}Sr_{0.1}MnO_3$), epitaxially grown by PLA on STO substrate. This study has been performed by Ulrich Gebhardt, within his PhD thesis.

In the case of LSMO films, the mismatch between the two structures leads to a *compressive* strain of the films structure. A TDM has been observed also for this films, with the following characteristics. The presence of high-order SL peaks around [H K L]-type Bragg reflections demonstrates the presence of in-plane *and* an out-of-plane modulation with a narrow domains size distribution. Consequently, the structure of the films is

more homogeneous. Moreover, while in the case of LCMO films the tilt angle α is strongly changed with respect to the bulk ($\alpha_{film} \approx 18\%$ of α_{bulk}), in the case of LSMO, the change is less dramatic, and decreases with increasing thickness. This shows that the TDM in the case of compressive strain requires a smaller structural distortion of the unit cell, and induces a better periodicity of the TD distribution.

The TDM parameters that better reproduce the experimental curves show a thickness dependence, which has the same qualitative behaviour as for the LCMO films, studied for the present work. With increasing thickness, the average domains size increases, and the distributions broaden. Moreover, a clear change of the tilt angle α towards the bulk value is observed. The model parameters for a 250Å and 650Å thick film are summarised in the following:

	250Å	650Å
α	0.34^o	0.52^o
L_0	25u.c.	40u.c.
ΔL_0	6.5u.c.	14u.c.

Most interestingly, temperature dependent structural measurements on 250Å thick films give a clear indication that a phase transition occurs. At $T \approx 200K$ the film undergoes a structural transition from the high temperature *triclinic* symmetry (a distorted rhombohedral unit cell) to a low temperature monoclinic structure (with higher symmetry). The signature of this phase transition is the strong reduction ($\approx$ 10 times) of the out-of-plane SL peaks intensity (relative to a triclinic structure) and the appearance of Bragg peaks relative to a monoclinic structure. Transport measurements performed on the same sample show that an insulator-metallic transition occurs at the same temperature (i.e. $T \approx 200K$), along with a PM-FM transition. The FM metallic state observed in the film is not found in the bulk, where a FM insulating state is present, instead. The strong correlation between structural and insulator-

metallic transitions suggest a correlation between structure and transport properties of the strained thin films, where a metallic state appears in correspondence with the higer symmetry of the crystal lattice.

Chapter 6

CTRs measurement and model of c-axis gradient

The study of the out-of-plane crystal structure of these samples completes the picture of the structural properties of the thin films and helps us to have an overall picture of their morphology and structure. This has been accomplished with the help of CTRs measurement and analysis, already introduced in chapter 3. The geometry used for the CTRs measurements is the z-geometry, i.e. incident and diffracted beam directions make the same angle with the surface, in this case there are no asymmetric absorption effects to be considered in the analysis of the Bragg peaks. As already discussed in section 3.5, we have not measured the CTRs with GID setup, so the data collected do not give any information about the depth-dependence of out-of-plane structural properties. All the results which will be discussed about c-axis gradient have been obtained by modeling and fitting of data. The information obtained by CTRs measurements are essentially of two kinds:

(a) coherence of the crystal structure along the c-axis, included the TDM[1]

[1] see chapter 5

(b) non-homogeneity of the lattice spacing along the c-axis direction

6.1 Measured CTR's

CTR measurements have been performed on the 400Å sample at the BM28 (XMaS) beamline of the ESRF in Grenoble, described in section 3.6, and at the MPI-surface beamline at ANKA in Karlsruhe. Figure 6.1 shows typical data along the $[3\,2\,L]_o$[2] CTRs. The profiles show two main characteristics:

1. Marked Laue oscillations around every Bragg peak with very pronounced minima.

2. Strong asymmetry in the intensity distribution around the Bragg points, the intensity being lower for the low $\vec{Q}$ side of the peak and higher for the high $\vec{Q}$ side. The asymmetry also becomes more pronounced with increasing $\vec{Q}$.

The strong amplitude of the Laue oscillations is consistent with an ordered and coherent crystalline structure of the film. The solid line in figure 6.1 corresponds to a simple model of the CTRs data assuming a homogeneous spacing of crystallographic planes parallel to the surface (c-axis). The periodicity of the oscillations of the model are consistent with a coherent thickness 377Å, corresponding to 49 unit cells with an average c lattice parameter $c_{av} = 7.70$Å. The simple model obtained using the structure factor of the LCMO films, described in chapter 3, does produce some asymmetries in the scattered profiles. These asymmetries are due to interference effects between atoms of the same elements whose position inside the u.c. is displaced with respect to the ideal perovskite structure. However, it is clear

[2]Note: in the following discussion we will always use the orthorhombic notation, and the $_o$ will be eliminated.

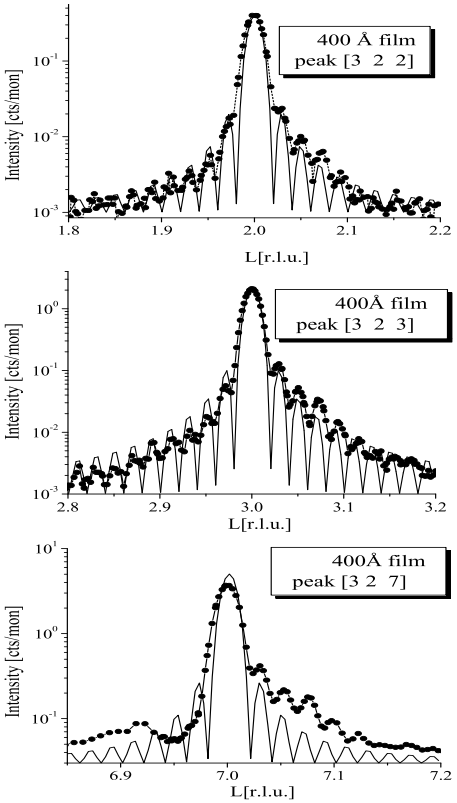

Figure 6.1: Example of strong asymmetry of the CTRs around some Bragg peaks

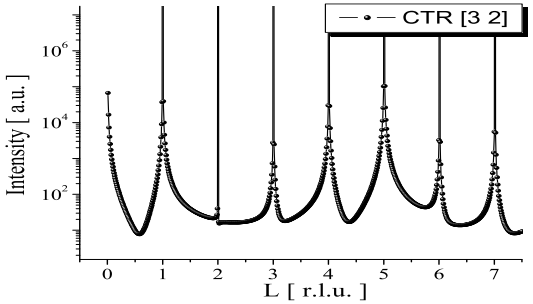

Figure 6.2: Example of bulk rods of LCMO. The asymmetry in the intensity around the Bragg points is due to interference of atoms inside the u.c.

that this simple model cannot account for the strong asymmetry features observed in the experimental profiles, and a more complex model is necessary.

6.2 Domain structure of LCMO and reciprocal lattice orientation

For the modeling of the CTR data it is necessary to consider the presence of crystallographic domains, due to the symmetry of the system, and the TDM model proposed for these films in chapter 5. This is because, in a domain system, the intensity of an arbitrary point [H K L] in the reciprocal space arises from a combination of scattering from Bragg peaks belonging to different domains. In order to try to disentangle the different scattering contributions it is necessary to model the CTR data, taking into account the domain distribution in the structure factor calculation. Therefore, the indexing of peaks of a domain system is intrinsically arbitrary.

In the case of these LCMO films, due to the pseudo-cubic symmetry, the Bragg peaks contributing to the intensity in a reciprocal lattice point, arbitrarily indexed, $[H\,K\,L]$ may be $[H\,K\,L]$, $[\bar{K}\,H\,L]$, $[\bar{H}\,\bar{K}\,L]$ and $[K\,\bar{H}\,L]$ (see figure 6.3). Each of these peaks corresponds to a different domain, obtained by a 90^o rotation of the $H\,K$ plane around the surface normal. Due to the symmetry of the system, the structure factor of these peaks are different.

It is important to note that in this special case we assume the L direction being well defined, and corresponding to the direction of the growth. This assumption seems to be in contrast with the hypothesis described in the previous chapter (cf. page 109) that the films could present domains with $c-$axis in-plane (a and b axis making an angle of 45^o with respect to the surface normal). Nevertheless, that hypothesis remains non-proven, and the absence of clear Bragg peaks corresponding to a or b spacing in the c -direction, and vice-versa (i.e. no c-domains are present in the $a-b$ plane) makes it controversery.

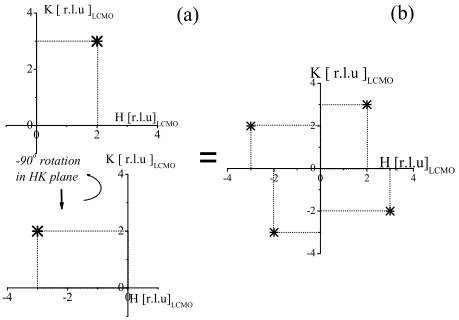

Figure 6.3: (a) Origin of the degeneracy of the rlp: the 4 successive rotations of the reciprocal space around $c*$ generate the degeneracy summarised in (b). Orthorhombic coordinates are used

An accurate crystallographic analysis, allowing us to deduce the population of each domain, is beyond the scope of this thesis. We might start with the assumption that the domains are equally populated, each pair of Miller indexes (i.e. domain) having equal probability 1/4.

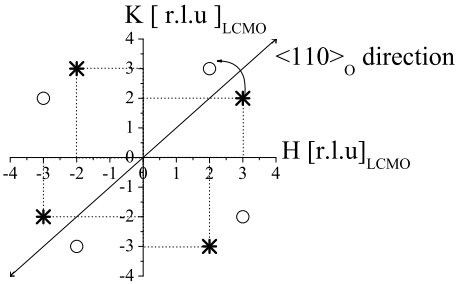

Figure 6.4: Mirroring of reciprocal lattice with respect to the $< 110 >_o$ direction (which corresponds to the $< 100 >_c$)

Moreover, in this special case an additional domain degeneracy comes from the presence of TD. In orthorhombic coordinates the reciprocal lattice of a TD is obtained mirroring the HK plane with respect to the direction $< 110 >_o$. Performing this operation on the reciprocal space coordinate system plotted in figure 6.3, we obtain 4 more peaks in the position $[H\ K\ L]$, as shown in figure 6.4. We label them as $[K\ H\ L]$, $[\bar{H}\ K\ L]$, $[\bar{K}\ \bar{H}\ L]$ and $[H\ \bar{K}\ L]$. After these this operations, we obtain a total of 8 possible domains for this system, i.e. 8 possible Bragg peaks contributing to the intensity in the same point of the reciprocal space of the sample measured. However, for symmetry reasons all the peaks satisfying the relation $H\ K = \bar{H}\ K$ have the same structure factor (cf figure 6.5), therefore the number of possible domains reduces to 4.

The following discussion is concerned with the analysis of

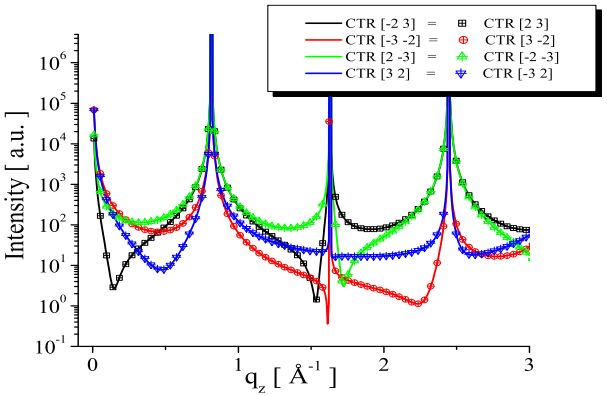

Figure 6.5: Rods with the same structure factor

the [2 3] CTR. On the basis of the above discussion, the model of our data considers the superposition of the CTRs $[3, 2]$, $[\bar{2}\,3]$, $[\bar{3}\,\bar{2}]$ and $[2\,\bar{3}]$ from 4 different crystallographic domains. This superposition can be considered as either an incoherent or a coherent sum, which give two different results. While an incoherent sum involves the sum of the intensity of each CTR $I_{[HK]}$, a coherent superposition involves the sum of the amplitudes of the scattered waves $A_{[HK]}$, and contains interference terms.

$$\text{incoherent sum} \qquad I_{inco} = I_{[3,2]} + I_{[\bar{2}\,3]} + I_{[\bar{3}\,\bar{2}]} + I_{[2\,\bar{3}]} \tag{6.1}$$

$$\text{coherent sum} \qquad A = A_{[3,2]} + A_{[\bar{2}\,3]} + A_{[\bar{3}\,\bar{2}]} + A_{[2\,\bar{3}]} \tag{6.2}$$

$$I_{co} = A^2 = I_{inco} + 2A_{[3,2]}A_{[\bar{2}\,3]} + 2A_{[\bar{2}\,3]}A_{[\bar{3}\,\bar{2}]} + \ldots \tag{6.3}$$

Twin domains are by definition coherent, therefore the summation of the diffracted intensity from the TD has to be coherent. However, due to the broad distribution of TDs found in our

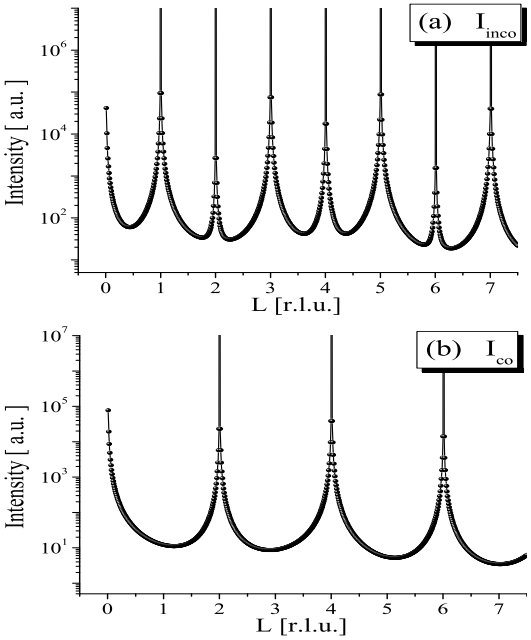

Figure 6.6: Example of (a) incoherent and (b) coherent sum of the 4 domains, corresponding to the CTRs $[3, 2]$, $[\bar{2}\,3]$, $[\bar{3}\,\bar{2}]$ and $[2\,\bar{3}]$ (see text)

films (see 5.19, page 130), and to the variation of the domain size distribution along the c-axis (see 5.20, page 132), it is perhaps more reasonable to suppose an incoherent sum of domains contributing to the CTRs. In this case the relevant equation is 6.1. A model assuming a coherent sum of the $[3, 2]$, $[\bar{2}\,3]$, $[\bar{3}\,\bar{2}]$ and $[2\,\bar{3}]$ CTRs is shown as example in figure 6.6(b). It can clearly be seen that some of the intensity at the Bragg position is zero by the coherent sum, which is not the case in the measured rod (figure 6.7). The results, i.e. suppression of intensity at some Bragg positions, are similar for a coherent sum of the intensity of any combinations of the domains considered. The disagreement with the data is evident, demonstrating that the model assumed is incorrect. A better description of the experimental data is provided assuming an incoherent sum of scattering from the domains (see figure 6.6(a)). However, far from describing the strong asymmetry observed in the CTR, accounting for the scattering from domains appears to make the profiles more symmetric around the Bragg position (cf. for example figure 6.6(a) and figure 6.2). Therefore, another explanation is needed to describe the CTR results.

6.3 Modeling the asymmetry of the CTRs

After establishing the way in which the domains contribute to the measured intensity, next step is identify the origin of the asymmetry in the intensity along the CTRs. It is important to recall the difference between a CTR produced by an ideal mono-layer and a CTR produced by the surface of a crystal. In the first instance, the CTR is a uniform line of intensity in the reciprocal space. In the second case, the CTR is characterised by a modulation of the intensity due to the presence of the crystal Bragg peaks. Moreover, any inhomogeneities within the crystalline lattice, with a component along the surface normal direction, will be reflected in the CTR. Therefore, one possible explanation for the asymmetry in the CTRs could be the

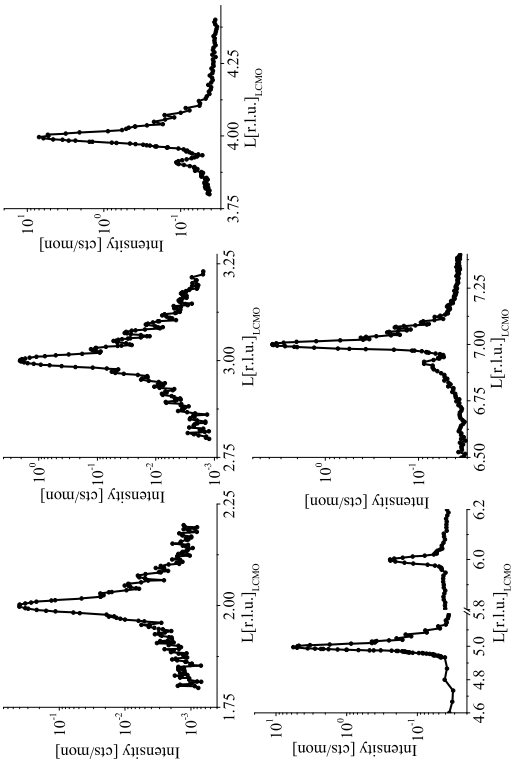

Figure 6.7: Measured [2 3] CTR on the 400Å LCMO film

presence of inhomogeneities in the crystal structure of the film along the surface-normal direction[105, 100]. The origin of such inhomogeneity can be chemical, like the surface confinement of one species in an alloy[100], or merely structural, as relaxation of strain and a smooth change in the lattice parameter[105] for epitaxial metallic films.

In our case, the most probable cause of the CTR asymmetry is of structural origin, although, as it will be shown later in this work, the possibility of chemical segregation effects might not be negligible. This hypothesis is based on the results already discussed in the previous chapter, i.e. the increased periodicity of the TD and the broadening of the domain size distribution. These can be interpreted as an increase of "disorder" toward the surface due to a relaxation of the epitaxial strain along the surface normal.

6.3.1 Variation of the c lattice parameter

The model we propose to explain the CTR data is a variation of the c lattice parameter in the film, due to the gradual relaxation of the elastic strain at the substrate-film interface.

The in-plane pseudocubic lattice parameter of the film (a_{pc}), as measured by GID, is constant in the whole film thickness. The XRD measurements do not show any evidence of relaxation of the in-plane lattice parameters of the film which always match those of STO. On the basis of the TDM model, we can think of the a_{pc} of LCMO as the projection of the a_o or b_o lattice parameters (elongated by the epitaxial strain) along the $< 100 >_c$ direction through the angle α (see figure 6.8). Consequently, any change in the a_o and b_o lattice parameters due to strain relaxation, has to be balanced with a change in α, in such a way a_{pc} stays constant. For these films the change in the c-lattice parameter, revealed by CTR measurements, has to be followed by a change of the a and b lattice parameters as well. However, our proposed model of TD distribution, as presented

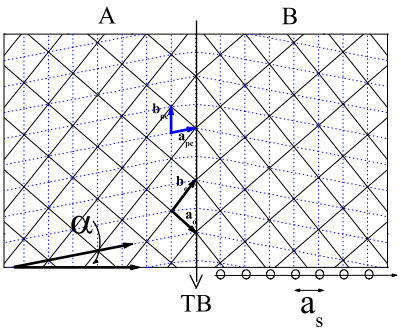

Figure 6.8: LCMO Twin domain matching STO substrate

in the previous chapter, is not enough "quantitative" to justify the introduction of such a complication as the variation of domain distribution *and* orthorhombicity at the same time. Finally, from what we learned from the model, we can suggest that the overall effect of slight variation of the parameter α would be a broadening of the side peaks, certainly non detectable within our approximation.

It is worthy to note that, due to the "phase problem", from the analysis of diffraction profiles one cannot discern a gradient at the interface with the substrate, from a gradient at the interface with the air. The rod we are going to analyse is a pure film-rod, i.e. there are no contribution from the substrate which, if present, would act as a phase reference and lift the degeneracy. Therefore, for the moment we will refer to a relaxation effect which happens at *one interface*, i.e. one of the two interfaces of the film without loss of generality. The problem of the phase reference can be overcome in the following way: modeling of the effect of the c-lattice gradient on the film-rod

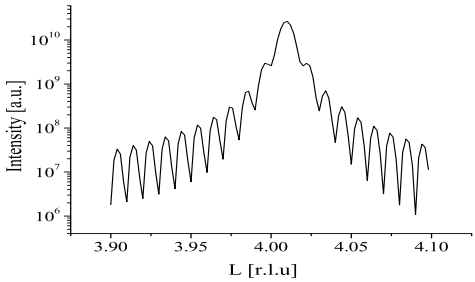

Figure 6.9: Example of scattering profile relative to a model of linear variation of the c-axis in a 400Å LCMO film

[3 2], and using the parameters to model the $[0\,0\,L]$ film + substrate rod, using the phase reference of the substrate to lift the degeneracy.

The program for the simulation of the CTRs intensity has been written with the code Mathematica. An easy way to model the system and evaluate the diffraction pattern is defining a functional form of the c-axis variation at the interface. Linear or quadratic variations do not reproduce well the data. For the sake of the completeness we show one example of scattering profile relative to a linear model in figure 6.9.

The choice of exponential variation of the c-lattice parameter, turns out to be the most appropriate. Also it is physically reasonable being associated to the phenomenon of "relaxation" of mechanical energy due to strain. One can express such variation in the following way:

$$c_j = c_0 + \Delta c \cdot e^{\frac{1-j}{\xi}} \qquad \text{for } j = 1 \ldots N_c \tag{6.4}$$

In the equation 6.4, c_j indicates the value of the lattice parameter c in the j^{th} u.c. c_0 is the maximum value that c reaches inside the film, N_c is the number of u.c. in the c-axis direction,

Δc is the maximum variation of the c-axis at the interface, and ξ the "decay" length of the exponential, i.e. the number of unit cells within which the relaxation occurs.

Calculating the CTRs of the LCMO film with an exponential variation of the c-lattice parameter, one immediately finds that this simple model accounts for the asymmetry of the intensity around the Bragg peaks. The shape of the diffraction profiles depends on the sign of the variation Δc. A decrease (increase) of c at the interface, i.e. $\Delta c < 0$ ($\Delta c > 0$) produces a higher (lower) intensity for low Q side of the Bragg peaks. The diffraction profiles produced by an increasing and a decreasing $c-$lattice parameter at the interface are plotted in figure 6.10.

However, from a close comparison between the scattering profiles calculated and the experimental data, it is clear that the model proposed does not explain very well the features of the measured profiles.

The asymmetry of the calculated profiles manifests itself mainly with an increase of the intensity of the Laue oscillation at the high Q side of the Bragg peak. These effects become more marked for higher momentum transfer. On the other hand the measured peaks are characterized by a rapid decrease of intensity on the low Q side of the Bragg peaks, which seems to be due to a strong interference effect.

6.3.2 A more complete model

A model which produces a diffraction profile with a better match to the experimental data consists in an exponential variation of c at both interfaces, with a short decay length ξ of the order of just few u.c. The functional form of the c-axis in the j^{th} layer is given by the following formula:

$$c_j = c_0 + \Delta c_1 \cdot e^{\frac{1-j}{\xi_1}} + \Delta c_2 \cdot e^{\frac{j-N_c}{\xi_2}} \qquad \text{for } j = 1 \ldots N_c \quad (6.5)$$

This expression is similar to the one in eq.6.4, with the presence of two more parameters, Δc_2 and ξ_2, representing respectively

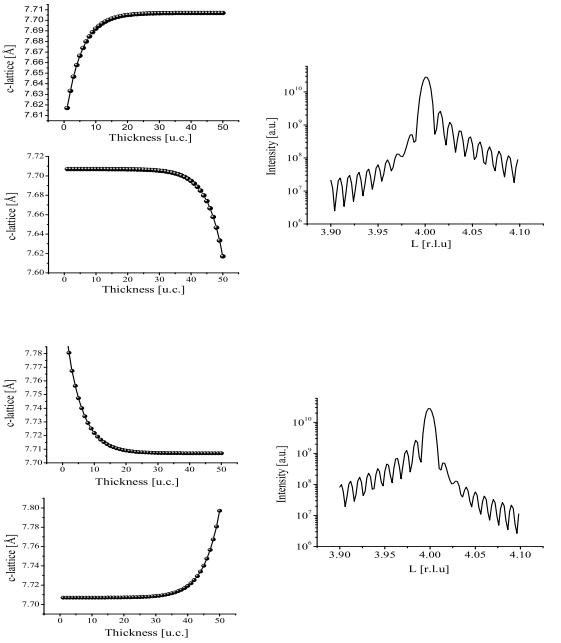

Figure 6.10: C-axis variation and scattering profile for $\Delta c < 0$ (upper figure) and $\Delta c > 0$ (lower figure)

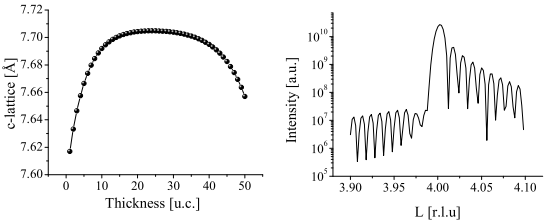

Figure 6.11: Exponential variation of the c-axis at both interfaces and relative scattering profile

amplitude and decay length of the variation of c at the second interface. The figure 6.11 shows the function 6.5.

The diffraction curves calculated on the basis of this model show a good agreement with the data -for a certain choice of the modeling parameters. In particular the asymmetry of the Laue oscillations arises from the interference between the two interface gradients. The choice of the parameters tunes the interference effect, generating different diffraction profiles. The interference effect can be so large that it suppresses the first few maxima of the Laue oscillations and enhances the following ones, as shown in figure 6.11. The variation of the c-lattice parameter strongly influences the position of the Bragg peaks in the reciprocal lattice, as one would expect. They no longer correspond to the c_0, which we can consider as the "relaxed" value of c, but instead to a weighted average value of c, depending on all the parameters in equation 6.5.

The above model describing a variation of the c-lattice parameters at the two interface, is supported by EELS measurement[107] shown in figure 6.12 which show a variation of Ca-content at the surface. It is well known that a variation of Ca concentration greatly affects the lattice parameters in LCMO[21, 22] and this

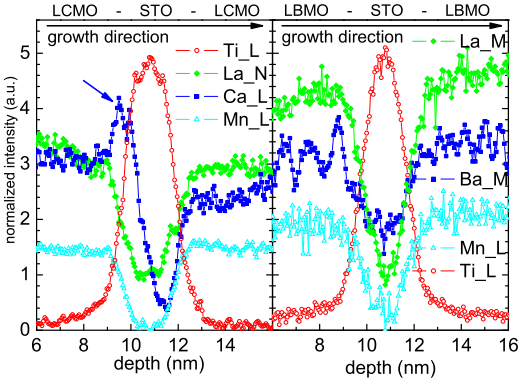

Figure 6.12: EELS measurements -courtesy of L.Alff

would account for the reduction of the c lattice parameter toward the surface of the films. Therefore, a more complete model needs to take into account also the variation of the structure factor along the c-axis, which could probably give additional small effects which need to be evaluated. Nevertheless, the simple model described in this section agrees well with the data.

6.3.3 Fitting procedure and results

A fitting routine written with the Mathematica 4.1 code, used for the CTRs $[2.5\,0.5]_c$, converges for more than one set of parameters, indicating that the space of solutions does not have a well defined minimum. A better fit would require more CTRs data, which could help to find an unique solution. However, the area of the space of the solutions giving a good agreement with the data is quite narrow, and is centered around the values:

$$\Delta c_{1,2} \approx 0.07\text{Å}$$

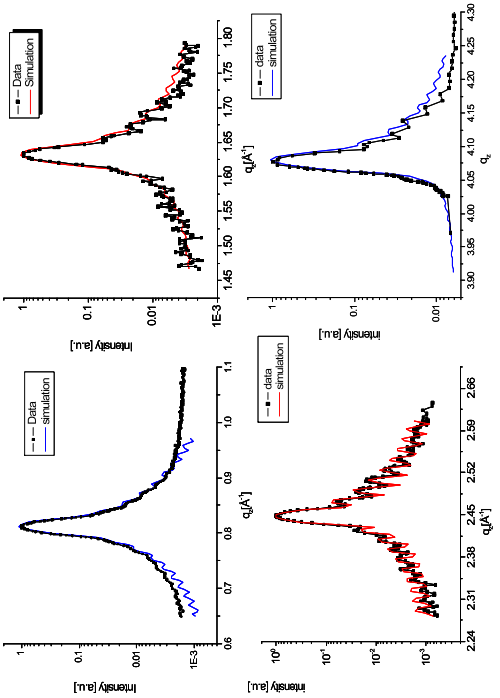

Figure 6.13: [2 3] CTRs of 400Å LCMO film. $L = 1, 2, 3, 4$ from top left. The experimental data and the fit obtained with the two-interfaces model are shown. The simulated curves have been convoluted with a function representing both the resolution of the instrument and the mosaicity of the sample.

$$\xi_{1,2} \approx 8 \text{ u.c.}$$

These parameters reproduce also very well the asymmetry of the [0 0] CTR. Moreover, due to the symmetry of the curve that describes the $c-$axis variation, as qualitatively found with our simulations, the procedure previously indicated (cf. page 151) as a possible solution of the *phase problem*, has not been implemented in this case.

Chapter 7

Polarised Neutron Reflectivity measurement

PNR measurements have been carried out on our samples in order to complete the study of the physical properties of thin LCMO films in presence of epitaxial strain. As discussed in chapter 3, PNR is a useful tool to probe the depth profile of the magnetisation $\vec{m}$ of a sample (with or without an external magnetic field H_{ext}). With an accurate measurement and analysis of all the curves R^{++}, R^{--}, R^{+-} and R^{-+} it is possible to get information about all the components of the vector $\vec{m}$, always averaged in the surface plane. It is clear that this method is not adequate to detect magnetic domains which are distributed in-plane but instead well suitable to detect changes of the magnetisation profile along the surface normal.

With PNR measurements a non-uniform magnetisation of the LCMO film has been detected, which will be discussed in the following.

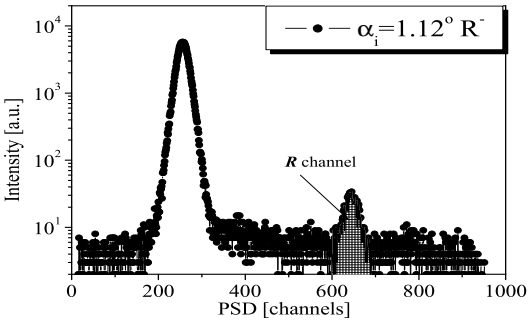

Figure 7.1: Intensity collected from the PSD during a neutron experiment. The angle of the incident neutron beam is $\alpha_i = 1.12^o$. In the channels 600–700 is the specular beam, while the transmitted beam in the channels 200–400. Background and diffuse scattering are also present

7.1 Measurement of PNR profiles

7.1.1 Experimental condition

The measurements have been carried out on the 400Å thick LCMO film, at a temperature $T = 10K$ in an external magnetic field $H_{ext} = 0.2$ Tesla applied either along the $< 100 >_c$ or the $< 110 >_c$ crystallographic axis of the film. The external magnetic field H_{ext} has been chosen to be higher than the coercive field $H_{coe} \approx 600Oe$[1] of the film and the temperature T well below the FM $T_C \approx 130K$. In this situation the magnetisation of the sample corresponds to about 50% of the its maximum value calculated at $\approx$ 6Tesla (cf. section 4.3).

The experiments have been performed at the reflectometer

[1]The coercive field of this sample has not been measured with the SQUID, but has been deduced on the basis of the dependence of the coercive field versus thickness of the series of samples measured

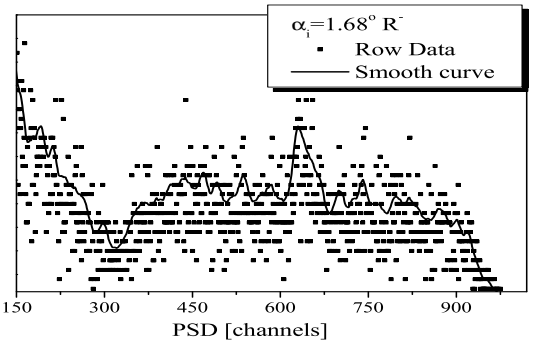

Figure 7.2: Intensity collected from the PSD at $\alpha_i = 1.68^o$. The data points (circles) have been convoluted with a square function (10 channels of PSD),to have a smoother signal (solid line). This kind of convolution has been used to verify that the specular can be separated from the diffuse scattering up to $\alpha_i = 2.6^o$.

EVA @ ILL in Grenoble. A detailed description of the instrument and the experimental setup can be found in section 3.6.2. An important parameter for the experiment is the polarisation of the incident beam, defined as

$$\frac{R^{++} - R^{+-}}{R^{++}}$$

measured on the incident beam. The value found for the polarisation factor is 97% ($\pm 0.5\%$).

The curves R^+ and R^-, with no polarisation analysis, have been measured in the experimental conditions of temperature and magnetic field described before. For completeness, measurements of reflectivity curves with polarisation analysis have also been performed, which have not provided any additional information. The measured profiles R^{++} and R^{--} do not dif-

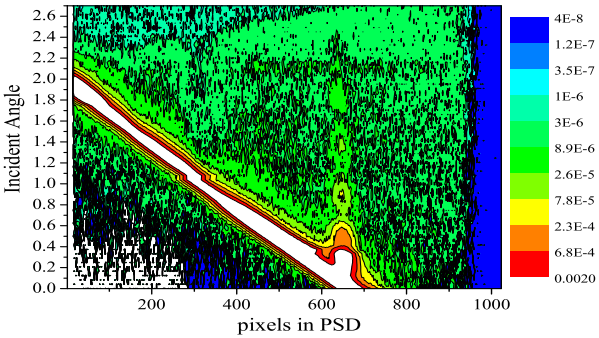

Figure 7.3: Map of the intensity of specular and non-specular scattering in a PNR measurement. The specular beam is always in the channels 600–700 (i.e. R), while the transmitted beam moves in different channels, until it does not hit the PSD anymore (for $\alpha_i > 2^o$). The increase of the background intensity at this angular value is an artifact of the PSD

fer respectively from the profiles R^+ and R^-. From this result one can conclude that the component of the magnetisation $\vec{m}$ transversal to the H_{ext} (cfr. Chapter4) is zero or produces a signal which is too low to be detectable.

7.1.2 Data treatment

The experimental data collected from the PSD detector during a PNR measurement have the form shown in figure 7.1. In this figure the intensity of both the transmitted and the specular beam is plotted versus their position on the PSD, for a fixed value of the incident angle $\alpha_i = 1.12^o$. During the measurements the PSD is moved in such a way the specular beam stays always in the same position on the detector (the filled area in the figure 7.1). From the data collected at different values of

the incident angle, it is possible to build up a map of the measured intensity on each channel on the PSD versus the incident angle α_i (cf figure 7.3). In this way not only the specular intensity is measured, but also the non-specular scattering, which can give important information about the in-plane (magnetic) structure of the sample. In figure 7.2, the PSD signal relative to $\alpha_i = 1.68^o$ is shown. The specular signal can be separated from the diffuse scattering, even if the two signals have a comparable intensity.

As pointed out before, the reflected signal will always be in the same group of channels, for simplicity defined as channel R. To extract the pure reflected scattering contribution from the data collected by the PSD, and create a reflectivity curve, the integrated intensity in the channel R is plotted with respect to the incident angle α. It is important to notice that this signal contains both the reflected beam and the background, which has to be subtracted properly. One way to make the background correction, is to measure the integrated intensity in a different channel, far from the reflected and transmitted beam, and subtract it from the integrated intensity of the channel R. In this way the background is overestimated, due to the fact that a diffuse intensity slightly above the background level is observed in our measurements. A second possibility to evaluate the background is to measure the asymptotic value of the integrated intensity of the R channel for high angular values. This value can be subtracted from the specular intensity. Both approaches have been used, with very similar results. This is probably due to the fact that the observed off-specular diffuse intensity (green area in figure 7.3) is very close to the background level.

The reflectivity curves obtained with the procedure described have been analysed to extract information about the magnetisation profile of the sample. Such analysis has been performed via the comparison of the measured curves with simulated PNR profiles, using as a parameter the average magnetisation per layer. The simulations have been performed with the program

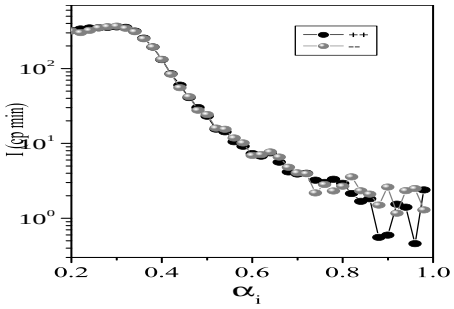

Figure 7.4: PNR profiles with $H_{ext} = 0$. The small contrast between the LCMO and STO does not make the Kiessig fringes to appear clearly

Winfit[93].

7.1.3 Reflectivity profiles

PNR profiles measured for an non-magnetised sample as well as with an unpolarised neutron beam, do not show the Kiessig fringes typical of samples of finite thickness (see figure 7.4). This is due to the fact that the "contrast" between the film and the substrate has a purely magnetic origin. On the other hand, in presence of a non-zero magnetisation vector of the sample the contrast between STO and LCMO becomes evident and clear Kiessig fringes appear on the reflectivity profile.

In figure 7.5 both the R^+ and R^- curves measured with the external magnetic field H_{ext} applied parallel to the $< 100 >_c$ crystallographic direction are shown. Similar measurements have been also performed with the external field applied along the crystallographic direction $< 1\bar{1}0 >_c$. The fact that the curves measured do not differ from the case $H_{ext} // < 100 >_c$ and that the results are invariant under rotation of the sample around

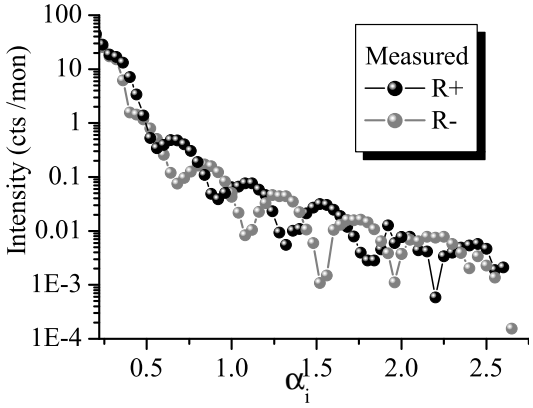

Figure 7.5: PNR profiles with $H_{ext} = 0.2T // < 100 >_c$

the surface normal, indicates the absence of a strong in-plane anisotropy in the magnetisation properties of the samples.

7.2 Model of the magnetisation profile of the LCMO film

7.2.1 Uniformly magnetised FM layer

The first simulation of PNR curves is based on a model of a FM film uniformly magnetised, with a magnetisation vector $\vec{m} = 3.7\mu_B$ per Mn-atom and aligned to the external magnetic field, which corresponds to a fully magnetised sample. The results of such simulation are shown in figure 7.6, and are useful for a qualitative comparison with the experimental data.

The PNR curves of a uniformly magnetised film show a very peculiar characteristic: the curves R^+ and R^-, each characterised by a certain critical angle $\alpha_c^{\pm}$ and whose difference

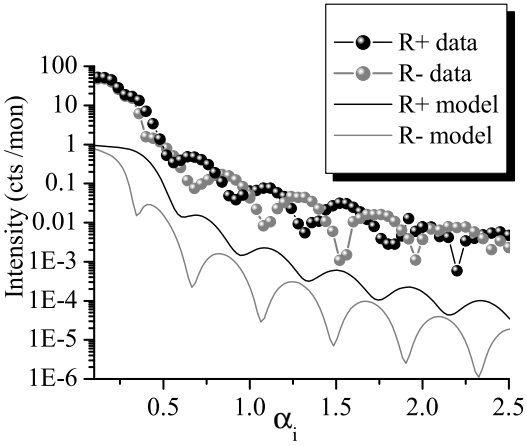

Figure 7.6: Comparison between data and simulated R^+ and R^- curves for a 400Å sample with uniform magnetisation $\vec{m} = 3.7\mu_B // < 100 >_c$ in a field $H_{ext} // < 100 >_c$.

$\Delta\alpha = \alpha_c^+ - \alpha_c^- \neq 0$ for $B \neq 0$, never intersect each other. This is easy to understand if one looks at the form of the interaction potential U(z) which we report in the following

$$U(z) = U_n(z) + U_m(z) = \frac{\hbar^2}{2m} N(z) b(z) + \vec{B} \cdot \vec{s}$$

The difference between R^+ and R^- clearly depends on the sign of the spin of the incident neutrons $\vec{s}$. Due to the small difference in the nuclear density between STO and LCMO discussed before, the "contrast" between the two materials (and consequently the Kiessig fringes) is due mainly to the term $\vec{B} \cdot \vec{s} = \pm B\mu$. If for a fully magnetised sample the curves R^+ and R^- do not intersect in any point, when the contrast becomes smaller, for example due to a smaller value of B, the quantity $\Delta\alpha$ will become smaller, but at the same time the intensity os-

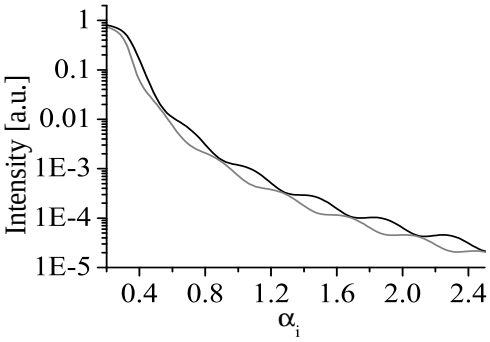

Figure 7.7: Simulation: R^+ and R^- curves for a 400Å sample with uniform magnetisation smaller than the ideal value. The curves become smoother than for the ideal case (figure 7.6) and the critical angle difference become smaller, but the curves never intersect.

cillations will become smoother, such that an intersection will never occur, for any value of B (cfr. figure 7.7).

From the analysis of the data, on the other hand, we clearly see that the characteristics of the measured curves is a small value of $\Delta\alpha$ and the intersection of the two curves R^+ and R^-, while the oscillations are still quite well marked. The small value of $\Delta\alpha$ is sign that at the surface the magnetisation is quite small, while the deep oscillations are sign of a quite strong contrast, of magnetic nature, at the interface with the substrate.

These consideration, together with the results of the SQUID measurements, reported in Chapter 5, converge toward a different model of the magnetic profile of these films.

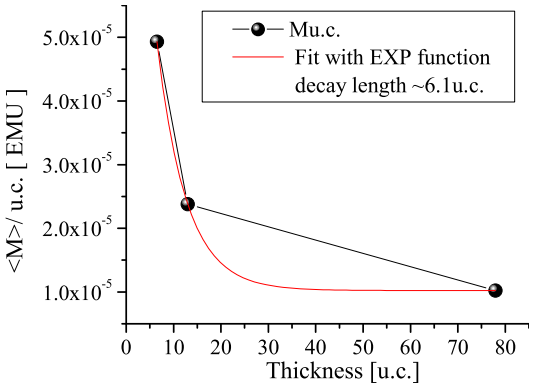

Figure 7.8: Average magnetisation (in EMU) measuread with SQUID, for a series of films of LCMO with thickness in the range of 50–600Å. The fit is an exponential function, which decays over a length $t \approx 6.13$u.c.

7.2.2 Gradient in the magnetisation of the LCMO film

The model proposed for the LCMO film is strongly supported by the results of the SQUID measurements performed on a series of samples with different thickness. As already discussed on Chapter 5, these measurements indicate that the average magnetisation $< m >$ of the sample decreases with increasing thickness following an exponential law.

The film can be thought as made of several layers each with different magnetisation. The magnetisation in each layer can be evaluated on the basis of the variation of $< m >$ described in the curve of figure 7.8, formally expressed in the following way:

$$< m >_j = m_0 - \Delta m \cdot e^{\frac{1-j}{\zeta}} \qquad \text{for j} = 1,\ldots \text{N} \tag{7.1}$$

which coincides with the exponential curve in figure 7.8.

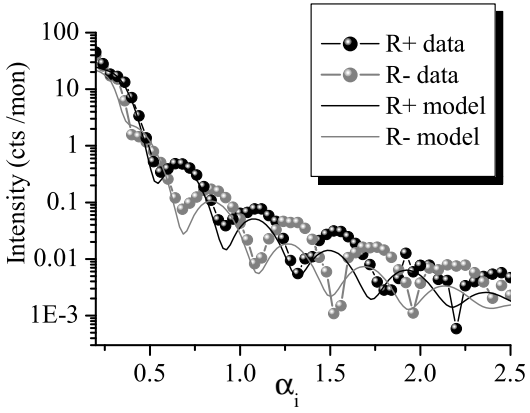

Figure 7.9: R^+ and R^- curves calculated for a LCMO film with a magnetisation profile decaying exponentially from the film-substrate interface, to the film surface. See the text

7.3 Results

The PNR curves calculated for this model are shown in figure 7.9. The model used is a stack of $N = 6$ layers the thickness of each layer being $t_j = 62$Å. The value of the parameters of equation 7.1 are the following:

$$\begin{aligned} m_0 &= 0.76\mu_B \\ \Delta m &= 2.93\mu_B \\ \zeta = 0.76[layers] &\approx 6\text{u.c.} \end{aligned}$$

This simple model seems to agree quite well with the experimental data. It is important to stress that the curves shown in figure 7.9 are not the results of a fitting procedure but are based on a model. Such model of exponential variation of the magnetisation vector has been deduced from the comparison be-

tween results of SQUID and CTRs measurements presented in Chapter 5 and 8.

The agreement between modeled and measured data, and the correspondence of the models and the parameters used, suggests a close connection between the structural and magnetic properties. The c-axis variation, the broadening of TD modulation and the decrease of the average layer magnetisation toward the surface seem to be different aspects of a unique trend. All these quantities vary with exponential law with a comparable decaying length. This suggests that an increased structural (or better morphological) disorder can be the cause of the decreasing of the magnetisation of epitaxially strained films. A similar model has been already proposed by Aarts et *al.* [APL, 72 (1998) p.2975]

7.3.1 Interface layers

A model to explain the influence of strain on the magnetic properties of thin manganite films has been proposed by F. Ott et al, in a work published on JMMM, based on the interpretation of PNR measurements performed out on similar films[110]. The proposed model consists in three regions in the film: two strained layers with reduced magnetisation at both the film-substrate interface and the surface, and a *relaxed* central region characterised by bulk-like value of the magnetisation. The curves calculated on the basis of this model seem to agree very well with their experimental data. However, the range of the momentum transfer explored allows to probe a minimum thickness of ≈ 20Å, while the model considers an interfacial layer of ≈ 10Å.

For the sake of the completeness we have tried to apply the same model for our films with unsatisfying results. The curves are shown in figure 7.10.

It is worthy to note that, in our case, due to the maximum momentum transfer for which the intensity of the signal is still

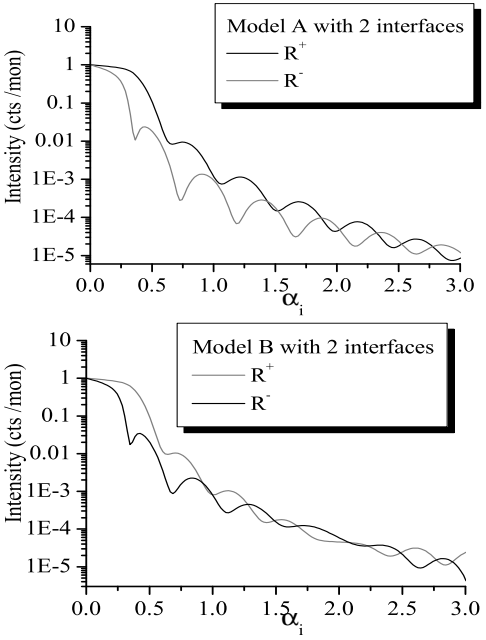

Figure 7.10: R^+ and R^- curves calculated for a model with magnetic profile characterised by a central part with 'bulk' magnetisation ($< m >= 3.7\mu_B$) and and two interface layers with lower magnetisation, ($< m >= 1.5\mu_B$). The two plots correspond to models with interfacial thickness of respectively 20Å the first (Model A) and 40Å the second (Model B).

above the background signal, the minimum thickness that can be probed is not lower than 60Å. On the basis of our simulations there is no sign of a layer of such thickness at the interfaces and proposing an interfacial layer of a smaller thickness would not make sense, because could not be directly probed. Moreover, as is clearly seen in figure 7.10, on the basis of our simulations

even the presence of a thinner layer at the interface, although if not directly detectable, would not be sufficient to reproduce the experimental data in the range of Q explored. A gradient is always needed to explain the major features of the measured curves.

7.4 Conclusions

To conclude, our measurements are not capable to exclude, neither to probe, the presence of a layer (thinner than 60Å) at the interface, but give a strong indication of the existence of a gradient in $< m >$, also strongly supported by the results of the SQUID measurements.

The agreement between modeled and measured data, and the correspondence of the models and the parameters used, suggests a close connection between the structural and magnetic properties. The c-axis variation, the broadening of TD modulation and the decrease of the average layer magnetisation toward the surface seem to be different aspects of a unique trend. All these quantities vary with exponential law with a comparable decaying length. This suggests that an increased structural (or better morphological) disorder can be the cause of the decreasing of the magnetisation of epitaxially strained films. A similar model has been already proposed by Aarts et *al*[72].

Conclusions

Structural and magnetic investigation have been performed on strained thin films of $La_{1-x}Ca_xMnO_3$ with $x \approx 1/3$ (LCMO) epitaxially grown on $SrTiO_3$.

It has been found that the energy balance between the formation of twin domains and the pseudomorphic growth, induced by the substrate, leads to the formation of a structural modulation. This modulation consists in a periodic arrangement of twin domains, and is the result of the competition between induced epitaxy and internal energy balance. This TDM has been found to be thickness dependent. From a comparison between the TDM for two different film thicknesses, a mechanism of relieving the strain is observed, which consists in the broadening of the domain size distribution, i.e. a gradual increase of "structural" disorder (of the domain distribution) towards the surface of the sample.

In order to understand if the mechanism of formation of TDM starts already at the film-substrate interface or if it develops from a certain thickness, it would be useful to investigate the structure of very thin films (of the order of few unit cells). Nevertheless, XRD measurements performed on these samples have not shown any evidence of a buffer layer with a different structure at the substrate-film interface, contrarily to what has been found from different authors on similar samples, where a strongly distorted layer is detected at the first stage of the growth. However, one could imagine that the epitaxial

strain and pseudomorphic growth could induce strong structural modification on very thin layers of material. This would not exclude the possibility, for the investigated samples, of a continuous modification of the structure during the growth of the successive layers. This is plausible if one takes into account that the temperature of the growth is high enough to allow atomic mobility.

In very thin films of LCMO, assuming a substrate-induced cubic symmetry, a total insulating behaviour is expected. This hypothesis is corroborated by the results of the temperature dependence of the structural modulation, which indicates a decrease of the modulation amplitude of a factor a two. On the basis of the proposed model, the disappearance of the SL peaks is related to an increase of the crystal symmetry of the system, i.e. the reduction to zero of the tilting angle α, related to the orthorhombicity of the film. The suppression of the metallic behaviour in the FM phase in very thin films (epitaxially strained) could be associated to a structural change, from the orthorhombic to the cubic symmetry. In this case one would expect a complete insulating behaviour in case of strongly distorted layers, e.g. pseudomorphic thin layers with cubic symmetry. However, there is no clear signature of a complete phase transition in the films investigated.

Clear indication of a structural phase transition have been found, within a different PhD work (Ulrich Gebhardt) in LSMO thin films. The observed structural phase transition is proven by the disappearance of the out-ofplane SL peaks (related to the triclinic phase) and the appearance of Bragg peaks relative to a orthorhombic symmetry. This phase transition is, in this case, related to the metallic-to-insulating transition, and paramagnetic-to–ferromagnetic transition.

For the LCMO thin film studied in this work, the magnetic properties show a clearer relation with the structural properties. The observed broadening of the size distribution of the TD with

increasing thickness is a sign of the increasing "structural" disorder (although the coherence of both the film structure and the in-plane modulation is not destroyed). SQUID measurements and PNR profiles give a clear indication of an exponential decrease of the average magnetisation per layer for the investigated samples. This variation is attributed to an increase of disorder in the magnetic domains, which could be related to the increase of disorder in the crystallographic domains, as deduced by the application of the TDM model. Moreover, this decrease is related to the variation of the c-lattice in the direction of the growth, as detected by CTR measurements, which follows an exponential decay, with decay length of $\approx$ 6u.c., in very good agreement with the magnetisation results.

PNR measurements are sensitive to the magnetisation profile along the surface-normal, but do not allow to probe the in-plane distribution of domains in the sample. For this reason it is impossible to relate the size of magnetic domains with the size of the crystallographic one. It is possible to measure the size of the magnetic domains with the Magnetic Force Microscopy (MFM) technique. However, this technique is only surface-sensitive, and allows the observation of magnetic domains on the surface of the sample. Moreover, it is a *local* technique, and a *statistical* characterisation of the sample would require a large surface sampling.

Finally, for a better understanding of the role of the structural and chemical parameters, and in particular the crystal symmetry and the doping of the sample, on magnetism and transport properties it is advisable to extend the structural studies to very thin samples (few unit cell thick) as well as to similar films deposited on different substrate (e.g. compressive strain). Moreover, to understand the origin of the variation of the c-lattice parameter in the film studied, the variation of the Ca concentration has to be taken into account, as well as the presence of the substrate for a phase assignement.

Summary

1. Motivation

Mixed valence manganites with perovskite structure, with general formula $A_{1-x}B_xMnO_3$ have been widely studied in the past 50 years because of their interesting and complex physics as demonstrated by their rich phase diagram[1]. Changing the dopant concentration x allows the formation of diverse phases, which change from insulating antiferromagnetic, to ferromagnetic metallic, passing through charge and orbital ordered regions. The variety of physical behaviour achievable via this chemical substitution (rare earth for alkali cations) makes these compounds an interesting subject of study, due to the possibility of tuning physical properties by the controlled variation of only one parameter, i.e. x. Recently, the discovery of phenomena of Colossal Magneto Resistance (CMR) and dense granular magneto-resistance in ferromagnetic thin films (corresponding to the doping $x \approx 1/3$) has renewed the interest towards them, as materials suitable for applications in electronic devices.

Considerable efforts have been recently addressed to the fabrication of high quality crystalline films. The expertise achieved in the fabrication of thin oxide films in the last few years, especially due to the large interest in fabrication of high temperature superconductors (HTSC), has been an advantage for the fabrication of high quality manganite films. Techniques such as sputtering, molecular beam epitaxy (MBE) or pulsed laser deposition (PLD) have been applied to the fabrication of manganites, to allow the fabrication of crystalline systems devoid of defects and more suitable for applications.

The use of thin films has introduced a new and interesting field of study, via the role of the strain induced by the substrate onto the transport and magnetic properties of the materials. Most interestingly, the presence of external strain (due to the epitaxy) introduces new physical behaviours, not yet completely understood, which have been for long time at the center of a very intensive research. Several works have been addressed to the study of the modification of physical properties introduced by epitaxial strain[8]. However, the complicated interplay between structure, magnetism and transport properties in manganites is still an open field, and the present work enters this framework as a contribution to the understanding of this fascinating topic.

This work focuses on $La_{1-x}Ca_xMnO_3$ in the $x = 1/3$ phase, hereafter referred to as LCMO. LCMO is ferromagnetic metallic below its Curie temperature which, for bulk systems, is $T_C \approx 280K$, and presents the phenomenon of CMR. One of the effects widely observed in thin LCMO films is the reduction of the Curie temperature and the appearance of a ferromagnetic *insulating* behaviour, instead of the metallic one of the bulk[10].

The main scope of this thesis has been the accurate structural and magnetic study of strained thin films of LCMO epitaxially grown on $SrTiO_3$ substrate (STO). Due to the mismatch between the crystal lattice of the two compounds, mechanical strain is imposed to the film structure, which can be responsible for changes of the physical properties of the material. Bulk LCMO has an orthorhombic structure with $a = 5.47$Å, $b = 5.49$Å, $c = 7.74$Å. However, the use of *pseudo-cubic* (pc) lattice parameters is very common for perovskite-like structures, and for LMCO is $a_{pc} = 3.87$Å[2]. The structure of the substrate STO, on the other hand, is cubic with lattice parameter $a = 3.905$Å, and for epitaxial LCMO films on STO the vector $\vec{a}_{pc}$ of LCMO is directed along the $< 100 >_{STO}$ crystallographic axis. In this case the mismatch between the two structures is

[2]The pseudo-cubic lattice parameter and the orthorhombic one are rotated with respect to each other by 45^o

$\delta \approx 1\%$, and the films is under *tensile* strain.

The epitaxial growth of a film on a substrate can induce a matching of the in-plane lattice parameters of the film with the ones of the substrate at the interface between the two compounds (in this case LCMO and STO). When this is not already the case for the bulk relaxed structures (i.e. in presence of a mismatch $\delta \neq 0$) we are in presence of *pseudomorphic growth*, and the strain imposed by the substrate acts on the film structure as a modifying agent. The pseudomorphic growth is then the result of an energy balance between the tendency of the crystal lattice to grow relaxed, following internal energy balance, and the external pressure of the substrate acting as a template structure. The epitaxial growth of a film in presence of a mismatch may lead, consequently, to structural distortions, which arise from the mechanical response of the crystal lattice to the presence of the substrate, as a mechanism to relieve the epitaxial strain. This response might vary from case to case, depending on the value of mismatch as well as on the nature of the atomic bondings and consequently on the *rigidity* of the lattice. The strain-induced lattice distortions can be localised or modulated on several unit cells, and directly influence those physical properties which are related to the lattice structure. For this reason an accurate study of the crystal structure of a strained material is an important step toward the understanding of the modification of physical properties in presence of strain.

2. Experimental

The main interest of this research project is the accurate analysis of the strain-induced modifications to the structure of LCMO epitaxial thin films and their effect on magnetic and transport properties. The films studied, with thickness in the range 50Å-600Å, have been grown by Pulsed Laser Ablation by Dr. J.Klein, at the University of Cologne - Germany.

The films are ferromagnetic and present the CMR effect. Their T_C, of the order of $\approx 130K$, is strongly suppressed with respect to the bulk value ($T_C \approx 280K$), and does not show any thickness dependence. i.e. there is no evidence of a relaxation towards the bulk up to the highest thickness measured. Structural analysis on these films have been performed with x-ray diffraction (XRD) using synchrotron radiation, to investigate the interconnection between the structure and their magnetic properties.

XRD technique is a non-destructive technique which allows an accurate structural study of the films. It has been adopted in this work with particular attention to the evaluation of the epitaxial relationships between film and substrate, to detect eventual strain-induced distortions, modification of the crystal symmetry and, more generally, the study of the mechanisms adopted by the film to relieve the strain. The reason for using synchrotron radiation is that the signals arising from strain-induced distortions are expected to be very weak compared with Bragg scattering (3–4 orders of magnitude smaller), impossible to detect with conventional sources. The measurements have been carried out mainly at the beamline BM28 (XMaS, UK CRG) at the ESRF (European Synchrotron Radiation Facility) in Grenoble -France, and at the MPI Surface Scattering Beamline at ANKA in Karlsruhe - Germany.

The use of Grazing Incidence Diffraction (GID) and Crystal Truncation Rod (CTR) measurements, have provided a complete picture of the structural properties of these films. In particular, the use of GID for the study of the in-plane structure of the films has allowed the observation of a particular microstructure of the films. Such microstructure consists of twin domains (TD) of similar size periodically arranged in the plane of the growth. The twinning axis is $< 110 >_{ortho}$.

We claim that such twin domain modulation (TDM) is the structural response of the film to the strain induced by the substrate. The formation of twin domains occurs very often in

perovskite crystals, being a mechanism with low cost in energy. In this special case of epitaxial growth, the TDM creates an *average* structure which helps reducing the mismatch between film and substrate. Consequently it enters considerably in the energy balance of the growth process, as a strain-relief mechanism energetically favorable if compared with unit cell distortion, or variation of inter-atomic distances.

The signature of this periodic microstructure, in the GID measured profiles, is the presence of broad superlattice (SL) peaks around in-plane Bragg peaks of the type $[H\,K\,0]$. These peaks are characterised by a very weak intensity if compared with Bragg reflections ($\approx$ 3 orders of magnitude less). For $[H\,0\,0]$- and $[0\,K\,0]$-type Bragg peaks, two SL peaks are found at a distance $\pm\vec{q}$ from the central peak, in direction perpendicular to the scattering vector. For $[H\,K\,0]$-type peaks, instead, 4 SL peaks are found, with wave vector $\vec{q}$ directed along the $< 100 >_c$ and $< 010 >_c$ crystallographic directions. These SL peaks indicate the presence of a one-dimensional structural modulation, i.e. a periodicity in the structure of the film, with components in the plane of the growth $a-b$, with characteristic length $\Lambda_0 = 2\pi/q$. No SL peaks have been found around purely *out-of-plane* peaks for thin films (100Å). For thicker films, instead, a broad peak has been observed together with the sharp Bragg component of $[0\,0\,L]$-type peaks. Such broad component can also be ascribed to a poorly correlated *out-of-plane* periodicity.

3. Model

In our proposed model, the size of the twin domains is statistically distributed around an average value L_0 with a standard deviation ΔL_0. L_0 represents the periodicity of the twin domain modulation, even if it is related to the wavelength of the modulation Λ_0 in a non trivial way. The parameters of our model

are only two. The first is the tilt angle (α) of the pseudo-cubic lattice between two twin domains. In our model α is related to the orthorhombicity factor a_o/b_o of the film by the relation $\alpha = 90^o - 2arctan(a_o/b_o)$. For bulk LCMO it is $\alpha_{bulk} = 0.31^o$. This value may be strongly modified in the films by the presence of epitaxial strain. For this reason, in our model, α is treated as a variable. The second parameter is the maximum number of unit cells allowed in a domain. This is a phenomenological parameter related to the internal mechanical energy of the system, also treated as a variable. A more detailed description of the model is found in the PhD thesis of U. Gebhardt, who has developed the model and the program for the simulation of the scattering profiles. This simplified model, which does not take into account the structure factor of the unit cell, reproduces surprisingly well the experimental diffraction profiles. On the basis of these results, we claim that our model is widely applicable to all the systems which allow the formation of twins, and can be thought as one of the possible strain relaxation mechanisms of perovskite films.

4. Results

4.1 *In-plane*

As a result of the application of this model, for the 100Å film we have found an *in-plane* distribution of twin domains, with an average domain size of $L_O = 32$u.c. and a distribution width of $\Delta L_0 = 16$ u.c. The tilt angle α found from the simulations is $\alpha = 0.06^o$, which corresponds to an orthorhombicity factor $a_o/b_o = 0.9991 \approx 1$, with *in-plane* lattice parameters larger than the bulk. This can be justified from the competition between the tendency to the formation of TD and the epitaxial growth. The energy balance tends to favor the formation of

TD's, while the epitaxial relationships force the matching of the in-plane lattice parameters of LCMO with STO. The resulting atomic configuration consists in a periodic arrangement of TD of LCMO with an enlarged lattice parameter.

For higher thickness, as for the 400Å film, a satisfactory modeling of the measured scattering profiles has been achieved considering the structure as made of 3 different *in-plane* TD distributions. These distributions are characterised by the following average and deviation: $L_{01} = 32$u.c. and $\Delta L_{01} = 14$u.c, $L_{02} = 64$u.c and $\Delta L_{02} = 24$u.c, $L_{03} = 79$u.c and $\Delta L_{03} = 49$u.c. This can be justified with a model of increased disorder in the domain distribution in the direction of the growth. As the thickness of the film increases, the distribution of domains becomes more and more disordered, as results of a process of *strain-relaxation*. Even though, the strain induced by the substrate is not relieved completely, and the structural properties of the films do not become the ones of the bulk relaxed system. The tilt angle for the 3 distributions is the same as the one found for the thin films, i.e. $\alpha = 0.06^o$, although a change (and in particular an increase towards bulk value) is expected from the process of *relaxation* of the structure. Simulations of scattering profiles from *in-plane* TD distributions characterised by different tilt angles, and same value of L_0 and ΔL_0, show that the variation of α alone is not enough to reproduce the data. Furthermore, for a good agreement between simulated and measured profiles, the parameter α should not exceed the value of 0.07. Finally, due to the fact that the introduction of such small change does not introduce any further improvement of the simulation, and considering that at this level the model is still qualitative, in our simulations α has been kept constant at the value of $\alpha = 0.06$. On the basis of the previous discussion, we can argue that the variation of α in the distribution of domains along the c direction, does not exceed the 20%, i.e. the tilt angle stays always around 18–19% of the bulk value.

4.2 *Out-of-plane*

The presence of the broad peak found at $[0\,0\,L]$-type positions has been explained, within the same model, as due to an *out-of-plane* TD modulation. One of the possible origin of this modulation could be the presence of crystallographic domains with c-lattice in the plane of the growth. In this case, TD with twin axis $< 110 >_o$ normal to the surface could produce a similar periodicity in this direction. In this case the twinning correspons to a slight periodic buckling of the film on the top of the substrate. The small intensity and the large width of this broad component, would be an indication of a small population of these domains, and a poor correration of the modulation itself. The second possibility is a *monoclinic* distortion of the LCMO unit cell, which would account for the periodicity in both the *in-plane* and the *out-of-plane* directions. The confirmation of one of thesis hypothesis requires an accurate crystallographic analysis, which goes beyond the scope of this thesis.

4.3 Crystal Truncation Rod

CTR measurements confirm the presence, in thick films, of a form of *strain-relaxation* along the direction of the growth. A strong asymmetry has been observed in the intensity of Laue oscillations. It has been found to be due to to a variation of the c-spacing both at the surface of the films and at the substrate-film interface. The $c-$lattice parameter increases from the interface towards the center of the film, and decreases again at the surface. The variation at both interfaces follows an exponential law, with amplitude $\Delta c \approx 0.07$Å, and a decay length of ≈ 6 u.c. The variation of the $c-$lattice parameter at the two interfaces is ascribed to a *relaxation* of the mechanical strain induced by the substrate. This relaxation may also lead to a variation

in the Ca stoichiometry at the interfaces, as demonstrated by EELS measurements performed on samples grown in the same conditions[107]. It is well known that a variation of Ca concentration greatly affects the lattice parameters in LCMO[106] and this would account for the reduction of the c lattice parameter towards the surface of the films.

It is important to stress that, despite the observed variation of the c-lattice parameters towards the bulk value, and the model of increased disorder in the TD distribution in thick films, these films do not show evidence of a strong relaxation *towards the bulk*, both from the point of view of structural and magnetic properties. The epitaxial relation with the substrate persists for all the thickness investigated and, as shown by magnetic measurements, the T_C is similar for all the films, evidencing that the films can be considered *strained* up to the highest thickness investigated (600Å).

4.4 Magnetism

Magnetic measurements have been performed both with superconducting quantum interference device (SQUID) and polarised neutron reflectivity (PNR) techniques. These two techniques have been used in a complementary way. SQUID measurements, sensitive to average magnetic properties of the samples, have been used to measure the Curie temperature, the saturation magnetisation and the coercive fields of the samples, while PNR measurements have been used for the investigation of the magnetisation profile of the sample, to analyse the way in which the strain influences the magnetisation *distribution* in the film.

From SQUID measurements all the films have been found ferromagnetic with a suppression of the critical temperature. The T_C found is in the range 80–130K, without a strong thickness dependence, indication of the persistence of the strain up to highest value of thickness explored. Interesting results come

from the analysis of hysteresis curves. The magnetisation of the samples does not saturate completely up to the maximum value of external field applied $H = 6Tesla$. This effect can be ascribed either to a *canting* of the magnetic moments, or to the presence of magnetic domains. The last hypothesis, subject of recent publications[72, 108], is in good agreement with the results of our structural investigation. The magnetic domains could be related to the presence of crystallographic domains. A proof of this may be obtained using MFM magnetic force microscopy. The size of magnetic domains is expected to be comparable with the size of the crystallographic domains found by our model.

Furthermore, the value of the *saturation* magnetisation of the films, calculated at the maximum field measured (i.e. for $H = 6Tesla$) strongly decreases with increasing thickness of the samples, following an exponential law. The value estimated for the decay length is $\approx$ 6u.c. while the estimated variation of the average magnetisation is 80% within 600Å. These values are in a very good agreement with the CTR results, indicating a strong correation between structural *relaxation* and variation of magnetic properties.

The results of SQUID measurements have been confirmed by PNR measurements, performed at EVA@ILL (Grenoble - France). For one of the thick samples, 400Å, PNR give evidence of a strong gradient in the magnetic profile of the film, as expected from the SQUID results. The average magnetic moment found is maximum at the interface, with a value of $3\mu_B$, which decreases exponentially along the direction of the growth to reach a value as low as $0.7\mu_B$ at the film surface, in good agreement with SQUID measurements.

This peculiar magnetic properties, together with the model of change in distribution of twin domains and variation of c-axis, can be attributed to an increase of disorder in the domains, which reflects also in a disorder in magnetic domains. In this sense all the measurements converge in a model of epitaxial growth, achieved by twin domain periodicity, with a distribution

of domain sharper at the interface and broader at the surface, symptom of an increase of disorder in the distribution, which is followed by the magnetic profile as well.

Bibliography

[1] P. Schiffer, A. P. Ramirez, W. Bao and S.-W. Cheong, *Physical Review Letters* **75** 3336 (1995)

[2] S. Jin, T.H. Tiefel, M. McCormack, R.A. Fastnacht, R. Ramesh and L.C.Chen, *Science* **264** 413 (1994)

[3] S. Jin, T.H. Tiefel, M. McCormack, H.M O'Brian, L.H. Chen, R. Ramash and D. Shurig, *Applied Physics Letters* **67** 557 (1995)

[4] A. J.Millis, P. B. Littlewood and B. I. Shraiman, *Physical Review Letters* **74** 5144 (1995)

[5] C. Zener, *Physical Review* **81** 440 (1951)

[6] J.B. Goodenough, *Jounal of Applied Physics* **81** 5330 (1997)

[7] S. Uhlenbruck et *al. Physical Review Letters* **82** 185 (1999)

[8] J.N. Eckstein, I. Bozovic, D. G. Schlom, J.S. Harris, *Applied Physics Letters 57* 1049 (1990)

[9] J.N. Eckstein et *al.* J. Va. Sci. Technol. B **7** 319 (1989); T. Mazumoto et *al. Applied Physics Letters* **58** 2039 (1991)

[10] A. J. Millis, T. Darling, A. Migliori *Jounal of Applied Physics* **83** 1588 (1998)

[11] N.-C. Yeh, C.-C. Fu, J.Y.T. Wei, R.P. Vasques, J. Huynh, M. Maurer, G. Beach, D.A. Beam, *Journal of Applied Physics* **81** 5499 (1997)

[12] M. Rajesvari et *al. Applied Physics Letters* **73** 2672 (1998)

[13] N.K.Todd, N.D. Mathur and M.G. Blamire, *Journal of Applied Physics* **89** 6970 (2001)

[14] F.S. Razavi, G. Gross, H.-U. Habermeier, O. Lebedev, S. Amelinckx, G.van Tandeloo, A. Vigliante, *Applied Physics Letters* **76** 155(2000)

[15] J.M.D. Coey, M. Viret and S. von Molnár, *Advances in physics* **48** N.2 167 (1999)

[16] A.P. Ramirez J *ournal of Physics: Condensed Matter***9** 8171-8199 (1997)

[17] A.M. Glazer *Acta Crystallographica* **B28** 3384 (1972)

[18] A.M. Glazer *Acta Crystallographica* **A31** 756 (1975)

[19] P.M Woodward *Acta Crystallographica* **B53** 32-43 *and* 44–66 (1997)

[20] B. B. Van Aken, A. Meetsma, Y. Tomioka, Y. Tokura, T. T. M. Palstra *cond-mat/0206181* (11 jun 2002)

[21] P. G. Radaelli, M. Marezio, H. Y. Hwang, S.-W. Cehong and B. Batlogg, *Physical Review B* **54** 8992 (1996)

[22] P. G. Radaelli, D.E. CoxM. Marezio, S.-W. Cehong, P. Schiffer, A. P. Ramirez, *Physical Review Letters* **75** 4488 (1995)

[23] A.K.Heilman et *al. Physical Review B* **61** 8950 (2000)

[24] K.I.Kugel', B.I. Komskiĭ *Usp. Fiz. Nauk* **136** 6221–664 (1982)

[25] A. J. Millis, B.I.Schraiman an R. Muellerc *Physical Review Letters* **77** 175 (1996)

[26] R.P. Sharma, G.C. Xiong, C. Kwon, R. Ramesh, R. L. Greene, T. Venkatesan *Physical Review B* **54** 100014 (1996)

[27] Y. Murakamiet *al. Phys. Rev. Letters* **80** 1932 (1998)

[28] M. v Zimmermann, J. P. Hill, D. Gibbs, M. Blume, D. Casa, B. Keimer, Y. Murakami, Y. Tomioka and Y. Tokura, *Physical Review Letters* **83** 4872 (1999)

[29] M. Fabrizio, M. Altarelli, M. Benfatto *Physical Review Letters* **80** 3400 (1998)

[30] C.W.M. Castleton and M. Altarelli, *Physical Review B* **62** 1033 (2000)

[31] P.W. Anderson and W.C. Hasegawa, *Phisical Review* **7** 397 (1955)

[32] E. Nagaev, *Semimagnetic Semiconductors* (Mir: Moscow, 1983)

[33] E. L. Nagaev, *Physics Letters* **A239** 321 (1998)

[34] N. Ohata *J. Phys. Soc. Jpn.* **34** 343 (1973)

[35] K. Kubo and A. Ohata, *J. Phys. Soc. Jpn.* **33** 21 (1972)

[36] E.L. Nagaev *Physics- Uspekhi* **39** 781-805 (1996)

[37] A. J. Millis *Chapter 2 in "Colossal Magnetoresistive Oxides"* Edited by Y. Tokura (Gordon and Breach Science Publisher)

[38] M. Hamada, H. Sawada and K. Terakura, *J.Phys. Chem. Sol.* **56** 17 1755 (1995)

[39] W. Pickett and D.E. Singh, *Phys. Rev. B* **53** 1146 (1996)

[40] A. J.Millis, P. B. Littlewood and B. I. Shraiman, *Physical Review Letters* **74** 5144 (1995)

[41] A. Millis *Nature* **392** 147 (1998)

[42] L.Vasilui-Doloc et *al. Physical Review Letters* **83** 4393 (1999)

[43] L.Vasilui-Doloc et *al. Jounal of Applied Physics* **89** 6840 (2001)

[44] S. Shimomura, N. Wakabayashi, H. Kuwahara, Y. Tokura *Physical Review Letters* **83** 4389 (1999)

[45] S. Shimomura et *al. Physical Review B* **62** 3875 (2000)

[46] V. Kiryukhin, B. G. Kim, T. Katsufuji, J. P. Hill, S.-W. Cheong *Physical Review B* **63** 144406-1 (2001)

[47] Y. Yamada, O. Hino, S. Nohdo, R. Kanao *Physical Review Letters* **77** 904 (1996)

[48] M.C. Martin, G. Shirane, Y. Endoh, K, HIrota, Y. Moritomo and Y. Tokura *Physical Review B* **53** 14285 (1996)

[49] P. Dai et *al. Physical Review Letters* **85** 2553 (2000)

[50] C.P. Adams, J.W. Lynn, Y.M. Mukovskii, A.A. Arsenov, D.A. Shulyatev *Physical Review Letters* **85** 3954 (2000)

[51] R. Kajimoto, H. Yoshizawa, Y. Tomioka, Y. Tokura *Physical Review B* **63** 212407 (2001)

[52] Caignaert et *al. J. Magn. magnn Mater.* **154** L260 (1996)

[53] M. Uehara, S. Mori, C.H. Chen, S.W. Cheong *Nature* **399** 560 (1999)

[54] A. Moreo, M. Mayer, A. Feiguin, S. Yunoki, E. Dagotto *Physical Review Letters* **84** 5568 (2000)

[55] K. Dörr, J.M. De Teresa, K.-H. Müller, D. Eckert, T. Walter, E. VLakhov, K. Nenekov, L. Shultz *Journ Phys: Cond Matt* **12** 7099 (2000)

[56] P. Schiffer, A. P. Ramirez, W. Bao and S.-W. Cheong, *Physical Review Letters* **75** 3336 (1995)

[57] S.-W. Cheong and H. Y. Wang *Chap. 7 in "Colossal Magnetoresistive Oxides"* Edited by Y. Tokura (Gordon and Breach Science Publisher)

[58] N. Fujimura, D.T.Thomas, S.K.Streiffer, A.I.Kingon *Japanese Jounal of Applied Physics* **37** 5185 (1998)

[59] R. Gross et *al. Proc. SPIE int. Soc. Opt. Eng.* 4058 **278** (2000)

[60] D.J. Rogers, P. Bove and F.H. Teherani *Supercond. Sci. Technol.* **12V** R75-R85 (1999)

[61] P.R. Willmott and R. Huber *Reviews of Modern Physics* **72** 315 (2000)

[62] R. Woerdenweber *Supercond. Sci. Technol.* **12** R86–R102 (1999)

[63] H. Sato, M. Naito, T. Arima, Y. Tokura, *Applied Physics Letters* **61** 2470 (1992)

[64] H. W. Zandbergen, J. Jansen, S. Freisen, T. Nojima and J. Aarts, *Philosophical Magazine A* **80** 337 (2000)

[65] M. Salvato, private communication

[66] J.F. Mitchell, *Physical Review B* **54** 6172 (1996)

[67] A. Maignan, Solid State Comm, **101** 207 (1997)

[68] O. I. Lebedev, G. Van Tendeloo and S. Amelinckx, B. Leibold and H.-U. Habermeier, *Physical Review B* **58** 8065 1998

[69] O. I. Lebedev et *al. Philosophical Magazine A* **80** 673 (2000)

[70] P. Dai, J. Zhang, H.A. Mook, S.-H. Liou, P.A. Dowben, E.W. Plummer, *Physical Review B* **54** R3694 (1996)

[71] J.Klein, J.B.Phillip, G.Carbone, A.Vigliante, L.Alff and R.Gross *Physical Review B* **66** 052414 (2002)

[72] J. Aarts, S. Freisem, R. Hendrikx, H.W. Zandbergen, *Applied Physics Letters* **72** 2975 (1998).

[73] L. Ranno, A. Llobet, R. Tiron, E. Favre-Nicolin, *Applied Surface Science* **188** 170 (2002)

[74] R.B. Praus, B. Leibold, G.M. Gross, H.-U. Habermeier, *Applied Surface Science* **40** 138 (1999)

[75] M. Ziese, H. C. Semmelhack, K.H. Han, S.P. Sena, H.J. Blythe *Jounal of Applied Physics* **91** 9930 (2002)

[76] N.-C. Yeh et *al. Journal of Applied Physics* **81** 5499 (1997)

[77] N.-C. Yeh et *al. J. Phys.: Condens. Matter* **9** 3713 (1997)

[78] T.Y. Koo, S.H. Park, K.B. Lee, Y.H. Jeong *Applied Physics Letters* **71** 977 (1997)

[79] K.-K. Choi, T. Taniyama and Y Yamazaki *Jounal of Applied Physics* **90** 6145 (2001)

[80] J. O'Donnell, M.S. Rzchowski, J.N. Eckstein, I. Bozovic, *Applied Physics Letters* **72** 1775 (1998)

[81] M.C. Smoak et *al. Jounal of Applied Physics* **87** 6764 (2000)

[82] Y. Suzuki, H.Y. Hwang, S.W. Cheong, R.B. van DOver *Applied Physics Letters* **71** 140 (1997)

[83] A. Biswas, M. Rajeswari, R.C. Srivastava, Y.H. Li, T. Venkatesan, R.L. Greene, A.J.Millis, *Physical Review B* **61** 9665 (2000)

[84] A. Das et *al. Jounal of Applied Physics* **90** 1429 (2001)

[85] R. P. Sharma, G. C. Xiong, C. Kwon, R. Ramesh, R. L. Greene, and T. Venkatesan, *Physical Review B* **54** 10014 1996

[86] T.P. Russel *Mat Sci Rep* **5** 171 (1990)

[87] H. Dosch *Critical Phenomena at Surfaces and Interfaces: Evanescent x-ray and neutron scattering* Springer Tracts in Modern Physics 126 (1992)

[88] L.G. Parratt *Phys. Rev.* **95** 359 (1954)

[89] G.P Felcher et *al. Rev Sci Instr* **58** 609 (1987)

[90] R.Pynn *Rev. Sci. Instrum.* **55** 837 (1984), M. Bray et *al. Proc. SPIE Int. Soc. Opt. Eng.* **44** 4509 (2001)

[91] K.P. Coulter et *al. Nucl. Intr. Meth A* **288** 463 (1999)

[92] J.F. Anker and J.P.Felcher *J. Magn. magn. Mater.* **200** 741 (1999)

[93] A. Rühm et *al. Physical Review B* **60** 16073 (1999)

[94] see references 2,3,9, in A. Rühm et *al. Physical Review B* **60** 16073 (1999)

[95] B.E. Warren "X-Ray Diffraction" Dover publications INC, New York

[96] I.K Robinson *Physical Review B* **33** 3830 (1986)

[97] I.K. Robinson, D.J. Tweet *Rep. Prog. Phys.* **55** 599 (1992)

[98] S.R. Andrews and R.A. Cowley *JP C : Solid State Phys* **18** 6427 (1985)

[99] R.P. Scaringe and R. Comès *Physical Methods of Chemistry*, Sec. Edition, ed. Bryant W. Rossiter and John F. Hamilton, Wiley & Sons, 1990, Vol. V, *Determination of structural features of crystalline and amorphous solids.*

[100] B. Nickel et *al. Physical Review Letters* **85** 134 (2000)

[101] H. You, U. Welp, G.W. Crabtree, Y. Fang, S.K. Sinha, J.D. Axe, X. Jiang and S.Moss *Physical Review B* **45** 5107 (1992)

[102] PhD thesis Jürgen Klein. University of Cologne Germany 2001

[103] J.Klein, J.B.Phillip, G.Carbone, A.Vigliante, L.Alff and R.Gross *Physical Review B* **66** 052414 (2002)

[104] A. De Andres *et al. Applied Physics Letters* **83** 713 (2003)

[105] I. Vartanyants, C. Ern, W. Donner and H. Dosch *Applied Physics Letters* **77** 3929 (2000)

[106] P.G.Radaelli et *al. Phys Rev Lett* **75** 4488 (1995)

[107] J. Simon, T. Walther, W. Maden, J. Klein, D. Reisinger, L. Alff, R. Gross *Appl. Phys. Lett.* **84** 3882 (2004)

[108] R. Desfeux, S. Bailleul, A. Da Costa, W. Prellier, A.H. Hagiri-Gosnet *Applied Physics Letters* **78** 3681 (2001)

[109] J.C. Jiang, I. Meletis, K.I. Gnanasekas *Applied Physics Letters* **80** (2002)4381; X.Q. Pan, J.C. Jiang, C.D. Theis, D.G. Scholm *Applied Physics Letters* **83** 2315 (2003)

[110] F. Ott et *al. J. Mag. Mag. Mater.* **211** 212 (2000)

Acknowledgements

The work presented in this PhD thesis has been possible thank to the help of the following persons:

Dr. P. Wochner, Dr. A. Vigliante, U. Gebhardt, Dr. Nikolai Kasper and Dr. D. Mannix helped me during synchrotron measurements. In particular, Dr. P. Wochner has closely followed this work, giving me also useful advices for the redaction of this book.

I thank Dr. Jürgen Klein and Dr. Lambert Alff for the useful discussions, and for being always ready to prepare new samples.

Dr. A. Vorobiev and Dr. B. Nickel for their support during Polarised Neutron experiments at ILL in Grenoble, and Dr. A. Rühm for his help with data analysis and the program "WinFit".

Dr. D. Goll and Dr. E. Göring, from the MPI-MF, Department of G.Schütz, introduced me to the use of the SQUID.

Adrian, Sebastian and Bärbel helped for the translation of the "Zusammenfassung" chapter.

Finally, I would like to thank Annette and Shurik for the unestimable help for the submission of the manuscript to the University of Stuttgart.

Thank to Prof. Dr. H. Dosch for welcoming me in his group.

This work was performed on the EPSRC-funded XMaS beam line at the ESRF, directed by M.J. Cooper and C. Lucas. I am grateful to the beam line team of S.D. Brown, L. Bouchenoire, D. Mannix, D.F. Paul and P. Thompson for their invaluable assistance, and to S. Beaufoy and J. Kervin for additional support.